



# **POLITECNICO DI TORINO**

*Faculty of Engineering*

Master of Science in Petroleum Engineering

## **A Fast and accurate investigation into CO<sub>2</sub> Storage challenges by Making a Proxy Model on a Developed Static Model with The Application of Artificial Intelligence/Machine Learning**

Supervisor:

Associate professor Vera Rocca (Politecnico di Torino)

Associate professor Ashkan Jahanbani Ghahfarokhi (NTNU)

Behzad Amiri

**JUNE 2022**

Thesis submitted in compliance with the requirements for the Master of Science degree

---

## ABSTRACT

CO<sub>2</sub> emissions as the root of global warming have been intended to be cut by net zero until 2050. CCS is a technology capable of capturing produced CO<sub>2</sub> in energy sectors and industries to be injected and stored into the subsurface geological formations like depleted oil and gas reservoirs and aquifers possessing effective trapping mechanisms rather than emissions in the atmosphere. CO<sub>2</sub> storage involves drilling an injection well, injection, well control, and CO<sub>2</sub> propagation within geological storage, governed by petroleum engineering principles. Therefore, oil and gas companies, besides petroleum engineers, are responsible for the exploration and assessment of viable storages in addition to execution.

Among multiple risks, fracturing in caprock and around the wellbore, in addition to leakage through geological paths and legacy wells, are the predominant ones that follow CO<sub>2</sub> injection and storage. Storage simulation is employed to monitor well performance and CO<sub>2</sub> plume migration to optimize the progress with respect to the objectives and constraints. The common approach is a numerical simulation by commercial and open-source simulators. A full field simulation may take a few hours, depending on the model's type, dimension, and resolution. Sensitivity analysis and optimization of CO<sub>2</sub> storage by conventional numerical methods require several runs, which is not temporally efficient.

During the last two decades, various types of proxy models have been developed to replicate the reservoir simulation results in the field, well, and grid scales from input features by mathematical, statistical, and AI approaches. The proxy models are able to be substituted for numerical simulators to apply sensitivity analysis, optimization, and history matching extremely quickly without sacrificing accuracy. The most current proxy models are AI and machine learning-based proxy models, called Smart Proxy Model or Surrogate Reservoir Proxy Model (SRM).

In this study, after updating the numerical model and designing a feasible injection well, by training two DNNs, grid-based SRMs were developed to simulate dynamic CO<sub>2</sub> saturation and pressure distribution in the entire model's grid blocks in 1 minute with 99% accuracy. Subsequently, the Genetic Algorithm optimized the CO<sub>2</sub> injection into the Smeaheia saline aquifer, which is placed in the North Sea, and found the optimum CO<sub>2</sub> injection rate and duration, maximizing storage capacity without leakage and fracturing.

---

## ACKNOWLEDGEMENT

In the last three years, I passed a lot of ups and downs and overcame many problems during the corona pandemic to improve my knowledge in petroleum engineering. In the last step, this thesis is written to employ the learned subjects in the final examination and fulfill my education in the master of science in petroleum engineering at Politecnico di Torino university. Intending to experience other academic structures and obtain a global vision for the oil and gas industry, I passed one semester at the Norwegian University of Science and Technology (NTNU) as an exchange student to perform the thesis in a part of CEORS Gemini-Center activities (CO<sub>2</sub> Enhanced Oil Recovery and Storage), a strategic collaboration between NTNU and SINTEF (<https://www.ntnu.edu/ceors>). The research topic was chosen according to my interests in ai, machine learning, data science, and programming. Moreover, as a human, I desired to utilize my skills and knowledge to tackle the most critical threat to life on the earth, global warming.

In this way, I should be grateful to professor Vera Rocca for accepting the supervision of this research at Politecnico di Torino university and providing technical support. Moreover, I appreciate professor Ashkan Jahanbani Ghahfarokhi, my supervisor at NTNU, who always supported and guided me by introducing the contemporary topics of reservoir engineering and providing expert feedback on proxy modeling and CO<sub>2</sub> storage. Additionally, I am thankful to Cuthbert Shang Wui Ng, Ph.D. Candidate at NTNU; Bamshad Nazarian, lead researcher on CO<sub>2</sub> storage and EOR technologies at Equinor; and Alv-Arne Grimstad, senior research scientist at SINTEF for brilliant consultation in proxy modeling, CCS, and numerical simulation.

Finally, I am appreciative of my family, partner, and friends, who supported me on all tough days and loved me without any expectation.



## SUMMARY

ABSTRACT.....	I
ACKNOWLEDGEMENT.....	II
List of Figures.....	VII
List of Tables.....	XI
1 Introduction.....	1
1.1 Background.....	1
1.2 Objective.....	3
1.3 Structure of the Report.....	3
2 Literature Review.....	4
2.1 CO <sub>2</sub> Capture and Storage.....	4
2.1.1 Capture of CO <sub>2</sub> .....	5
2.1.2 Transport of CO <sub>2</sub> .....	6
2.1.3 Underground geological storage.....	6
2.1.4 CO <sub>2</sub> Properties.....	9
2.1.5 Rock and Fluid Interaction.....	10
2.1.6 Risk assessment of CO <sub>2</sub> Storage.....	12
2.2 Proxy Modeling.....	13
2.2.1 Building SRM.....	13
2.2.2 Previous studies on proxy modeling.....	19
2.3 Optimization.....	22
2.3.1 Optimization for CO <sub>2</sub> storage.....	24
2.3.2 Genetic algorithm.....	24
3 Methodology, Problem, and Model Description.....	28
3.1 Study Workflow.....	28
3.2 Reservoir Description.....	30
3.2.1 Geology and Stratigraphy.....	31
3.2.2 Prospects Characteristics.....	35
3.2.3 Stress Model and Geomechanical Properties.....	36
3.3 Reservoir Model.....	37
3.3.1 Geological Model and Properties.....	37
3.3.2 Fluid Model.....	39

---

3.3.3	Numerical Simulation.....	41
3.3.4	Well Design .....	44
3.4	Optimization Problem.....	47
3.4.1	Objective Formulation.....	47
3.4.2	Optimization Algorithm .....	48
3.5	Proxy Modeling .....	48
4	Proxy Modeling and optimization, Building the structure.....	49
4.1	Developing SRMs.....	49
4.1.1	Data Generation .....	49
4.1.2	Input Features.....	51
4.1.3	Sampling Dataset .....	53
4.1.4	ANN Structure .....	54
4.2	Optimization.....	56
4.2.1	Optimization Implementation.....	57
5	Proxy Model and Optimization Progress, result, and validation.....	59
5.1	Developing Proxy Model .....	59
5.1.1	Model Training .....	60
5.1.2	Blind Evaluation .....	62
5.2	Proxy Model Results.....	64
5.2.1	SRM Result.....	65
5.2.2	Blind Evaluation Result.....	77
5.3	Optimization Result .....	83
5.3.1	Optimum Plan Validation and Visualization.....	83
6	Discussion .....	86
7	Conclusion .....	88
8	References.....	89



## LIST OF FIGURES

Figure 2.1: Emissions reductions by mitigation measure in the NZE, 2020-2050 (Bouckaert, et al., 2021) .....	4
Figure 2.2: Conceptual diagram of carbon capture and storage. Image supplied by CO <sub>2</sub> CRC (Bandilla, 2020) .....	5
Figure 2.3: Carbon capture at power plants: (A) no capture, (B) post-combustion, (C) pre-combustion, and (D) oxyfuel combustion. (Metz, 2005) .....	6
Figure 2.4: Options for storing CO <sub>2</sub> in deep underground geological formations (after Cook, 1999; Metz, 2005) .....	7
Figure 2.5: Density of CO <sub>2</sub> as a function of temperature and pressure.....	10
Figure 2.6: Viscosity of CO <sub>2</sub> as a function of temperature and pressure .....	10
Figure 2.7: Brine CO <sub>2</sub> IFT dependence on pressure, temperature, and brine salinity (Rackley S. A., 2017) .....	11
Figure 2.8: drainage imbibition capillary pressure curves (Rackley S. A., 2017).....	11
Figure 2.9: Risks associated with the geological storage of CO <sub>2</sub> (Li & Liu, 2016).....	12
Figure 2.10: Some potential escape routes for CO <sub>2</sub> injected into saline formations and remedial measures (Metz, 2005).....	12
Figure 2.11: Summary of proxy model scale and application (Matthew, 2021) .....	14
Figure 2.12: General schematic of ANN, based on (Silva, Spatti, Flauzino, Liboni, & Alves, 2017).....	16
Figure 2.13: ANN forward propagation, based on (Géron, 2019).....	17
Figure 2.14: Behavior of MSE function respect to training epochs (Silva, Spatti, Flauzino, Liboni, & Alves, 2017) .....	18
Figure 2.15: Proxy modeling workflow, based on (Zubarev, 2009).....	19
Figure 2.16: Grid based cascading flow-chart (Gholami, 2014).....	20
Figure 2.17: CO <sub>2</sub> mole fraction distribution map (Gholami, 2014).....	20
Figure 2.18: Pressure distribution map (Gholami, 2014) .....	20
Figure 2.19: Oil saturation distribution map (Gholami, 2014).....	21
Figure 2.20: Water saturation distribution map (Gholami, 2014).....	21
Figure 2.21: Oil production by SRMw (Gholami, 2014) .....	21

---

Figure 2.22: Distribution maps of Pressure, Gas saturation and CO <sub>2</sub> mole fraction (from left: CMG output, SRM result and Error) (Amini, 2015).....	22
Figure 2.23: Global optimum & local optima (Hendrix, Boglárka, & others, 2010).....	23
Figure 2.24: One-point crossover that splits up the genome of two solutions at an arbitrary (Kramer, 2017).....	26
Figure 3.1: Study workflow .....	29
Figure 3.2: Smeaheia outline and location of this study's AOI: GN1101 3D seismic survey (Statoil, 2016) .....	30
Figure 3.3: Correlation of the wells on the Smeaheia fault block (Erichsen, Rørvik, Kearney, & Haaberg, 2013).....	31
Figure 3.4: Storage complex main seal units identified by well correlation and seismic interpretation (Erichsen, Rørvik, Kearney, & Haaberg, 2013).....	32
Figure 3.5: Main seal unit thickness (m) maps for the Smeaheia Storage Complex (Erichsen, Rørvik, Kearney, & Haaberg, 2013).....	33
Figure 3.6: Storage formation (Erichsen, Rørvik, Kearney, & Haaberg, 2013).....	34
Figure 3.7: Structural setting of the Smeaheia storage site, where the location of each seismic profile is posted on the Top Sognefjord Fm depth map in the upper left corner (Erichsen, Rørvik, Kearney, & Haaberg, 2013).....	34
Figure 3.8: Alpha and Beta prospect location in respect to GN 101 survey and Smeaheia storage (Statoil, 2016) .....	35
Figure 3.9: Smeaheia stress model (Equinor & Gassnova, 2021) .....	37
Figure 3.10: Smeaheia model's faults and horizons .....	38
Figure 3.11: Probability distribution of porosity and permeability.....	39
Figure 3.12: The PVT properties of Statoil's model (exported from Petrel).....	40
Figure 3.13: The Relative permeability and capillary pressure of Statoil's model (exported from Petrel) .....	41
Figure 3.14: Saturation distribution in 2300, after 25 years injection since 2022 .....	42
Figure 3.15: Bottom hole and field pressure.....	42
Figure 3.16: Pore volume multiplier .....	43
Figure 3.17: Storage structure.....	43
Figure 3.18: Well location sensitivity analysis.....	44
Figure 3.19: Minimum horizontal stress .....	45

---

Figure 3.20: Fracture pressure .....	45
Figure 3.21: Saturation distribution in 2072 after 35-year CO <sub>2</sub> injection by newly designed injection well .....	46
Figure 3.22: Bottom hole pressure of well Alpha with 5872000 sm <sup>3</sup> /day .....	46
Figure 4.1: Injection rate of numerical simulation cases .....	50
Figure 4.2: Bottom hole pressure of numerical simulation cases .....	50
Figure 4.3: Tier model (Amini, 2015) .....	52
Figure 5.1: Saturation model loss	Figure 5.2: Saturation model MAE .....
Figure 5.3: Saturation model evaluation .....	60
Figure 5.4: Pressure model loss	Figure 5.5: Pressure model MAE .....
Figure 5.6: Pressure Model Evaluation .....	61
Figure 5.7: Real MAE of the pressure model .....	62
Figure 5.8: Saturation model blind evaluation .....	63
Figure 5.9: Pressure model blind evaluation .....	64
Figure 5.10: Pressure and CO <sub>2</sub> saturation distribution and error maps in the case of 25 years injection with the rate of 1798810 Sm <sup>3</sup> /day, 30 <sup>th</sup> layer .....	65
Figure 5.11: Pressure and CO <sub>2</sub> saturation distribution and error maps in the case of 25 years injection with the rate of 1798810 Sm <sup>3</sup> /day, 40 <sup>th</sup> layer .....	66
Figure 5.12: Pressure and CO <sub>2</sub> saturation distribution and error maps in the case of 25 years injection with the rate of 1798810 Sm <sup>3</sup> /day, 50 <sup>th</sup> layer .....	67
Figure 5.13: Pressure and CO <sub>2</sub> saturation distribution and error maps in the case of 50 years injection with the rate of 1798810 Sm <sup>3</sup> /day, 1 <sup>st</sup> layer .....	68
Figure 5.14: Pressure and CO <sub>2</sub> saturation distribution and error maps in the case of 50 years injection with the rate of 1798810 Sm <sup>3</sup> /day, 2 <sup>nd</sup> layer .....	69
Figure 5.15: Pressure and CO <sub>2</sub> saturation distribution and error maps in the case of 50 years injection with the rate of 1798810 Sm <sup>3</sup> /day, 40 <sup>th</sup> layer .....	70
Figure 5.16: Pressure and CO <sub>2</sub> saturation distribution and error maps in the case of 25 years injection with the rate of 7610350 Sm <sup>3</sup> /day, 1 <sup>st</sup> layer .....	71
Figure 5.17: Pressure and CO <sub>2</sub> saturation distribution and error maps in the case of 25 years injection with the rate of 7610350 Sm <sup>3</sup> /day, 2 <sup>nd</sup> layer .....	72
Figure 5.18: Pressure and CO <sub>2</sub> saturation distribution and error maps in the case of 25 years injection with the rate of 7610350 Sm <sup>3</sup> /day, 70 <sup>th</sup> layer .....	73

---

Figure 5.19: Pressure and CO <sub>2</sub> saturation distribution and error maps in the case of 50 years injection with the rate of 7610350 Sm <sup>3</sup> /day, 1 <sup>st</sup> layer .....	74
Figure 5.20: Pressure and CO <sub>2</sub> saturation distribution and error maps in the case of 50 years injection with the rate of 7610350 Sm <sup>3</sup> /day, 2 <sup>nd</sup> layer .....	75
Figure 5.21: Pressure and CO <sub>2</sub> saturation distribution and error maps in the case of 50 years injection with the rate of 7610350 Sm <sup>3</sup> /day, 50 <sup>th</sup> layer .....	76
Figure 5.22: Pressure and CO <sub>2</sub> saturation distribution and error maps in the case of 25 years injection with the rate of 3459250 Sm <sup>3</sup> /day, 1 <sup>st</sup> layer .....	77
Figure 5.23: Pressure and CO <sub>2</sub> saturation distribution and error maps in the case of 25 years injection with the rate of 3459250 Sm <sup>3</sup> /day, 40 <sup>th</sup> layer .....	78
Figure 5.24: Pressure and CO <sub>2</sub> saturation distribution and error maps in the case of 25 years injection with the rate of 3459250 Sm <sup>3</sup> /day, 50 <sup>th</sup> layer .....	79
Figure 5.25: Pressure and CO <sub>2</sub> saturation distribution and error maps in the case of 50 years injection with the rate of 3459250 Sm <sup>3</sup> /day, 1 <sup>st</sup> layer .....	80
Figure 5.26: Pressure and CO <sub>2</sub> saturation distribution and error maps in the case of 50 years injection with the rate of 3459250 Sm <sup>3</sup> /day, 2 <sup>nd</sup> layer .....	81
Figure 5.27: Pressure and CO <sub>2</sub> saturation distribution and error maps in the case of 50 years injection with the rate of 3459250 Sm <sup>3</sup> /day, 50 <sup>th</sup> layer .....	82
Figure 5.28: CO <sub>2</sub> Saturation distribution in 2100, 28 years after stopping CO <sub>2</sub> injection with the rate of 4683495 Sm <sup>3</sup> /day for 50 years.....	84
Figure 5.29: Pressure and CO <sub>2</sub> saturation distribution and error maps in the case of 50 years injection with the rate of 4683495 Sm <sup>3</sup> /day (optimum case), 1 <sup>st</sup> layer .....	85

---

## LIST OF TABLES

Table 2.1: Subsurface carbon storage options .....	7
Table 2.2: Trapping mechanisms for geological carbon sequestration .....	8
Table 2.3: SRM input .....	14
Table 2.4: ANN input data structure .....	16
Table 3.1: Structural capacity estimate for Alpha prospect.....	35
Table 3.2: Structural capacity estimate for Beta prospect .....	36
Table 3.3: Smeaheia rock mechanic data .....	36
Table 3.4: Initial Condition.....	39
Table 4.1: Input Features .....	51
Table 5.1: The final population of the optimization.....	83



---

# 1 INTRODUCTION

## 1.1 Background

After the Paris Agreement in December 2015, Framework Convention on Climate Change (FCCC) published a report on the Agreement and its adoption (Nations, 2015) that defined the Nationally Determined Contributions (NDC) regulations. The main target of NDCs is holding the global average temperature below 2 °C above pre-industrial levels and concentrating efforts on limiting temperature increase below 1.5 °C above pre-industrial levels. Since then, a special report (Masson-Delmotte, 2018) revealed the emission trend, and NDC's ambition deviated from the path of limiting global warming to under 2 °C. According to the research result, if greenhouse gas emissions do not decline sharply until 2030, global warming will surpass 1.5 °C; consequently, irreversible extinction of many frail ecosystems will occur. Carbon Capture and Storage (CCS) is a suitable technology that takes action against CO<sub>2</sub> emission at the source directly and contributes to 15% of total emissions cut to achieve the global target of the net-zero CO<sub>2</sub> energy sector and industrial activity emissions in 2050 (Bouckaert, 2021).

A measure of challenges follows geological CO<sub>2</sub> storage in terms of seismicity effect, economic factors, and leakage due to overpressure, transmissible faults and fractures, and legacy wells (Ajayi, 2019) that must be investigated and defined in every CCS project. Subsequently, the available risks can be avoided by monitoring pressure and CO<sub>2</sub> plume migration in the porous media, and injection optimization (Santibanez-Borda, 2019). Indeed, it is required to run numerous numerical simulations to analyze the sensitivity of dynamic pressure and gas saturation distribution, and rock response respect to the well position and injection condition, as well as searching for the optimum condition without any risk in a computationally heavy and time-consuming process (Jiang, 2011). Proxy Modeling can be a complementary method for heavy numerical simulations and an alternative in the long term (Jaber, 2019), which enhances computation time by more than one hundred times (Hosseini Boosari, 2019). Smart Proxy Modeling (SPM), or Surrogate Proxy Reservoir Modeling (SRM), is an AI and machine learning-based data-driven model that can substitute large and complex numerical models and replicate pressure and saturation distribution throughout the grids at each time step with high pace and adequate

---

accuracy (Mohaghegh, 2018). Mohaghegh (2012) and his research team, Gholami (2014) and Amini (2015) are pioneers in smart proxy modeling. This study uses grid-based SRM subsequent to Mohaghegh (2012) and Amini (2015).

The case study for proxy modeling and optimization is Smeaheia CO<sub>2</sub> Storage (Equinor & Gassnova, 2021), an aquifer in the Norwegian North Sea on the Horda Platform, east of the Troll Field. Smeaheia has been investigated and modeled by Erichsen, Rørvik, Kearney, & Haaberg (2013), Statoil (2016), and Brobakken (2018) as part of the Northern Lights' full-scale CCS project and a potential for future storage. Each one created a black oil model by Eclipse100 and Petrel based on different Geological perceptions. In Gassnova's model, an average property value is distributed for each layer, whereas properties of Statoil's model are distributed stochastically. Two exploration wells were drilled in the east and west of the field; they were dry and left abandoned. However, the acquired data from the wells and 2D and 3D seismic are employed for creating geological models.

Nowadays, computationally expensive optimization problems, either for injection or production optimization, are being performed by Surrogate Models to reduce computation time and compensate for the lack of facility. For instance, Golzari (2015) and Ng (2021) utilized surrogate modeling for production optimization, or it is employed for injection optimization in CO<sub>2</sub> Storage or CO<sub>2</sub>-EOR by Agada (2017), Nait Amar (2018), and Sun (2021). They used various optimization algorithms such as Genetic Algorithm (GA) (Liu, 2021; Agada, 2017; Agarwal, 2019), Ant Colony (ACO) (Nait Amar, 2018), Hooke–Jeeves Direct Search (HJDS) (Cameron, 2012), SIMPLEX, and Generalized Reduced Gradient (GRG) (Santibanez-Borda, 2019). GA is a popular optimization algorithm developed by John Holland (1975) from DNA evolution. The prevalence of GA can be due to its competence in dealing with complex problems, whether the objective function is stationary or non-stationary (changing with time), linear or non-linear, continuous or discontinuous, or with random noise (Yang, 2021). Moreover, in addition to unconstrained single-objective problems, it can be adapted for constrained single-objective and multi-objective problems (Konak, 2006). Indeed, GA can optimize CO<sub>2</sub> injection, which may be a constrained or multi-objective problem.

---

## 1.2 Objective

The core objective of the study is to create a full-scale grid-based SRM in lieu of typical numerical simulation facilities to achieve a dramatic enhancement in computation cost without sacrificing accuracy. The SRM will model CO<sub>2</sub> storage, a practical solution for the energy transition (Arlota & de Medeiros Costa, 2021). Afterward, the volume of stored CO<sub>2</sub> must be maximized as the optimization objective, in parallel with controlling the migration path and avoiding fracture pressure as safety constraints by selecting the optimum injection rate and duration, and well location.

After selected geological model sensitivity analysis, the well location will be chosen in an acceptable location according to the bottom-hole pressure tolerance and the influence of virtual wells on the CO<sub>2</sub> plume migration path.

Briefly, the research objectives can be listed as follows:

1. Defining the objectives of the optimization and the kind of optimization according to the field characteristics and challenges
2. Developing a grid-based SRM as a substitute for computationally heavy numerical simulations to decline the running time.
3. Optimizing CO<sub>2</sub> injection according to defined objectives with the help of the created proxy model.

## 1.3 Structure of the Report

In this thesis, the literature review and theory of CCS, proxy modeling, optimization, and Genetic algorithm follow the thesis introduction. The third chapter will describe the project methodology, storage characteristics, model, and required optimization problem. In chapter four, the proxy model and optimization problem will be structured to represent the obtained results from the implementation in chapter five. Finally, the progress and results will be discussed and concluded in chapters six and seven, respectively.

## 2 LITERATURE REVIEW

### 2.1 CO<sub>2</sub> Capture and Storage

Based on the IEA report (Bouckaert, et al., 2021), the energy sector participates in 75% of greenhouse gas production and is at the root of climate change disasters, perhaps the most tremendous challenge for humankind. Limiting the global temperature increase to 1.5°C would be possible by falling total CO<sub>2</sub> emissions to net-zero until 2050, which requires a wide range of technologies. Carbon Capture and Storage (CCS) is a feasible technology that has the task of annual capturing 7.6 Gt out of 36 emitted CO<sub>2</sub> in a net-zero emission path (Bouckaert, et al., 2021).

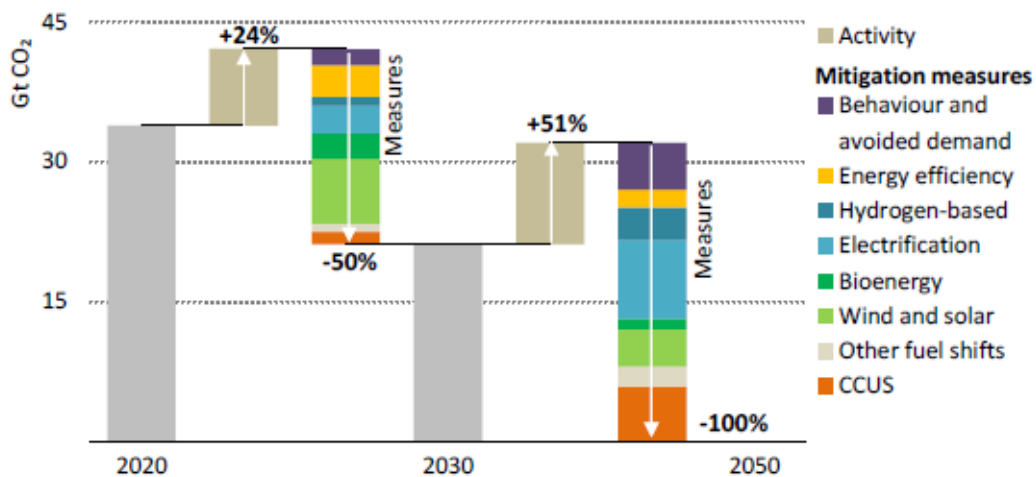


**Figure 2.1: Emissions reductions by mitigation measure in the NZE, 2020-2050 (Bouckaert, et al., 2021)**

CCS is a remedy technology for climate change that consists of capturing and purifying CO<sub>2</sub> produced in industrial and energy origins in preference to releasing into the atmosphere, transporting it to a suitable site location, both onshore and offshore, and storing CO<sub>2</sub> in the subsurface for a long time (Bandilla, 2020), as shown in figure 2.2.

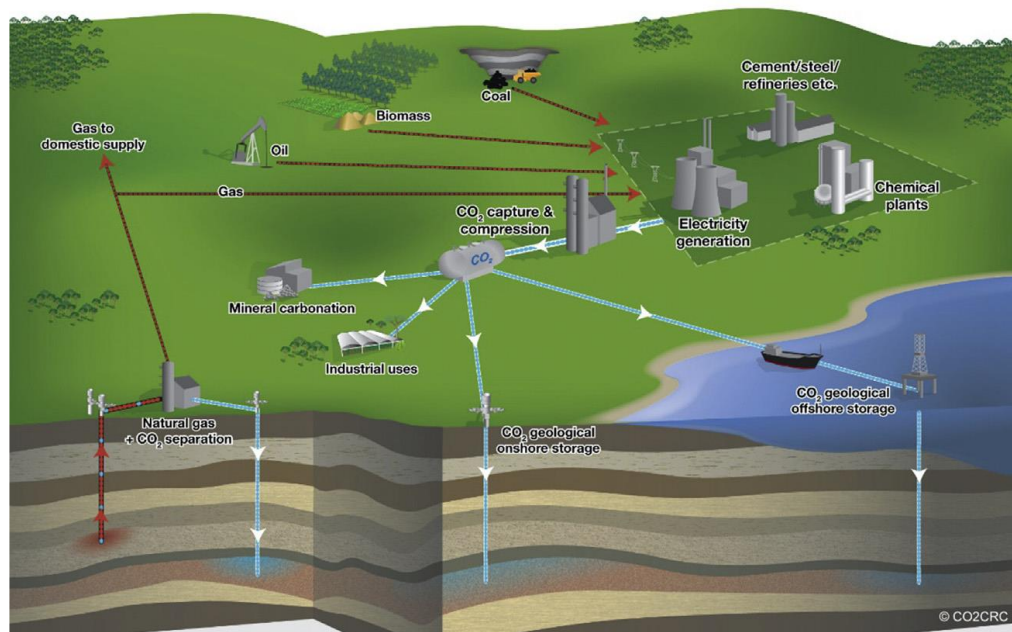


**Figure 2.2: Conceptual diagram of carbon capture and storage. Image supplied by CO<sub>2</sub>CRC (Bandilla, 2020)**

### 2.1.1 Capture of CO<sub>2</sub>

The first step of CCS is capturing carbon, and post-combustion capture, oxy-fuel combustion capture, and pre-combustion capture are the main capturing processes from the use of fossil fuels and biomass. Post-combustion capture is performed when the produced flue gas by fossil fuels and biomass combustion is captured. Rather than discharging flue gas into the atmosphere directly, it will be fed to a separator that filters a vast majority of CO<sub>2</sub> and will be stored in a reservoir in addition to releasing the remaining gas into the air. The oxy-fuel combustion capture is the same as post-combustion capture, with the difference of using pure oxygen instead of air for the combustion and recycling the CO<sub>2</sub> and H<sub>2</sub>O-rich flue gas to the combustor in order to moderate inordinately high-temperature flame. During pre-combustion capture, fuel reacts with the mixture of air or oxygen and steam to produce syngas consisting of carbon monoxide and hydrogen. Subsequently, CO<sub>2</sub> and hydrogen, created due to carbon monoxide reaction with steam, will be separated by a physical or chemical absorption process (Metz, 2005).

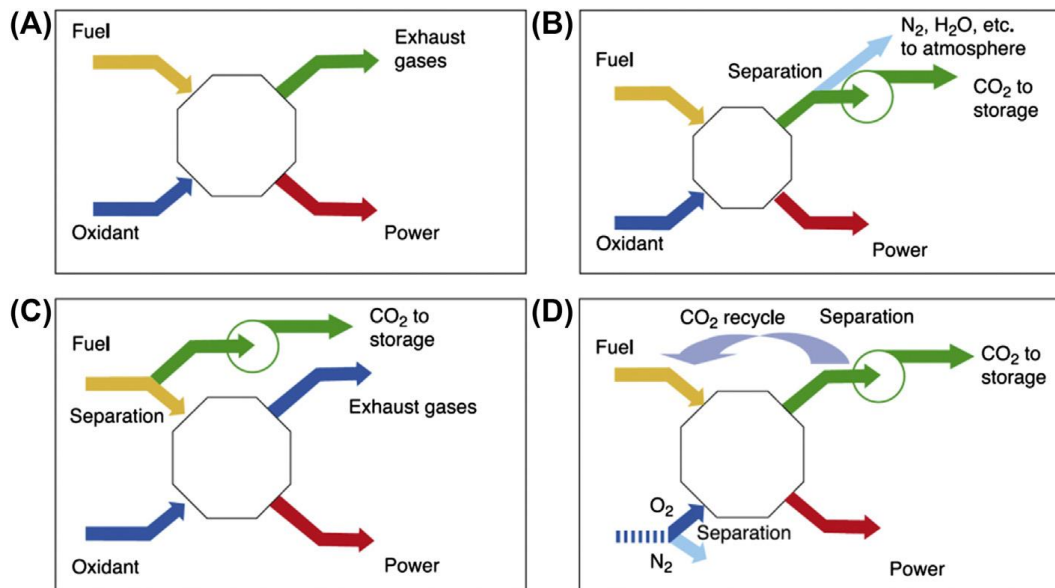


**Figure 2.3: Carbon capture at power plants: (A) no capture, (B) post-combustion, (C) pre-combustion, and (D) oxyfuel combustion. (Metz, 2005)**

### 2.1.2 Transport of CO<sub>2</sub>

CO<sub>2</sub> transport can be carried out in gas, liquid, and solid phase. Companies employ tanks, pipelines, and ships for economic and large-scale transport of CO<sub>2</sub> in gas and liquid states. Low-pressure gas occupies a large volume; therefore, pipelines transport compressed gas. Furthermore, the gas volume is able to be reduced more by liquefaction, solidification, and hydration. Ships transport liquified CO<sub>2</sub> as LPG (liquefied petroleum gas) and LNG (liquefied natural gas). Although, solidification is not reasonable in aspects of energy and cost because of too much energy consumption (Metz, 2005).

### 2.1.3 Underground geological storage

The last step of CCS is storing captured CO<sub>2</sub> in the subsurface in place of discharging it into the atmosphere. The subsurface is the hugest carbon reservoir on the earth in the shape of coal, oil, gas, organic-rich shales, and carbonate rocks. The first structured CO<sub>2</sub> injection into the underground geological formations took place in Texas, USA, in 1972, with the intention of enhanced oil recovery (Hill, Hovorka, & Melzer, 2013). In this project, injecting 600 million metric tonnes of CO<sub>2</sub> produced 1.4 billion barrels of oil, and produced CO<sub>2</sub> was reinjected. Since then, a measure of subsurface storage options and purposes for CO<sub>2</sub> have been designed, which are mentioned in table 2.1.

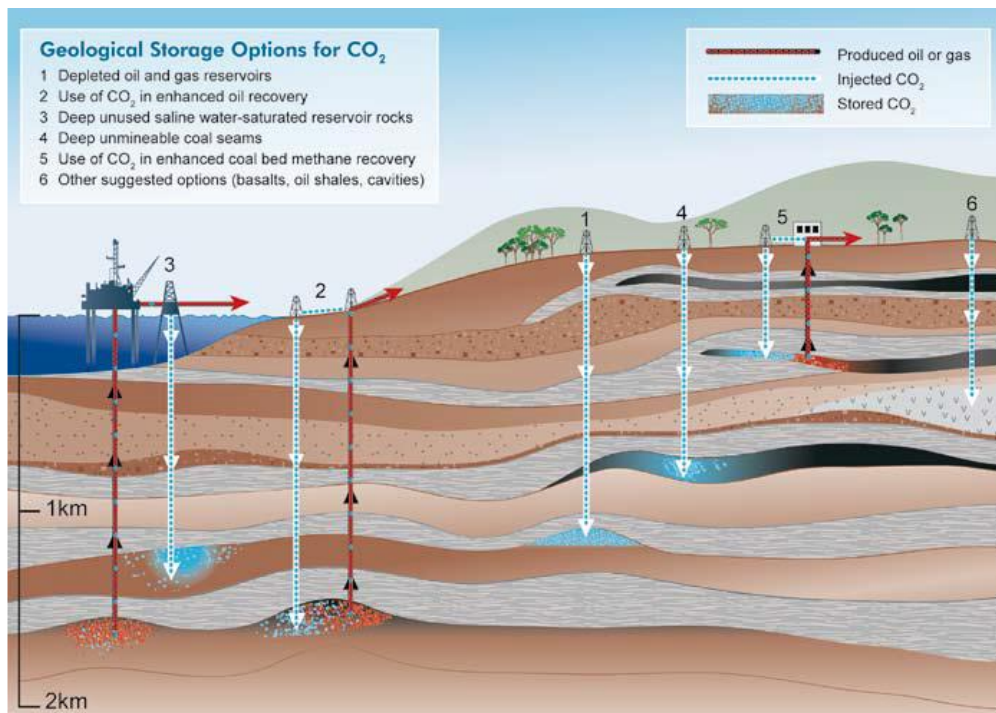


**Figure 2.4: Options for storing CO<sub>2</sub> in deep underground geological formations (after Cook, 1999; Metz, 2005)**

**Table 2.1: Subsurface carbon storage options (Rackley, 2017)**

Subsurface storage option	Description
Saline aquifer storage	Injection into saline aquifers that are not considered potential drinking water resources
Enhanced oil recovery (EOR)	Injection into operating oil fields, typically those containing heavier oil, initially to maximize economic oil recovery and more recently to also achieve CO <sub>2</sub> storage
Enhanced gas recovery (EGR)	Similar to EOR, injection into depleted or operating gas fields with the objective of co-optimizing hydrocarbon recovery and CO <sub>2</sub> storage
Enhanced coal bed methane recovery (ECBM)	Injection into unmineable coal seams, increasing CBM recovery by preferential adsorption of CO <sub>2</sub> and desorption of methane
Enhanced geothermal systems (EGS)	Use of CO <sub>2</sub> as a working fluid in geothermal energy extraction and storage systems, a variant being the extraction of heat from an injected CO <sub>2</sub> plume in a saline aquifer (CO <sub>2</sub> plume geothermal)
Compressed air energy storage systems (CAES)	Use of CO <sub>2</sub> as a cushion gas to store energy from intermittent sources such as wind or solar power systems

---

In situ mineral carbonation	Injection of CO <sub>2</sub> into fractured alkali mineral deposits, such as sheet basalts, and storage via mineral carbonation
-----------------------------	---

---

(Rackley, 2017)

After injection, CO<sub>2</sub> distribution in geological storage will be ruled by fluid flow in consequence of induced pressure gradient by injection; natural hydraulic gradient in the storage; buoyancy due to CO<sub>2</sub> and formation fluids density difference; molecular diffusion; dispersion and fingering in response of heterogeneity and mobility contrast between CO<sub>2</sub> and formation fluids; dissolution into the formation fluids; mineralization by CO<sub>2</sub> reaction with minerals and organic particles in the formation, pore space trapping, and CO<sub>2</sub> adsorption by organic material. Moreover, CO<sub>2</sub> must be trapped and immobilized for the long term by physical and chemical trapping mechanisms in table 2.2.

**Table 2.2: Trapping mechanisms for geological carbon sequestration**

Subsurface storage option	Description
Static trapping	Mobile CO <sub>2</sub> is trapped in stratigraphic and structural traps, or in man-made caverns.
Structural trapping	Structural traps refer to geological media which precludes the upward and lateral movement of CO <sub>2</sub> induced by crust movement (faults and folds).
Stratigraphic trapping	Stratigraphic traps refer to geological media which precludes the upward and lateral movement of CO <sub>2</sub> induced by depositional and/or diagenetic processes.
Hydrodynamic trapping	<ol style="list-style-type: none"> <li>1. The buoyant CO<sub>2</sub> is kept underground by an impermeable caprock.</li> <li>2. The injected CO<sub>2</sub> is primarily trapped as a gas or supercritical fluid. CO<sub>2</sub> will rise up due to buoyancy effect until it approaches the seals.</li> </ol>
Capillary trapping	<ol style="list-style-type: none"> <li>1. It means the trapping by capillary forces in the pores on the trailing edge of the mobile CO<sub>2</sub> plume (typically).</li> <li>2. CO<sub>2</sub> phase is disconnected into an immobile (trapped) fraction (or called residual trapping).</li> </ol>
Residual trapping	<ol style="list-style-type: none"> <li>1. CO<sub>2</sub> can be stored as an immobile form in deep saline aquifers due to the density difference</li> </ol>

---

---

	<p>between CO<sub>2</sub> and brine. CO<sub>2</sub> will be left behind as trapped (residual) saturation.</p> <p>2. CO<sub>2</sub> is trapped in the pore space at irreducible gas saturation in which case CO<sub>2</sub> is immobile because of the interfacial tension between CO<sub>2</sub> and formation water.</p> <p>3. It means the trapping by capillary forces in the pores on the trailing edge of the mobile CO<sub>2</sub> plume (Less commonly).</p> <p>4. Residual trapping happens when water is imbibed behind the migrating CO<sub>2</sub> plume, and is caused by gas-water relative permeability hysteresis.</p> <p>5. Formation of disconnected blobs of CO<sub>2</sub> phase is held by capillary forces.</p>
Solubility trapping (Dissolution trapping)	<p>1. CO<sub>2</sub> dissolves in hydrocarbons or water contained in subsurface formations by diffusion.</p> <p>2. CO<sub>2</sub> mixes with residual gas.</p> <p>3. CO<sub>2</sub> dissolves in brine as aqueous species.</p>
Mineral trapping	<p>1. CO<sub>2</sub> reacts with minerals and organic matters in the geologic formations to become a portion of the solid matrix.</p> <p>2. CO<sub>2</sub> is trapped by precipitation of carbonate-bearing mineral phases, such as calcite, magnesite, siderite, and dawsonite.</p> <p>3. CO<sub>2</sub> is trapped by the mineralization process of mineral dissolution and precipitation.</p> <p>4. CO<sub>2</sub> is trapped by precipitation of dissolved carbonate anions and metal cations as solids.</p>

---

(Zhang & Song, 2014)

#### 2.1.4 CO<sub>2</sub> Properties

CO<sub>2</sub> phase behavior and properties like density and compressibility are intensely pressure and temperature-dependent because CO<sub>2</sub> is usually found around the critical point,  $T_c=31.1^\circ\text{C}$  and  $P_c = 7.38\text{ MPa}$ , in the reservoir condition. The CO<sub>2</sub> density in the standard condition is about  $1.87\text{ kg/m}^3$ , despite the fact that it varies between 300 and  $700\text{ kg/m}^3$  in the storage (van der Meer, Hofstee, & Orlic, 2009), as shown in figure 2.5. In contrast to density, the viscosity of CO<sub>2</sub> has a lower variation interval with pressure and temperature change.

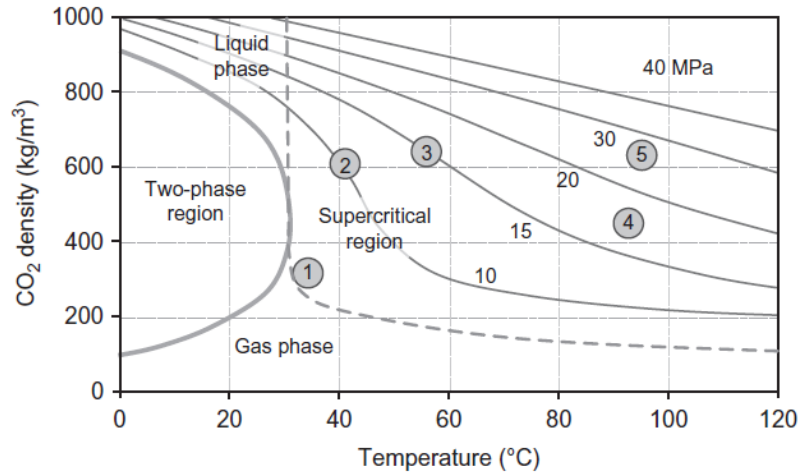


**Figure 2.5: Density of CO<sub>2</sub> as a function of temperature and pressure  
(Rackley S. A., 2017)**

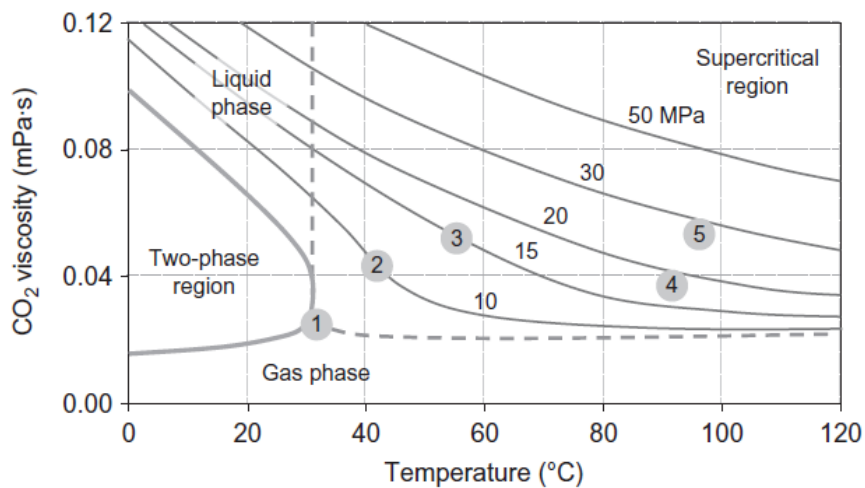


**Figure 2.6: Viscosity of CO<sub>2</sub> as a function of temperature and pressure  
(Rackley S. A., 2017)**

### 2.1.5 Rock and Fluid Interaction

CO<sub>2</sub> injection in the saline aquifer will create a 2-phase system that causes CO<sub>2</sub> migration and trapping in the porous media to be influenced by interfacial tension (IFT). Figure 2.7 indicates IFT between CO<sub>2</sub> and brine as the function of pressure, temperature, and brine salinity.

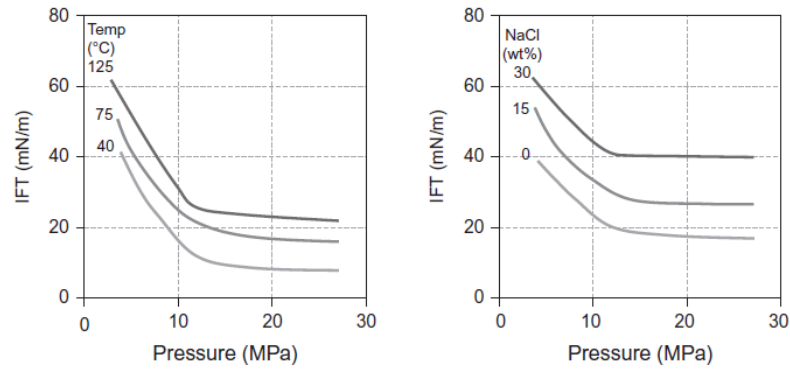


**Figure 2.7: Brine CO<sub>2</sub> IFT dependence on pressure, temperature, and brine salinity (Rackley S. A., 2017)**

Before injection, the reservoir is fully saturated by the formation water. CO<sub>2</sub> injection causes the non-wetting phase, CO<sub>2</sub>, to displace the wetting phase, water, during drainage and induces a capillary pressure and rise in consequence of the pressure difference between the two partially immiscible phases in addition to the pressure gradient of injection. While drainage, the gas saturation cannot reach one because of IFT; a small amount of water adheres to the wall of the pores, equal to the irreducible water saturation. After stopping the injection, spontaneous imbibition will be created, and the water will force CO<sub>2</sub> back to reach the phase and hydraulic equilibrium. Therefore, mostly CO<sub>2</sub> will be placed in the upper part of the storage and above the water, which has a greater density. However, the water saturation will not return to one due to immobile gas called critical gas saturation. Finally, capillary pressure will generate a transition zone in addition to the gas and water zone (Rackley S. A., 2017). Figure 2.10 demonstrates capillary pressure change versus the water saturation during drainage and imbibition. The capillary pressure can be translated to capillary height by the density difference.

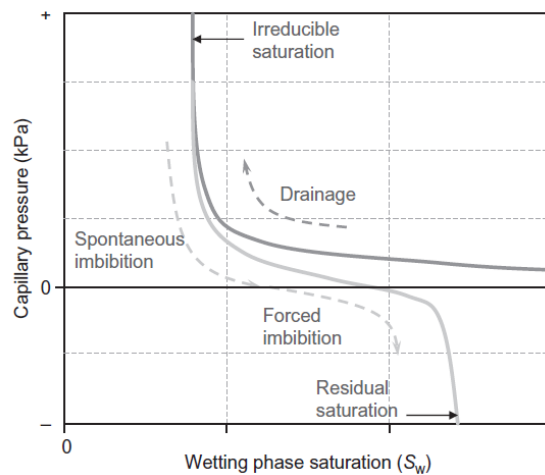


**Figure 2.8: drainage imbibition capillary pressure curves (Rackley S. A., 2017)**

2.1.6 Risk assessment of CO<sub>2</sub> Storage

Five main types of risk follow geological storage of CO<sub>2</sub> in terms of CO<sub>2</sub> leakage, CH<sub>4</sub> leakage, seismicity, ground movement, and brine displacement, which are generalized in figure 2.9 (Li & Liu, 2016). The overriding concern that must be guaranteed before the injection is CO<sub>2</sub> leakage through caprock capillary penetration, existing fractures and faults or induced fractures in caprock by pressures over fracture pressure, and legacy wells. Additionally, remedial measures for any possible leakage should be predicted, such as in figure 2.10.

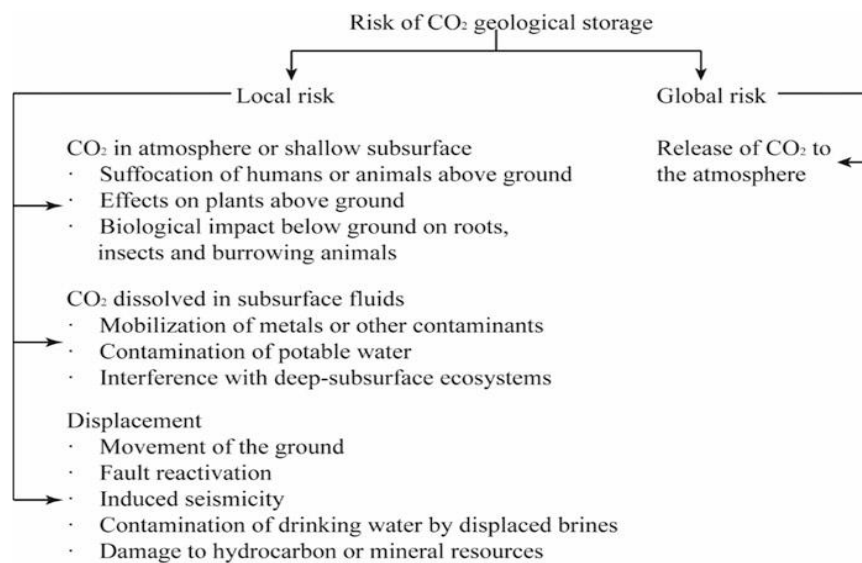


Figure 2.9: Risks associated with the geological storage of CO<sub>2</sub> (Li & Liu, 2016)

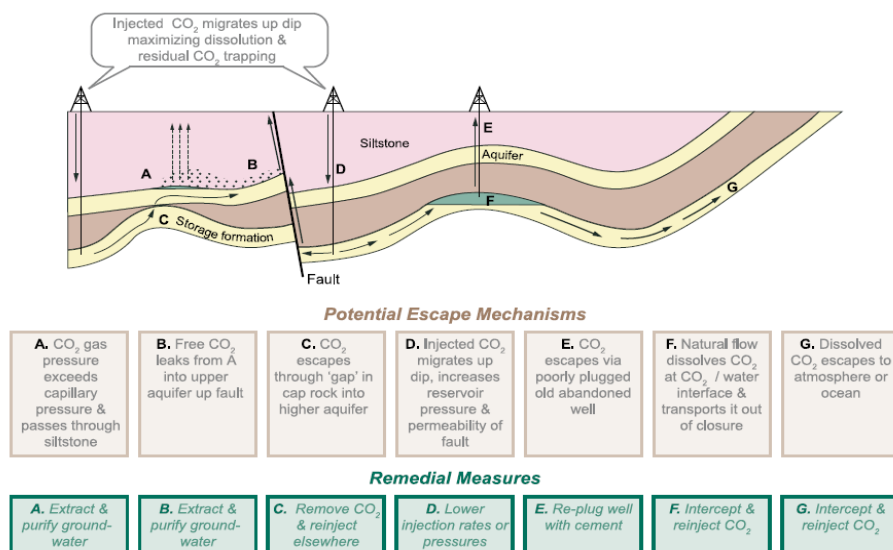


Figure 2.10: Some potential escape routes for CO<sub>2</sub> injected into saline formations and remedial measures (Metz, 2005)

## 2.2 Proxy Modeling

The nature of numerical reservoir simulation modeling involves uncertainty that requires uncertainty analysis and quantification for foolproof implementation of CO<sub>2</sub> storage. On the other hand, these models contribute to overkill computation costs owing to using non-academic and real cases, which are huge. Therefore, the utilization of numerical reservoir simulation models limits uncertainty analysis, full-field studies, and optimization. The oil & gas industry has been grappling with the mentioned problems by building proxy models (Mohaghegh, 2018), which reproduce simulation output from input features through mathematical or statistical functions, to substitute for complex reservoir simulation models (Zubarev, 2009).

Generally, there are four types of proxy models: statistics-based technique, reduced physics approach, reduced-order modeling approach, and artificial intelligence (AI)-based method. The statistical methods, such as Statistical Response Surfaces (SRSs), make a relationship between input and output parameters by a function that can be obtained by computational trials proportional to the complexity of the mathematical function. Reduced-order approaches work based on simplifying the physics of the model by making a measure of assumptions, and reducing the dimensions of the system equations matrix, respectively. Last but not least, AI-based proxy modeling employs the power of flexible AI and machine learning techniques to find highly complex relationships between input-output parameters participating in fluid flow simulation. In this study, AI-based proxy models will be used (Amini & Mohaghegh, 2019; Jaber, Al-Jawad, & Alhuraishawy, 2019)

### 2.2.1 Building SRM

Smart Proxy Models (SPMs) or Surrogate Reservoir Proxy Models (SRMs) employ AI techniques to address geological CO<sub>2</sub> storage challenges in an effective and accurate computation. SRM generation consists of four steps:

#### 1. Defining Objectives and Features

SRMs are divided into three types Field-based, Well-based, and Grid-Based, and their resolution and complexity increase, respectively, according to figure 2.11 (Matthew, 2021). the selection of the SRM type depends on the problem objective. A field-based SRM models a segment or whole of the field by the

field-scale parameters. Well-scaled proxies simulate pressure and rate change around the wellbore, and grid-based proxies monitor the alteration of pressure and saturation at each grid. Subsequently, the input features will be determined by general inputs of each proxy model in table 2.3 and the physics of the case study.

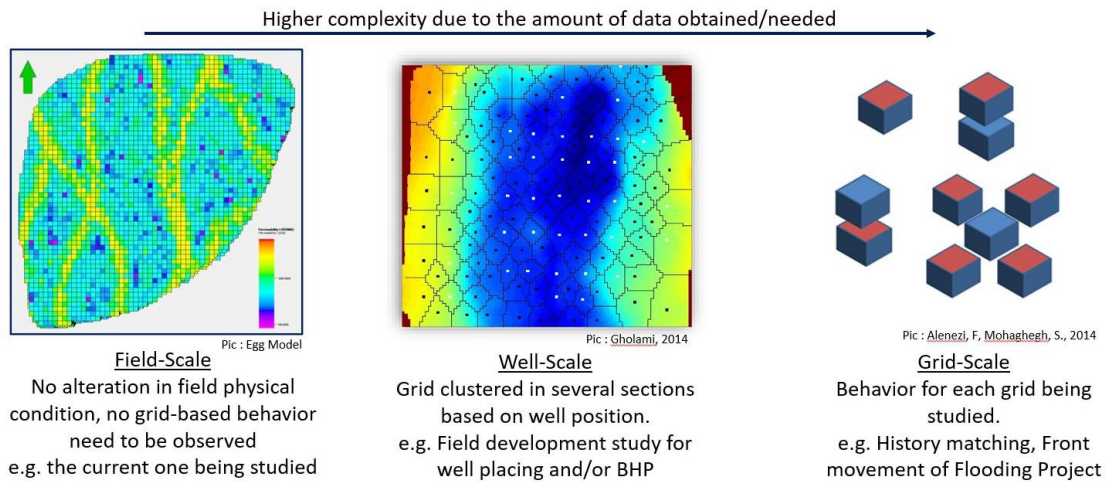


**Figure 2.11: Summary of proxy model scale and application (Matthew, 2021)**

**Table 2.3: SRM input**

DATA	Grid-based <sup>1</sup>		Well-based <sup>1</sup>		Field-based <sup>2</sup>	
	Property	Domain	Property	Domain	Property	Domain
<b>Static</b>	Grid Type	Grid	Drainage Area	Well	No input needed here (Constant geological/ static condition)	
	Location (i, j, k, x, y)	Grid/Tier	Location (i, j, k, x, y)	Well		
	Thickness	Grid	Thickness	Tier		
	Porosity	Grid	Porosity	Tier		
	Permeability (x, y, z)	Grid	Permeability (x, y, z)	Tier		
	Grid top	Grid/Tier	Grid top	Tier		
	Distance to boundary	Grid/Tier	Distance to boundary	Well		
<b>Dynamic</b>	Time		Time		Time	
	Pressure	Grid/Tier	Pressure	Tier		
	Saturation	Grid/Tier	Saturation	Tier		
	CO <sub>2</sub> mole fraction	Grid/Tier	CO <sub>2</sub> mole fraction	Tier		
	COWs <sup>3</sup> BHP	Well	COWs BHP	Well		
	COWs Amount of prod/inj (rate & cum)	Well	COWs Amount of prod/inj (rate & cum)	Well		
	Amount of prod/inj (rate & cum)	Field	Amount of prod/inj (rate & cum)	Field		

1. (Gholami, 2014)

2. (Matthew, 2021)

3. COW: Closesst offset wells

## 2. Numerical Simulation and Dataset Generation:

The SRM requires several examples for learning and building a relationship among features. Hence, numerical reservoir models will generate simulation cases with various dynamic inputs and geological perceptions. Availability of a real case can reduce geological perception uncertainty by history matching. After that, according to table 2.3 and reservoir's properties and condition, a dataset will be generated that combines input and output features to learn SRM. Each simulation scenario contains enormous data, especially on a grid-scale, leading to a long training time. Thus, data sampling is exploited for declining dataset volume based on more alternated dynamic parameters (Amini & Mohaghegh, *Application of Machine Learning and Artificial Intelligence in Proxy Modeling for Fluid Flow in Porous Media*, 2019).

## 3. Developing and Validation of SRM:

There are assorted AI and machine learning techniques for Proxy modeling that are usually applied to well-based and field-based proxies. Mohaghegh et al. (2012), Gholami (2014), and Amini (2015) developed grid-based SRMs by ANN. Until then, a few attempts existed for saturation and pressure distribution by AI methods, despite very simplified and limited applications. In this study, ANN will also be used to develop a grid-based SRM for CO<sub>2</sub> Storage in a saline aquifer.

ANN is a machine learning algorithm obtained through the network of biological neurons inside the brain. However, the ultimate version of ANN used in complex machine learning tasks differs from the simple version in the 1940s (Géron, 2019; Nayak, 2001). Generally, ANN, like other machine learning models, learns a phenomenon's historical behavior and examples to predict its future performance. Moreover, a phenomenon is described by independent parameters or features with different characteristics in each example,  $m$ . As shown in figure 2.12, An ANN includes three layers: input layer, hidden layer, and output layer, and each layer contains some units. Input layer units correspond with the phenomenon features,  $x_1, x_2, \dots, x_i$ , plus the bias unit, and the input dataset equals the number of examples,  $n$ , that characterize features in diverse behaviors.

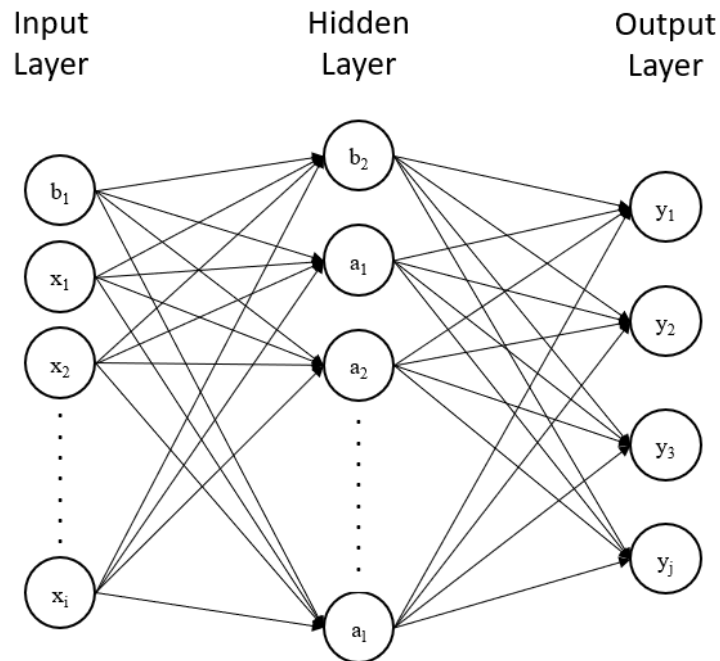


**Figure 2.12: General schematic of ANN, based on (Silva, Spatti, Flauzino, Liboni, & Alves, 2017)**

**Table 2.4: ANN input data structure**

Features	$x_1$	$x_2$	$x_i$
<b>Example 1</b>	$m_1^1$	$m_1^2$	$m_1^i$
<b>Example 2</b>	$m_2^1$	$m_2^2$	$m_2^i$
<b>Example 3</b>	$m_3^1$	$m_3^2$	$m_3^i$
.....	.....	.....	.....
<b>Example n</b>	$m_n^1$	$m_n^2$	$m_n^i$

Units of the hidden layer employ an activation function to activate weighted input data using the kernel matrix plus the bias matrix, similar to figure 2.13. The weighted outcome of the hidden layer plus its bias will be activated again by the activation function of the output layer, including units equal to predicting phenomenon. The mentioned process called Forward Propagation will contribute to the predicted result. While model training, the first forward propagation is carried out by random kernel and bias matrixes.

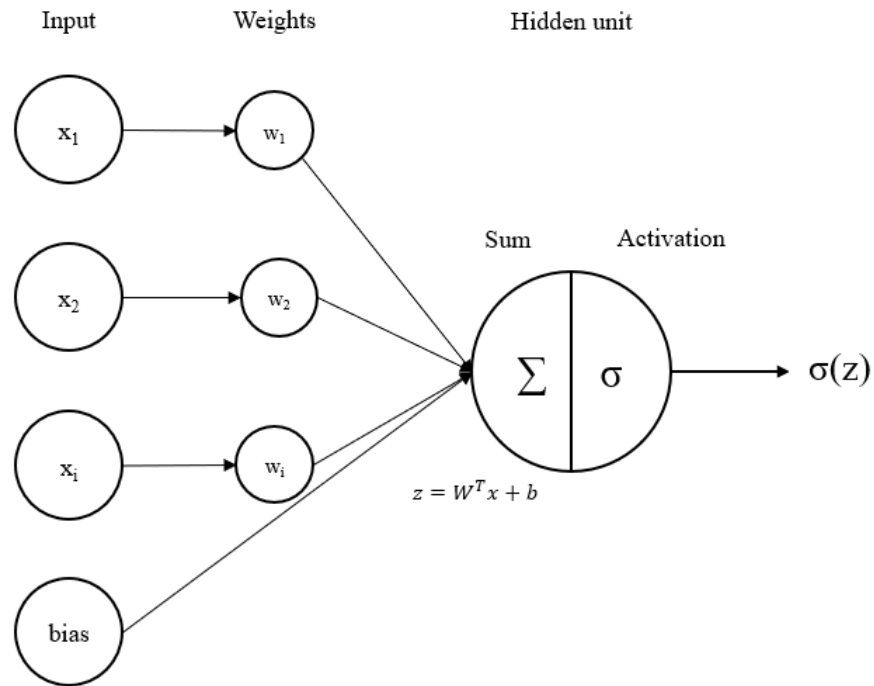


**Figure 2.13: ANN forward propagation, based on (Géron, 2019)**

Where:

$x$ : Input data matrix

$W$  = Kernel matrix

$b$  = Bias matrix

$Z$  = Weighted sum

$\sigma(z)$  = Activation function

Then, the difference between predicted values and true values will be computed by a loss function like Mean Absolute Error (MAE) and Mean Squared Error (MSE). Finally, the Back Propagation process employs the loss function to update the matrixes and reduce the prediction loss and error, proportional to the learning rate. The progress will be repeated until achieving the global minimum of the loss, and each endeavor is called one Epoch. Figure 2.14 indicates the loss function vs. the number of epochs that the more epochs, leading to less loss.

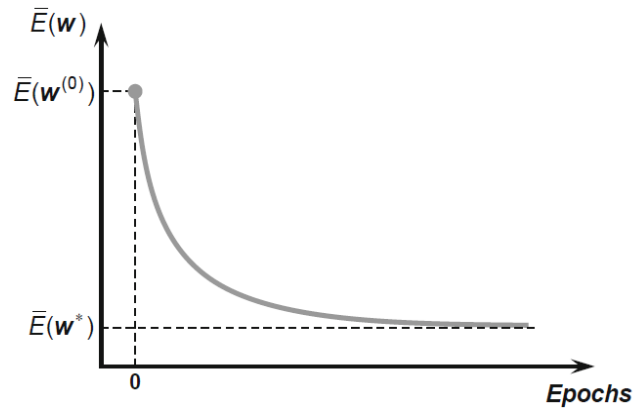


**Figure 2.14: Behavior of MSE function respect to training epochs (Silva, Spatti, Flauzino, Liboni, & Alves, 2017)**

Deep Neural Network (DNN) works the same as ANN with the difference of employing multi hidden layers. Within training an ANN, hyperparameters such as learning rate, the number of hidden layers, the number of units inside each layer, optimizer, and so on must be tuned for diverse cases by trials and error. Two main problems that may be faced during model training are underfitting and overfitting. Underfitting happens when the ANN is not trained perfectly; the model is much simpler than learning the phenomenon complexity. When the model has a great performance in training whereas it is not able to generalize well, the model is overfitted. Extending the model network, growing the learning rate as well as improving the features can overcome the underfitting. On the other hand, simplifying the model, employing regularization, and adding more data are the solutions to overfitting (Géron, 2019).

Consequently, the generated data set will be fed to an ANN to build and tune the SRM according to figure 2.15. In this regard, the dataset will be split into three groups training, validation, and test. The ratio of training data to the total data is 80% and 10% for each validation and test data. Finally, the model will be validated by a blind case that never is introduced to the model. If the model does not operate accurately, the model hyperparameters and dataset must be tuned, trained, and validated again.

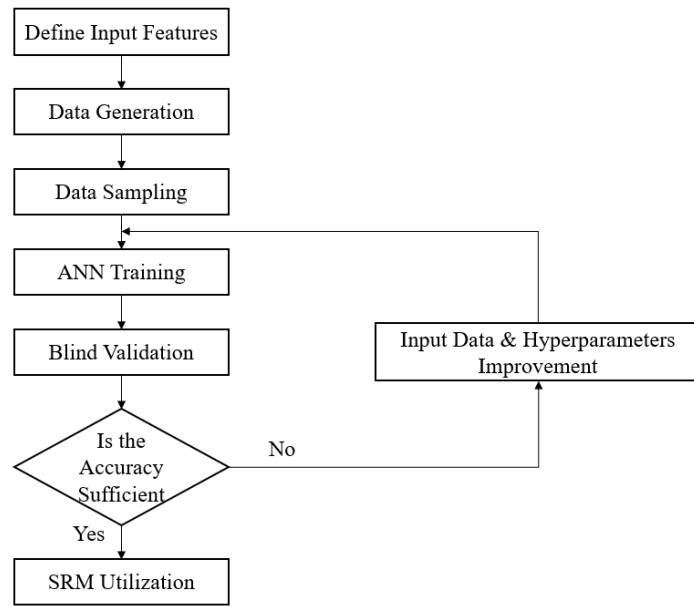


**Figure 2.15: Proxy modeling workflow, based on (Zubarev, 2009)**

#### 4. Model Implementation and Prediction:

The validated SRM can predict CO<sub>2</sub> storage performance, depending on the type of SRM, in a very short time instead of commercial simulators for uncertainty, sensitivity, and risk analysis, in addition to optimization. This study will exploit a grid-based SRM for CO<sub>2</sub> injection optimization.

##### 2.2.2 Previous studies on proxy modeling

Gholami (2014) coupled a grid-based and a well-based SRM for CO<sub>2</sub>-EOR optimization. She employed a cascading grid-based method to simulate CO<sub>2</sub> mole fraction, pressure, water saturation, and oil saturation distribution in a compositional model. Cascading method generates separate SRMs in each time step and for each parameter. According to figure 2.16, the model input in time step  $t$  is the previous model output in the time step of  $t-1$ . Accurate results are demonstrated in 2.17, 2.18, 2.19, and 2.20. Moreover, the well-based SRM modeled the oil production rate and cumulative oil production in production wells. Figure 2.21 compares the SRM<sub>w</sub> result and numerical simulation output.

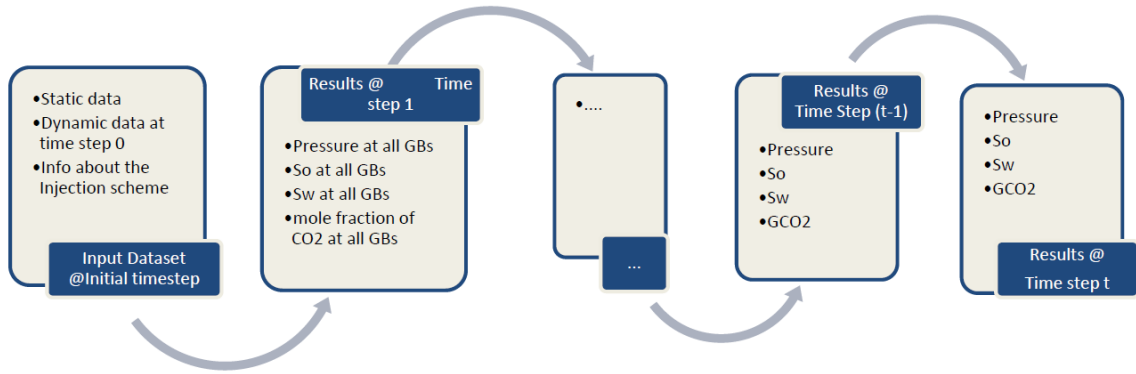


Figure 2.16: Grid based cascading flow-chart (Gholami, 2014)

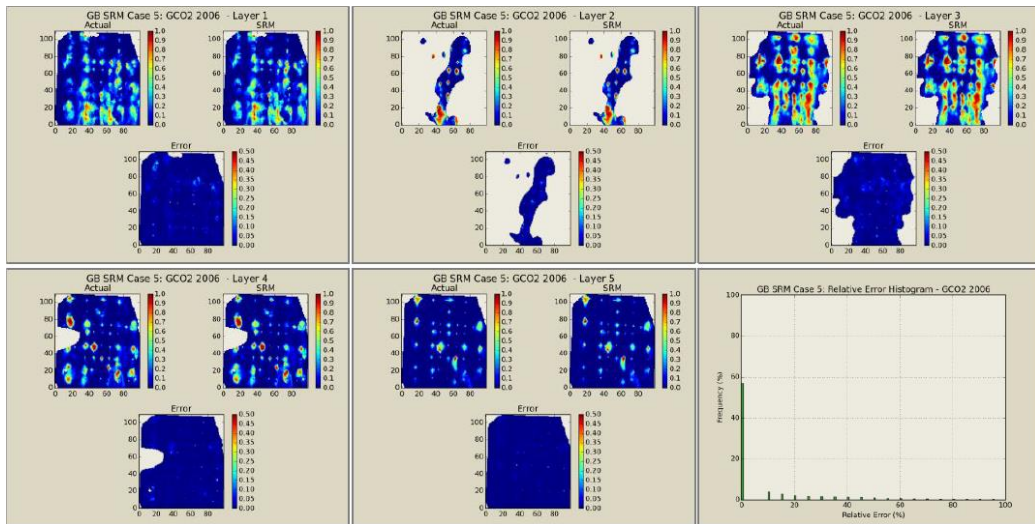


Figure 2.17: CO2 mole fraction distribution map (Gholami, 2014)

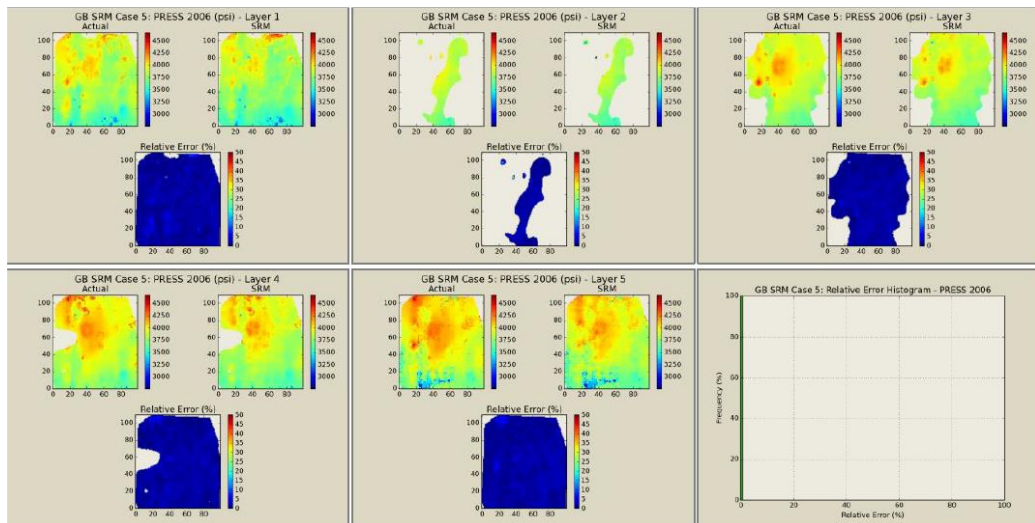


Figure 2.18: Pressure distribution map (Gholami, 2014)

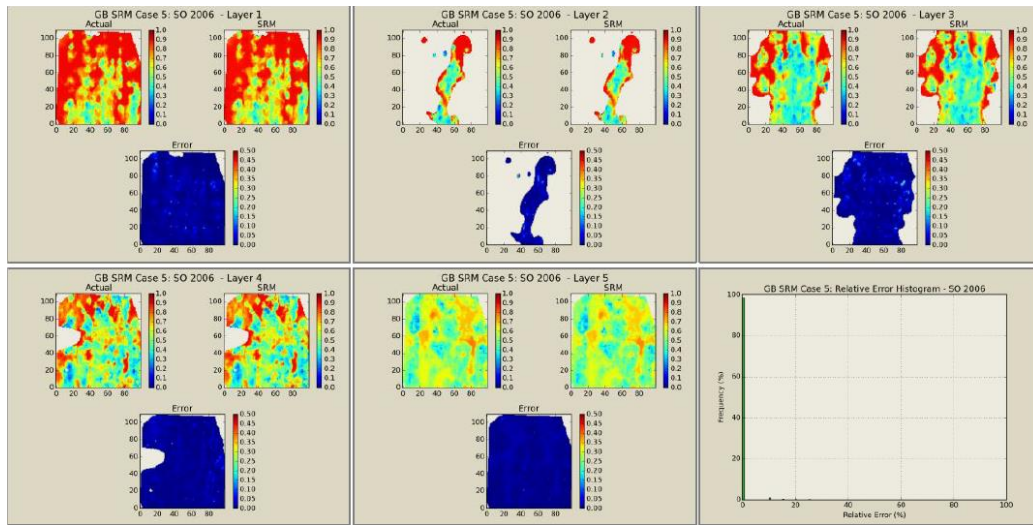


Figure 2.19: Oil saturation distribution map (Gholami, 2014)

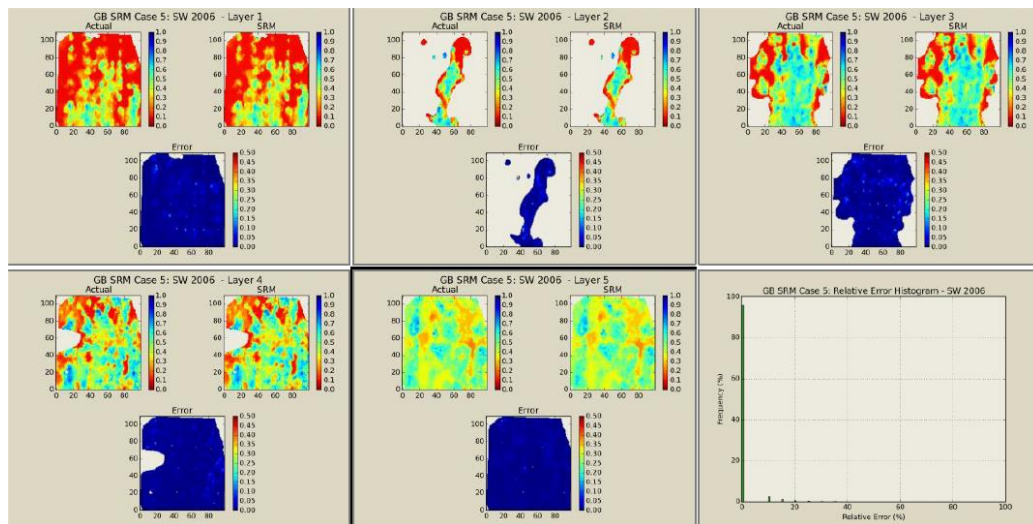


Figure 2.20: Water saturation distribution map (Gholami, 2014)

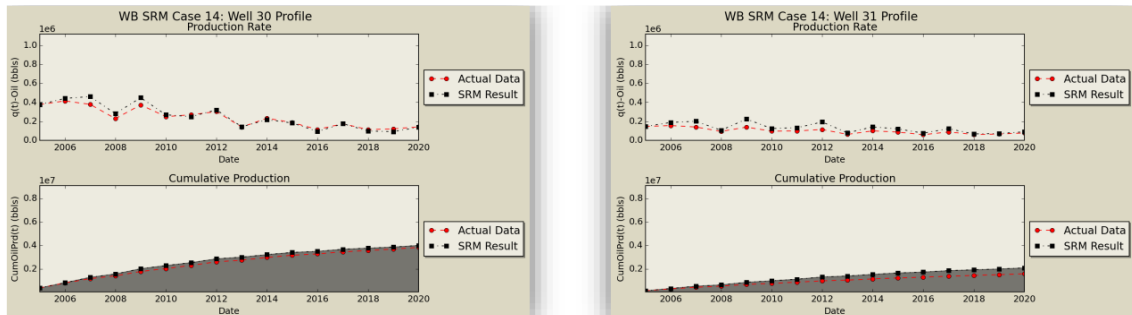
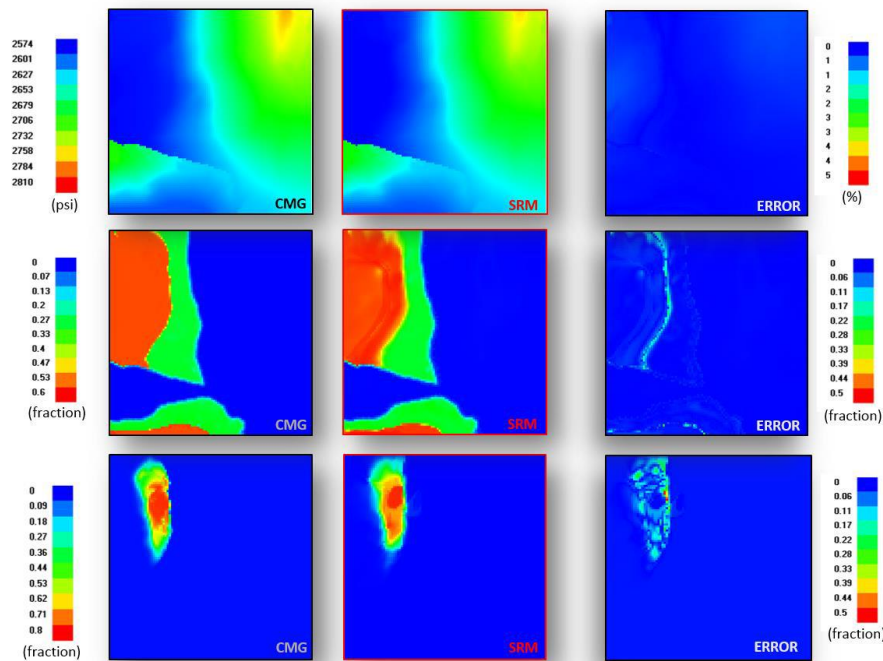


Figure 2.21: Oil production by SRMw (Gholami, 2014)

Amini (2015) developed both cascading and non-cascading grid-based full-field SRMs for coarse and fine grid models. In contrast to cascading, the non-cascading method develops one model for the whole simulation time per parameter, and only the initial condition of dynamic parameters at time step zero is fed to the model. Consequently, the cascading SRM<sub>G</sub> caused the error of each time step to accumulate with the last time steps and less accuracy than the non-cascading technique. Furthermore, the non-cascading SRM<sub>G</sub> developed by the fine-grid model results in more accuracy for the pressure and more error for the saturation in comparison with the coarse-grid model. The non-cascading fine-grid SRM<sub>G</sub> for the pressure, CO<sub>2</sub> saturation, and CO<sub>2</sub> mole fraction led to figure 2.122.



**Figure 2.22: Distribution maps of Pressure, Gas saturation and CO<sub>2</sub> mole fraction (from left: CMG output, SRM result and Error) (Amini, 2015)**

### 2.3 Optimization

Optimization involves finding the best solution under the circumstances. Frequently, in the progress of engineering projects, critical decisions should be made to minimize costs and maximize the benefit (Rao, 2019). In this regard, mathematical models are constructed to describe the project, and predict and optimize its implication. A model can possess different output properties that lead to more than one acceptable design. Thus, a criterion must be selected to find the optimum design. The function  $f(x)$  with the design

variable vector  $x \in \mathbb{R}^n$ , as the optimization criterion, is called the Objective Function (Hendrix, Boglárka, & others, 2010). A problem that must satisfy multiple criteria and requires more than one objective function is a multi-objective optimization problem. Additionally, there may be some restrictions on design variables selection: Inequality Constraints,  $g(x)$ , and Equality Constraints,  $h(x)$ . In a constrained optimization problem, the limitations must be satisfied in parallel to objective functions (Snyman & Wilke, 2018).

$$\begin{aligned} \text{minimize } f(x), \quad x &= [x_1, x_2, \dots, x_n]^T \in \mathbb{R}^n \\ g_j(x) &\leq 0 \quad j = 1, 2, \dots, m \\ h_j(x) &= 0 \quad j = 1, 2, \dots, r \end{aligned} \tag{2.1}$$

Where:

$x$  = Design variable vector

$n$  = The number of problem variables

$m$  = The number of inequality constraints

$r$  = The number of equality constraints

As mentioned before, the best solution, minimum or maximum, will be chosen as the Global Optimum, and no existing better solution, plan, or design. Although, there are Local Optimums that are only optimum points in their neighborhoods, as illustrated in figure 2.23. The presence of local optimums can be a challenge in optimization because they may be mistaken for the global optimum.

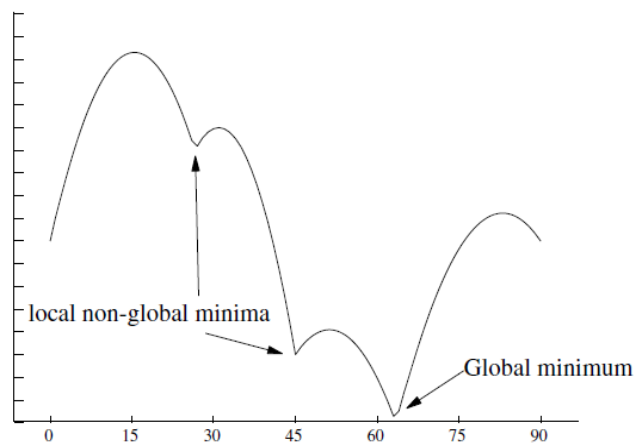


**Figure 2.23: Global optimum & local optima (Hendrix, Boglárka, & others, 2010)**

### 2.3.1 Optimization for CO<sub>2</sub> storage

CO<sub>2</sub> injectivity and containment are two vital elements of subsurface CO<sub>2</sub> storage (Harding, James, & Robertson, 2018) that should be maximized as the project's objectives. Primary parameters which must be optimized can be listed as follows (Ettahadtavakkol, Lake, & Bryant, 2014):

#### 1. **Well Design and Placement:**

An injection well must be able to deliver CO<sub>2</sub> to the depth of subsurface geological storage at an appropriate pressure and transmit it to the reservoir without exceeding the bottom hole fracture pressure. Moreover, well location should be chosen concerning CO<sub>2</sub> immobilization and trapping. Therefore, well location, perforation location and length, tubing size, surface facilities, etc. require optimization (Kuk, Kuk, Janiga, Wojnarowski, & Stopa, 2020).

#### 2. **CO<sub>2</sub> Injection Rate:**

Despite injection rate dependency on CO<sub>2</sub> availability, the maximum possible rate must not lead to fracturing and CO<sub>2</sub> plume migration toward possible leakage points (Cameron & Durlofsky, 2012).

#### 3. **Injection Duration:**

The field cumulative CO<sub>2</sub> injection volume is the function of the Injection rate and duration. Depending on the type and goal of the CO<sub>2</sub> injection Water Alternate Gas (WAG) cycle or CO<sub>2</sub> injection period requires optimization. In CO<sub>2</sub>-EOR, the WAG cycle is an uncertain variable that should be optimized to obtain the maximum storage capacity and recovery factor. While CO<sub>2</sub> storage in saline aquifers only involves CO<sub>2</sub> injection for a span to maximize storage capacity without any risk (Ampomah, et al., 2017; Santibanez-Borda, 2019).

Economic efficiency is a priority in all industrial projects that can be considered an objective besides storage capacity to achieve the CCS goals with the lowest cost. Indeed, SRMs can be exploited for CO<sub>2</sub> storage optimization alone or coupled with each other, depending on the objectives and uncertain variables.

### 2.3.2 Genetic algorithm

Holland (1975) was the first to develop GA, which was popularized by David Goldberg while solving a complex problem for the control of the gas-pipeline transmission

(Goldberg, 1983). GA is an optimization and search method based on genetic principles and natural selection. It helps a population, including a certain number of individuals, to produce a new generation leading to maximum fitness or minimum cost function (Haupt & Haupt, 2004). Widespread use of GA is because of its advantages over compliance with both continuous and discrete values, the simultaneous search of several samples from cost surface, no limitation in the number of variables, capability to escape from local optimums, and compatibility with numerically generated data, experimental data, or analytical functions.

Algorithm 2.1 indicates a basic genetic algorithm procedure. The total population includes  $N_{\text{pop}}$  individuals or chromosomes, which are all possible solutions, and each individual or chromosome is built on  $N_{\text{var}}$  variables or genes. Individual genes can be represented in bits, numbers, trees, arrays, lists, or other objects by Encoding, the process of converting gene values (Sivanandam & Deepa, 2008).

---

#### **Algorithm 1: Basic Genetic Algorithm**

---

```

1: initialize population
2: repeat
3:   repeat
4:     crossover
5:     mutation
6:     phenotype mapping
7:     fitness computation
8:   until population complete
9:   selection of parental population
10: until termination condition

```

---

(Kramer, 2017)

The initial population is a random matrix with the  $N_{\text{pop}}*N_{\text{var}}$  dimension. While initialization, the objective function for decoded individuals, real values, will be calculated. The obtained value for an individual is called its Fitness, revealing the equality of solution as well as closeness to the optimal chromosome. Decoding of gene values is performed by Genotype-Phenotype Mapping, which converts genotypes to phenotype, actual solution (Kramer, 2017). In the case of using continuous solutions, real values need not decode the genotype, and only normalized values must be denormalized. After fitness computation, two parents will be selected to reproduce the new generation. Ranking Selection, one of the best selection approaches, ranks the individuals according to their

fitness. The best parents are chosen by a selection ratio to pick two required parents among them randomly (Haupt & Haupt, 2004). Crossover, by swapping single or multi-genes of parents, and Mutation, by random evolution of some genes inside the solution interval, reproduce a new generation (Sivanandam & Deepa, 2008).

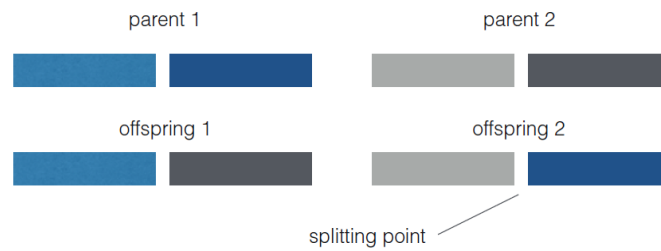


**Figure 2.24: One-point crossover that splits up the genome of two solutions at an arbitrary (Kramer, 2017)**

The foremost task of Mutation is preventing the algorithm from sticking to a local optimum by declining the tendency of GA to quick convergence (Haupt & Haupt, 2004). Algorithm 2.2 controls the mutation rate in the way of the global optimum. Finally, the new generation will replace the weak parents. The replacement too can be done randomly, or two parents can be replaced; however, they may disturb the search convergence by eliminating good individuals. Lastly, each individual's fitness in the new population is computed, and the loop will be repeated to reproduce the next generations until achieving Termination or Convergence criteria.

---

**Algorithm 2:** Global mutation rate control

---

```

1: repeat
2:   mutate local optimum
3:   local search
4:   if same local optimum, then
5:     increase mutation rate
6:   else
7:     decrease mutation rate
8:   end if
9: until termination condition

```

---

(Kramer, 2017)

The most straightforward strategy to handle constraints in GA is using Death Penalty, according to algorithm 2.3, which checks the feasibility of constraints after crossover and

mutation. In the condition of constraints' unfeasibility, the loop will be repeated until satisfying them.

---

**Algorithm 3:** Death penalty

---

1: **repeat**  
2: crossover  
3: mutation  
4: check constraints  
5: **until** solution is feasible

---

(Kramer, 2017)

Another method to tackle constraints is employing a penalty function to degenerate the fitness of an unfeasible solution and make it less applicable for selection by equation 2.2. Repair, Decoder, and Premature Stagnation are other options to overcome constraints in GA (Kramer, 2017).

$$f'(x) = f(x) + \alpha * g(x) \quad (2.2)$$

Where:

$f(x)$  = Objective function

$g(x)$  = Constraint function

$f'(x)$  = Penaltalized objective function

$x$  = Variable vector

$\alpha$  = Penalty factor

---

### 3 METHODOLOGY, PROBLEM, AND MODEL DESCRIPTION

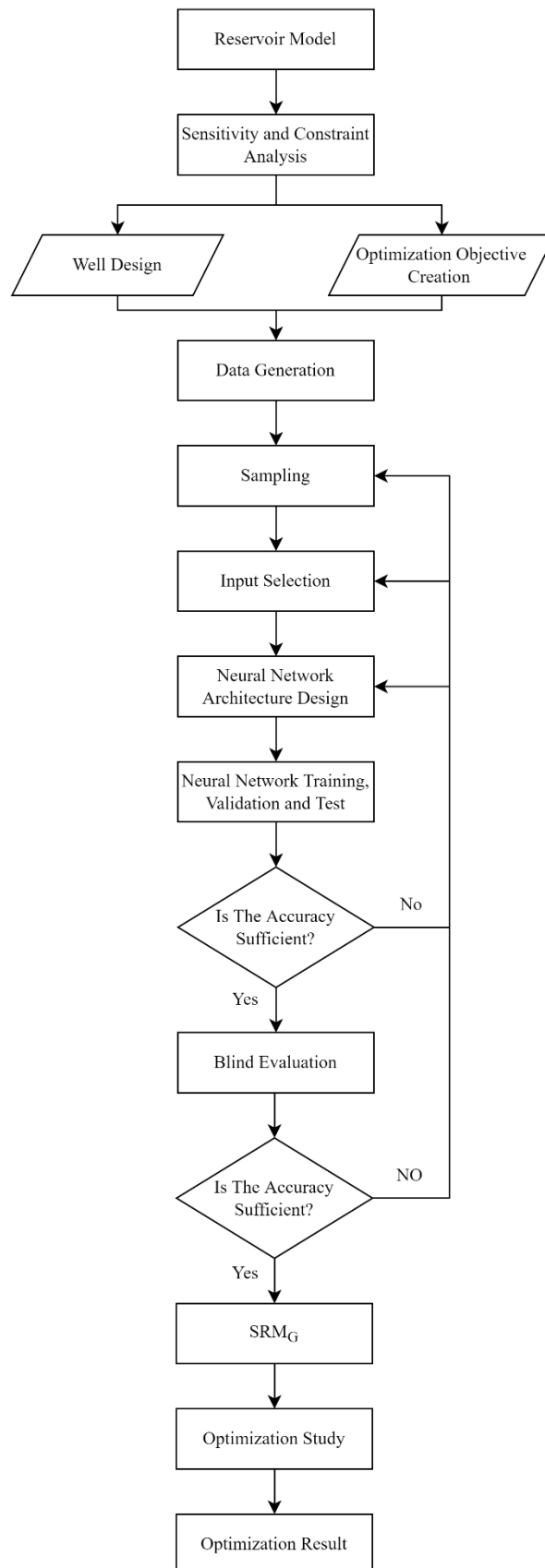
Previous studies proved the competence of grid-based SRMs in CO<sub>2</sub>-EOR and CO<sub>2</sub> storage simulation and optimization. However, the studies' time intervals have been limited to a few months or years. Gholami (2014) simulated CO<sub>2</sub>-EOR for 15 years, and Amini (2015) for 24 months. Growth in the prediction time can be challenging in terms of Processing an extensive dataset, the model training time, and error accumulation.

Moreover, repeatedly CO<sub>2</sub> injection rate and time interval optimization, and pressure and migration path control are performed by numerical models, which may require more than 12 hours for a long-term simulation. Therefore, a gap exists in developing grid-based proxy models to be substituted for numerical models in the long-term simulation and optimization of CO<sub>2</sub> storage.

In this research, two proxy models will be created for saturation and pressure distribution prediction in a 50-year CO<sub>2</sub> injection interval. The Smeaheia model (Equinor & Gassnova, 2021) from Eqiunor (Statoil) will be used to simulate CO<sub>2</sub> storage in a saline aquifer and generate data. The models will be employed in an optimization problem. In this chapter, the study workflow and reservoir characteristics will be described. Additionally, the reservoir model will be updated before proxy modeling.

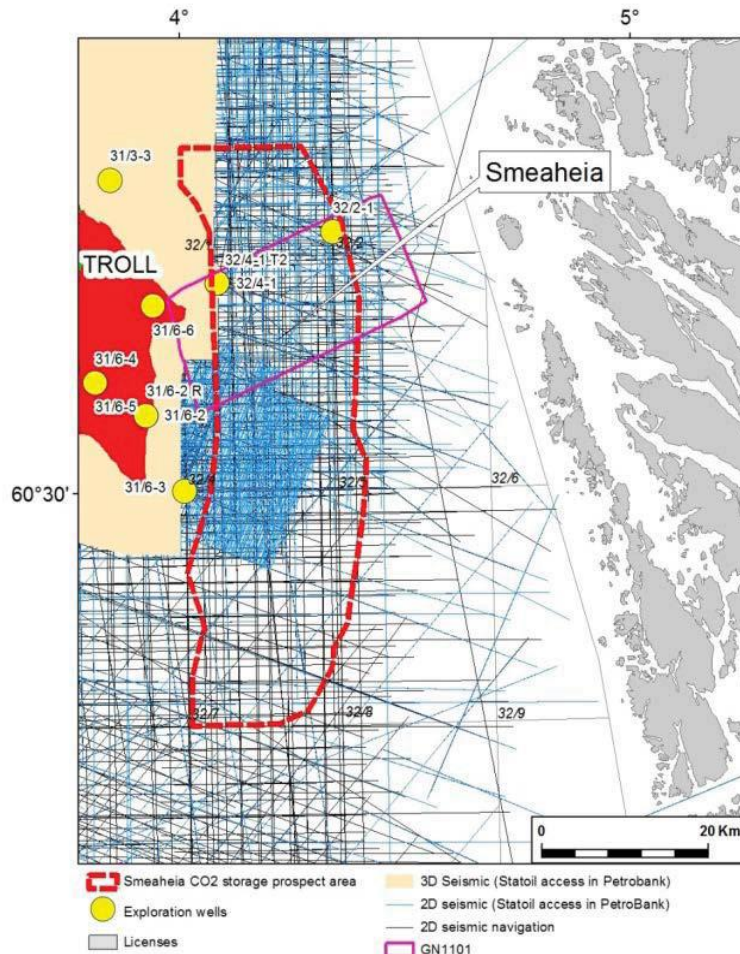
#### 3.1 Study Workflow

Figure 3.1 demonstrates the thesis workflow based on previous studies in CO<sub>2</sub> storage analysis, proxy modeling, and optimization, as well as trial and error during implementation. Finally, the workflow has been confirmed by the final result of the study.

**Figure 3.1: Study workflow**

### 3.2 Reservoir Description

The Smeaheia CO<sub>2</sub> storage prospect evaluated in this study lies on the Horda Platform east of the Troll field, mainly in Blocks 32/4 and 32/1, see Figure 3.2. The studied area is approximately 20km east of the Troll A platform and 40km northwest of the Kollsnes gas terminal.



**Figure 3.2: Smeaheia outline and location of this study's AOI: GN1101 3D seismic survey (Statoil, 2016)**

The AOI was chosen based on the maturity of previous works on CO<sub>2</sub> storage in this area (internal and external) and the availability of seismic data. A pre-requisite for this feasibility study was to investigate areas with little need for additional data acquisitions before a potential investment decision. Therefore, it was decided to focus on the area covered by the 3D survey GN1101. The regions, called Alpha and Beta, have been tested by exploration wells. Both wells, 32/4-1 and 32/2-1 were dry even though both confirmed good reservoirs (Sognefjord- and Fensfjord formations) and thick sealing formations

(primary seal: Draupne shales). There is also additional storage potential in the underlying Triassic Lunde Fm.

### 3.2.1 Geology and Stratigraphy

The tectonic activities and faulting of the North Sea at the beginning of Permian times dictated the geological evolution and depositional setting of the Horda Platform. On the Horda Platform, the Viking Group is composed of the shallow-marine Krossfjord, Fensfjord, and Sognefjord formations. Furthermore, basin-wide flooding led to the deposition of mudstones in the Draupne formation. Figure 3.3 shows the field stratigraphy.

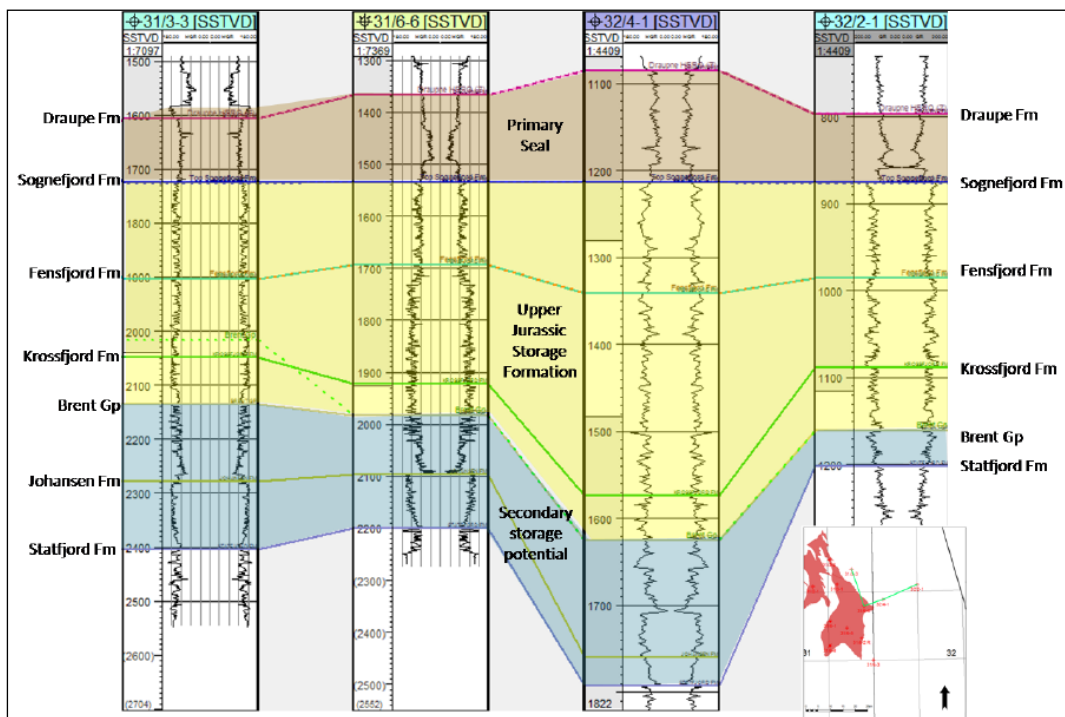


**Figure 3.3: Correlation of the wells on the Smeaheia fault block (Erichsen, Rørvik, Kearney, & Haaberg, 2013)**

The Krossfjord formation was deposited during the initial phases of the rifting period. The progradation of sand-rich deltas characterizes it during relatively low normal faulting and fault-block rotation rates.

The Fensfjord formation eventually covered the whole Horda Platform. The formation consists of well-sorted, fine to medium-grained sandstones where calcite cemented sandstones occur in bands, and minor shale intercalations occur throughout the formation.

In the late Callovian, fault-related subsidence outpaced sediment supply, and landward migration of the Fensfjord Delta happened. Meanwhile, fault-related activity created footwall islands which supplied additional sediment input.

The Sognefjord formation is the main reservoir in the Troll area. The formation is 100-170 m thick, and unique target sands are 3-45m with permeability ranging from 1-20 Darcy. These sands alternate with finer-grained micaceous units. In addition, calcite cemented zones can be discovered in both Sognefjord and Fensfjord, commonly made of a couple of meters thick and a lateral extend between tens of meters to a few kilometers.

The Draupne formation is the primary caprock to the Smeaheia storage complex and consists of marine, organic-rich claystone (figure 3.4). The Troll Field wells verify the trapping capacity of the Draupne formation, which is supposed to be present over the whole fault block. Limestone and shales of the Shetland and Cromer Knoll groups equip the storage complex with secondary seal units. Tertiary and Quaternary deposits are also assumed to boast sealing capability. The gross seal is approximately in a range of 750m and 1200m over the modeled CO<sub>2</sub> plume areas (figure 3.5).

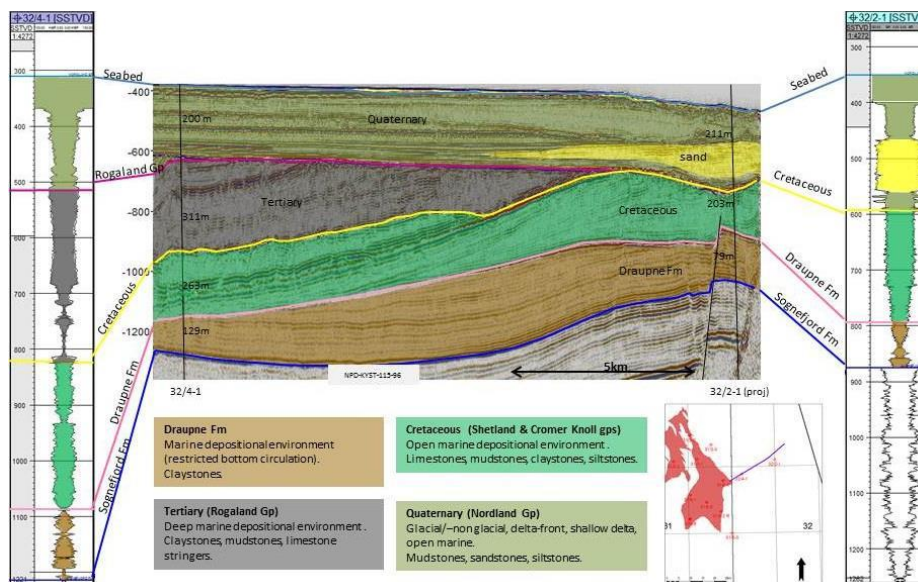


**Figure 3.4: Storage complex main seal units identified by well correlation and seismic interpretation (Erichsen, Rørvik, Kearney, & Haaberg, 2013)**

The primary seal is thinned both eastward and westward parallel to the storage thinning from west to east. Indeed, the primary seal thickness varies from 70m to 300m. The well 32/4-1 and 32/2-1 penetrated over 200m of mudstones and limestones representing the Shetland and Cromer Knoll groups in figure 3.4. The thickness map (figure 3.5) shows that the secondary seal unit varies between approximately 250m and 450m in the modeled CO<sub>2</sub> plume area.

The Smeaheia storage site is a portion of Troll Kystnær fault block located on the northeast region of the Horda Platform (Figure 3.6), east of the Viking Graben. Major faults bound the fault block to the west, north, and east (Figure 3.7). To the north and west, the storage formation constitutes the footwall of the Vette fault. In contrast, to the east, the storage location is limited by the hanging wall of the Øygarden Fault Complex (ØFC), which reflects a substantial sealing capacity in evaluations. The ØFC generates the border between the Norwegian territory to the east and the Horda Platform to the west. The ØFC and Vette fault are two out of several major faults between the shore of Norway and the North Viking Graben.

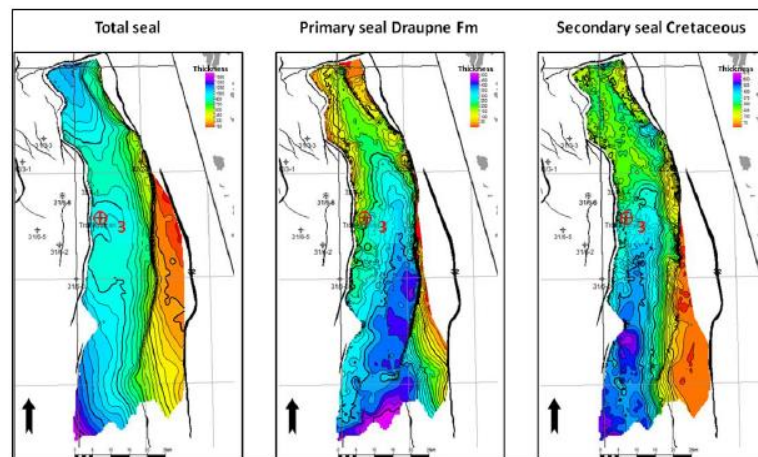


**Figure 3.5: Main seal unit thickness (m) maps for the Smeaheia Storage Complex (Erichsen, Rørvik, Kearney, & Haaberg, 2013)**

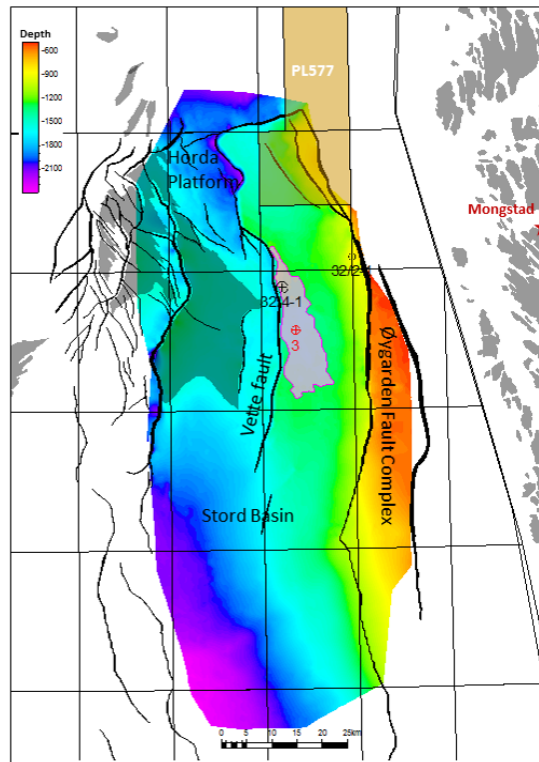


Figure 3.6: Storage formation (Erichsen, Rørvik, Kearney, & Haaberg, 2013)

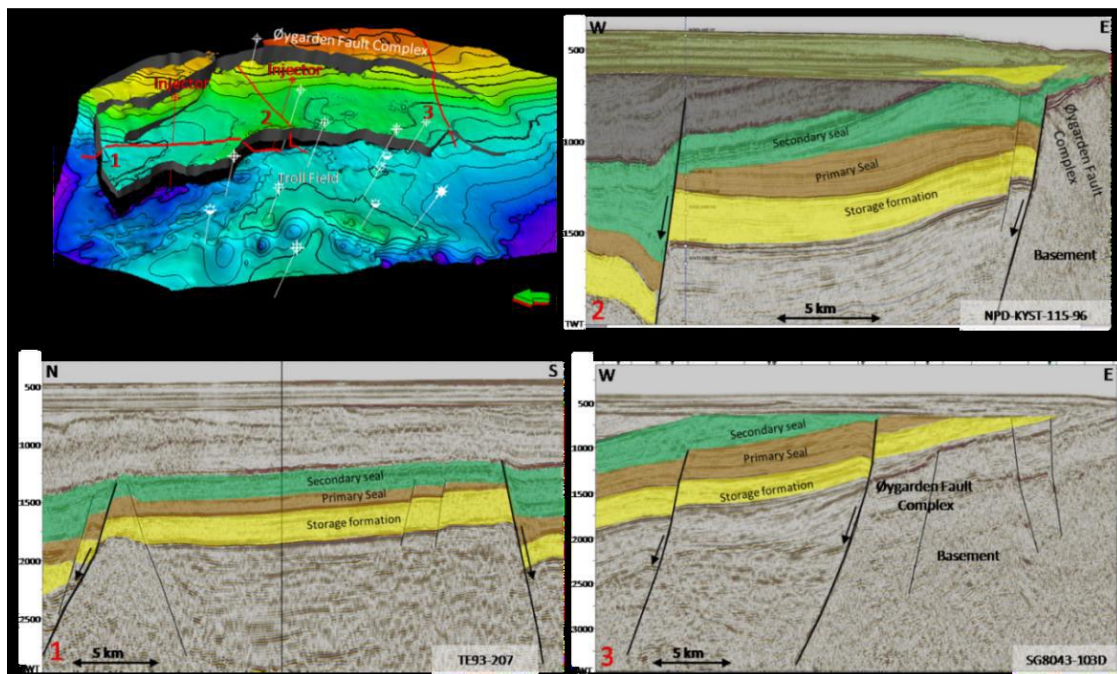
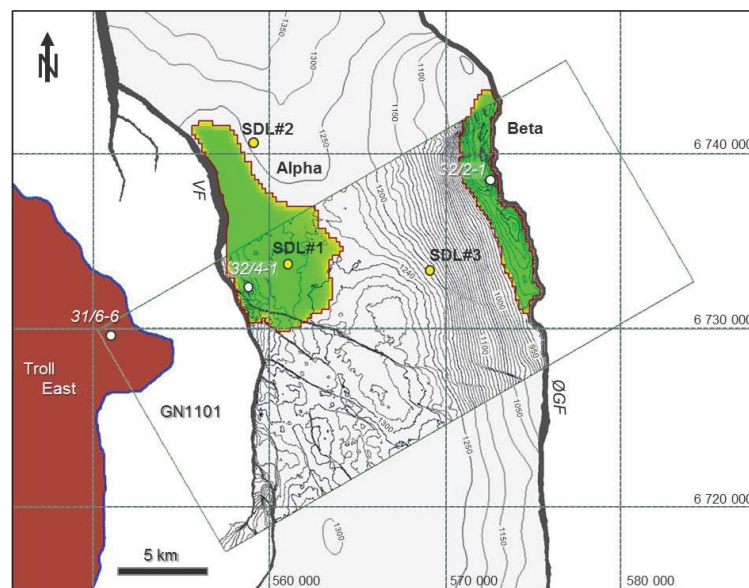


Figure 3.7: Structural setting of the Smeaheia storage site, where the location of each seismic profile is posted on the Top Sognefjord Fm depth map in the upper left corner (Erichsen, Rørvik, Kearney, & Haaberg, 2013)

### 3.2.2 Prospects Characteristics

The Smeaheia CO<sub>2</sub> storage is composed of 3 prospects: Alpha, Beta, and Gamma. As shown in figure 3.8, the majority of Alpha and Beta are covered by the GN1101 survey, making them more reliable for investigation. Although, the Gamma zone carries a considerable storage potential due to its extension. Table 3.1 and table 3.2 indicates the general characteristics of zones Alpha and Beta, respectively. Moreover, the in-situ CO<sub>2</sub> density is used to compute the capacity of each zone.



**Figure 3.8: Alpha and Beta prospect location in respect to GN 101 survey and Smeaheia storage (Statoil, 2016)**

**Table 3.1: Structural capacity estimate for Alpha prospect**

Property	Low	Mid	High
Bulk rock volume (m <sup>3</sup> )	634 000 000	634 000 000	634 000 000
Net (%)	75	85	95
Permeability (mD)	440	1300	4000
Porosity (%)	31	35	39
Saturation (%)	70	80	90
Structural capacity (Mt)	82.7	98.6	117

(Statoil, 2016)

**Table 3.2: Structural capacity estimate for Beta prospect**

Property	Low	Mid	High
Bulk rock volume (m <sup>3</sup> )	669 000 000	669 000 000	669 000 000
Net (%)	75	85	95
Permeability (mD)	440	1300	4000
Porosity (%)	31	35	39
Saturation (%)	70	80	90
Structural capacity (Mt)	87.8	105	124

(Statoil, 2016)

### 3.2.3 Stress Model and Geomechanical Properties

The acquired data from wells 31/6-3, 31/6-6, 31/3-3, and 31/6-2 in the Eastern Troll and wells 32/2-1 and 32/4-1 in Troll Kystnær by drilling tracks, logs, pressure measurement, and LOT, created a stress model for the Smeaheia storage. Thus, the specific gravity of overburden stress, pore pressure, fracture pressure, and minimum horizontal stress is plotted in figure 3.9. Besides, the interpretation of test results on the wells 32/2-1 and 32/4-1 cores revealed the rock mechanic properties of Smeaheia formations in table 3.3.

**Table 3.3: Smeaheia rock mechanic data**

Formation	UCS (Mpa)			Elastic modulus (Gpa)			Poisson's ratio			Bulk modulus (Gpa)			Uniaxial compaction modulus (Gpa)			Cohesion (Mpa)*	Friction angle (deg)*
	P10	Mean	P90	P10	Mean	P90	P10	Mean	P90	P10	Mean	P90	P10	Mean	P90		
<b>Draupne</b>	--	--	--	2	5	7	--	0.4	--	--	--	--	--	--	--	7	13
<b>Heather</b>	13	15	17	4	4	5	0.19	0.22	0.24	2	3	3	5	5	6	5	15
<b>Sognefjord</b>	9	15	19	3	5	6	0.20	0.24	0.29	2	3	5	4	6	9		
<b>Fensfjord</b>	11	19	25	4	7	9	0.19	0.24	0.28	2	4	7	5	8	12		
<b>Krossfjord</b>	16	25	34	5	8	11	0.18	0.22	0.27	2	5	8	6	9	15		

\*Recommend considering variations of +/- 25% to these values

(Equinor &amp; Gassnova, 2021)

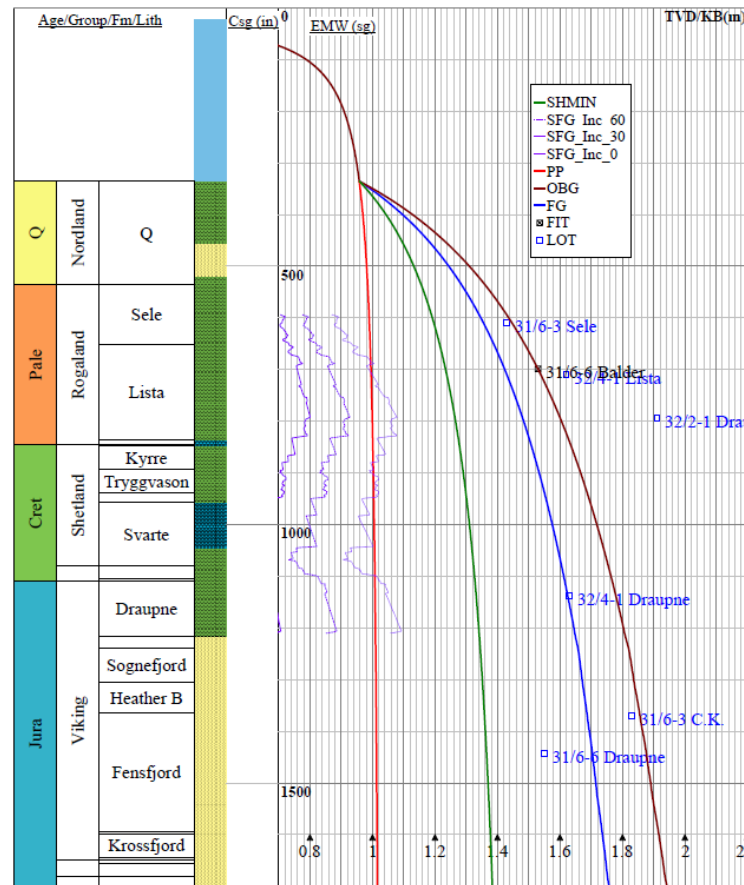


Figure 3.9: Smeaheia stress model (Equinor & Gassnova, 2021)

### 3.3 Reservoir Model

Up to now, many models have been generated for Smeaheia CO<sub>2</sub> storage with diverse geological perceptions, property distribution, covered area, and depletion scenarios. Gassnova and Statoil also developed their own models, which have been published in CO<sub>2</sub> DataShare (Equinor & Gassnova, 2021). After investigating the available models, Statoil's model was selected for this study because of considering property heterogeneity. The geological model, fluid model, and rock and fluid interaction will be discussed in the following.

#### 3.3.1 Geological Model and Properties

The geological model consists of 101 horizons resulting from gathering 2D and 3D seismic surveys and wells correlation in Smeaheia. The model and horizons cover from the top of the Sognefjord formation to the bottom of the Krossfjord formation and extend from the south to the north between the Vette fault, in the west of storage, and the

Øygarden fault complex, in the east in figure 3.11. The lateral mesh was created with a resolution of 200\*200 m regularly, and the reservoir depth was divided into 100 layers with a 1.6m resolution.

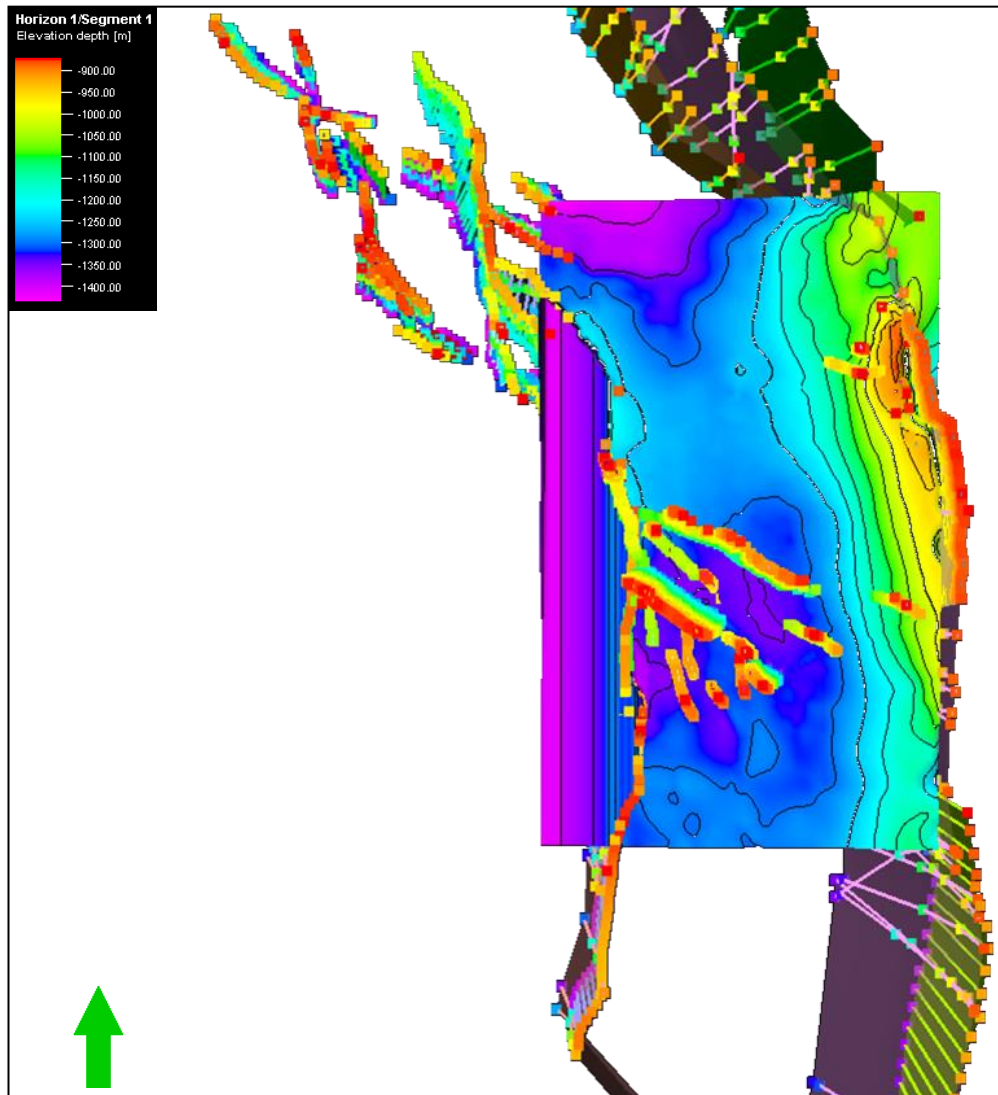


**Figure 3.10: Smeaheia model's faults and horizons**

In this model, the opposite of Gassnova's model, which only assumed vertical heterogeneity in a way that an average property value has been assigned to all grid blocks in each layer, both vertical and horizontal heterogeneities are picked, and Porosity and permeability are diverse in each layer. Figure 3.11 indicates random and irregular distribution patterns regarding permeability and porosity, respectively.

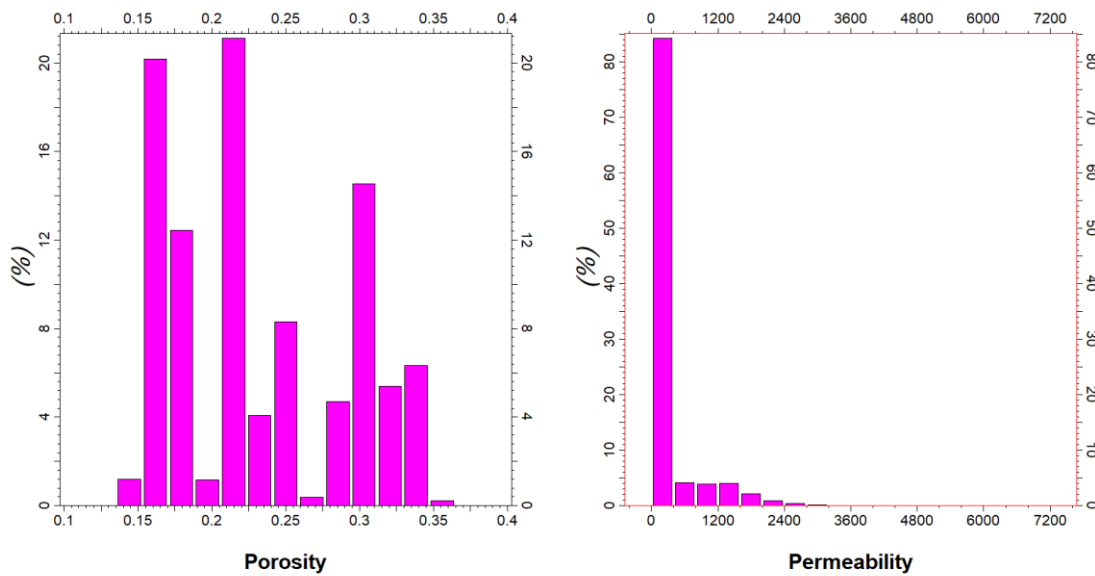


**Figure 3.11: Probability distribution of porosity and permeability**

### 3.3.2 Fluid Model

Statoil is employed a black-oil fluid model for CO<sub>2</sub> injection in Smeaheia in a way that there are 2 phases of gas and oil instead of CO<sub>2</sub> and aquifer. In this regard, the PVT properties of CO<sub>2</sub> and aquifer are plotted in figure 3.12. Moreover, table 3.4 represents the reservoir's initial condition in 1999.

**Table 3.4: Initial Condition**

Property	Initial Value
Datum depth	-800 m
Pressure	81 bar
Oil density (aquifer)	1026.0302 kg/m <sup>3</sup>
Gas density	1.872 kg/m <sup>3</sup>
Rock compressibility @ P=10 bar	4E-05 bar <sup>-1</sup>

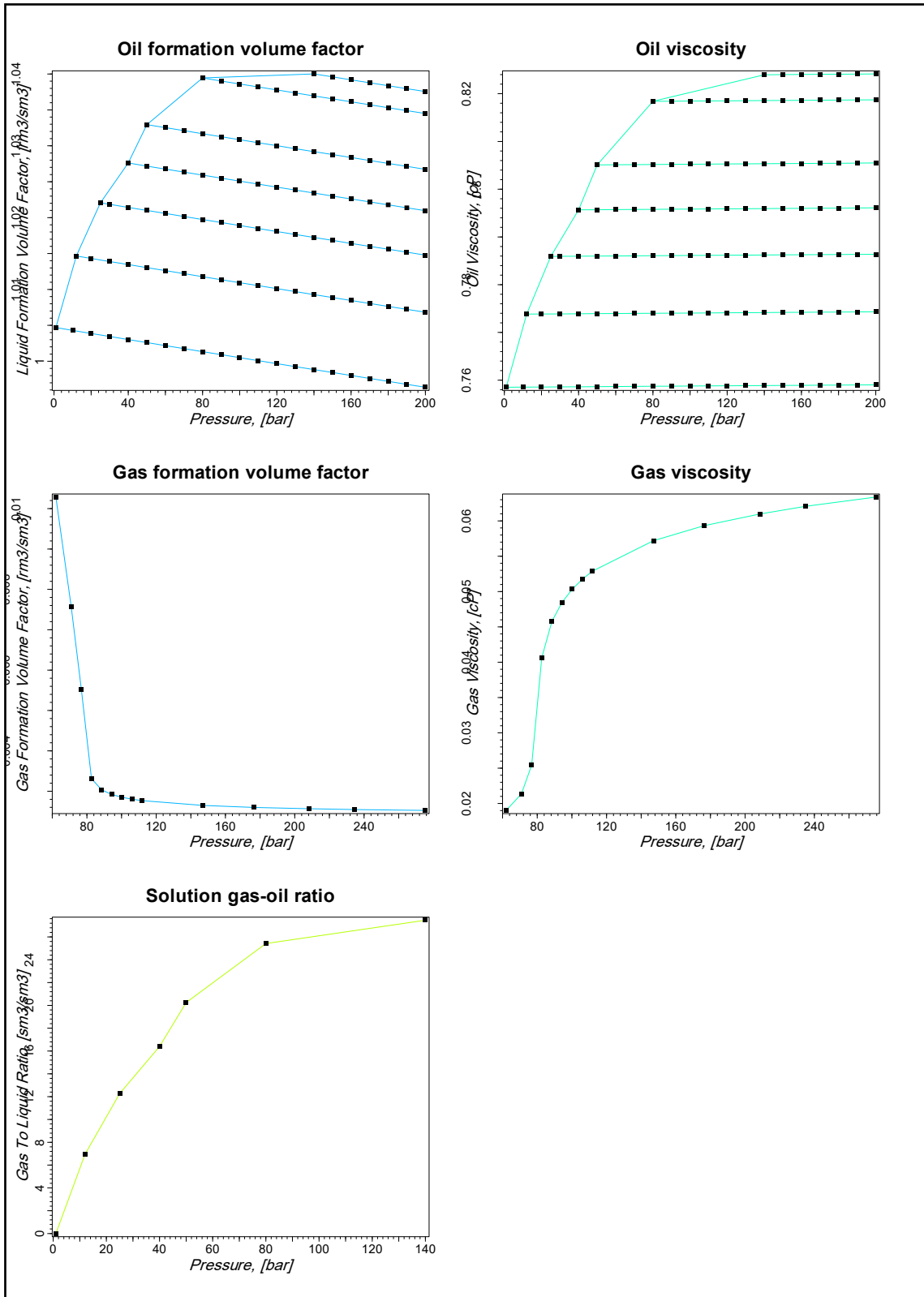
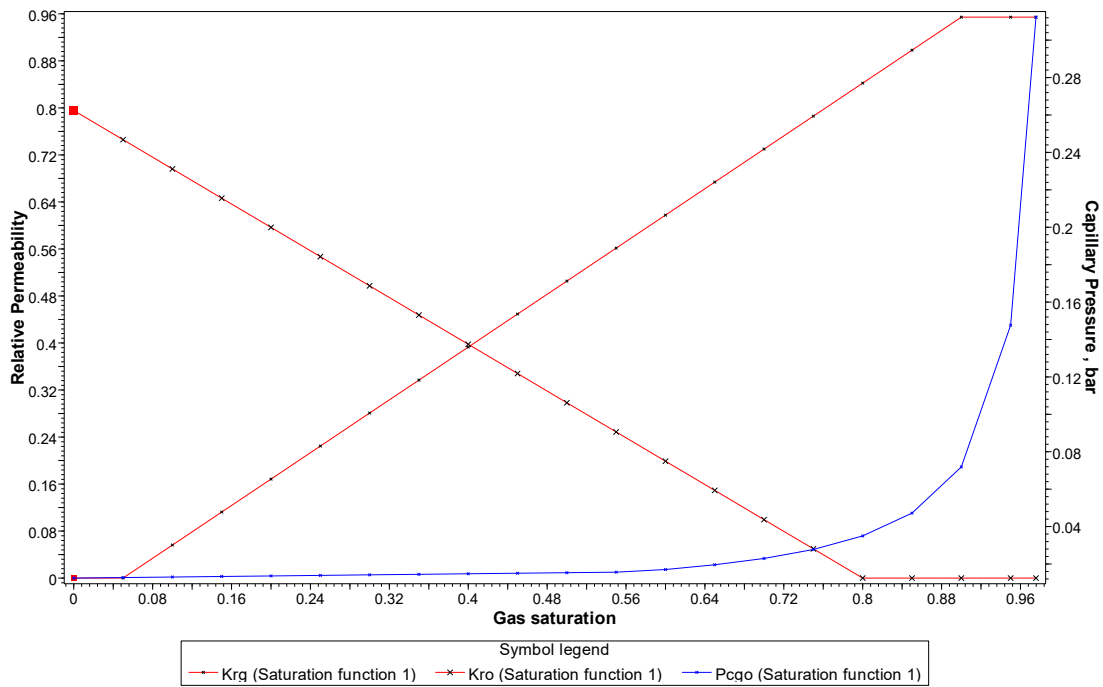


Figure 3.12: The PVT properties of Statoil’s model (exported from Petrel)

Starting CO<sub>2</sub> injection will generate at first a 2-phase system and subsequently interfacial tension that influences flow, saturation distribution, and fluid penetration in caprock. Consequently, relative permeability and capillary pressure in figure 3.14 must be utilized for 2-phase simulation.



**Figure 3.13: The Relative permeability and capillary pressure of Statoil's model (exported from Petrel)**

### 3.3.3 Numerical Simulation

The Statoil's dynamic model contains four virtual production wells in the south and one in the north to induce depletion owing to Troll field production. In 1999, wells began production until 2060, when three wells, WP1, WP2, and WP5, would be shut-in, and in 2122 that WP1 and WP2 would be shut-in. Moreover, pore volume multipliers exist in the south and north of the model to compensate for the unexplored reservoir area and match the pressure depletion inside the storage.

In the first step, the simulation data file was run by Eclipse 100 without considering pore volume multipliers. Since January 2022, CO<sub>2</sub> was injected for 25 years at a 5872000 sm<sup>3</sup>/day rate through well Alpha-N, and its post-injection migration was monitored until

2300. Figure 3.14 illustrates the CO<sub>2</sub> saturation distribution in 2300, migrated to the Beta zone through a saddle point in the middle of the field. On the other hand, the bottom hole pressure shows violence with 1000 bar in figure 3.15, besides field pressure.

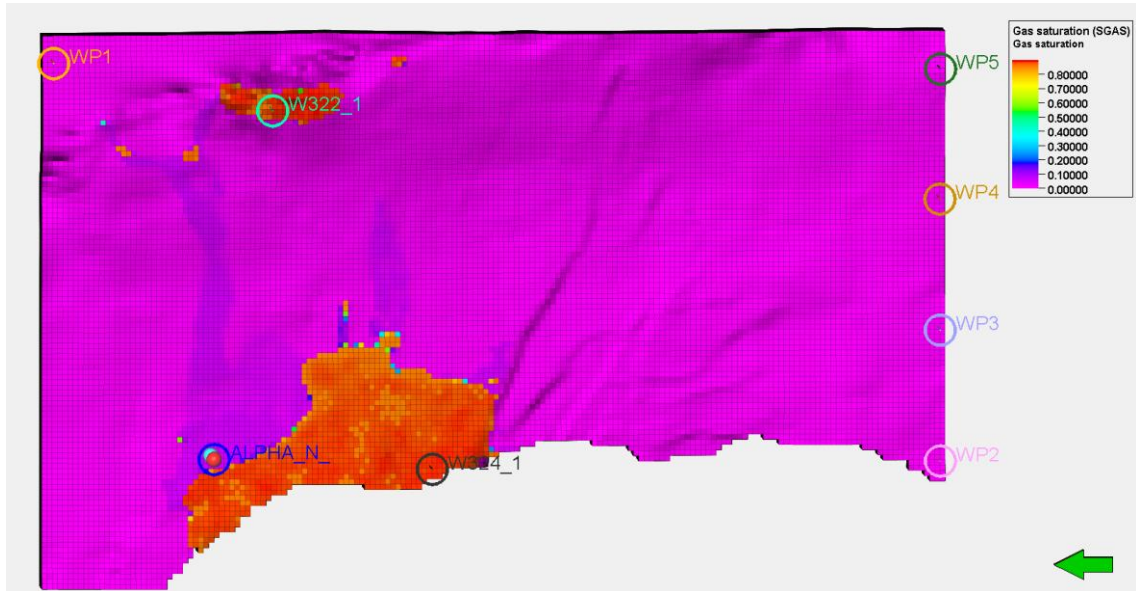


**Figure 3.14: Saturation distribution in 2300, after 25 years injection since 2022**

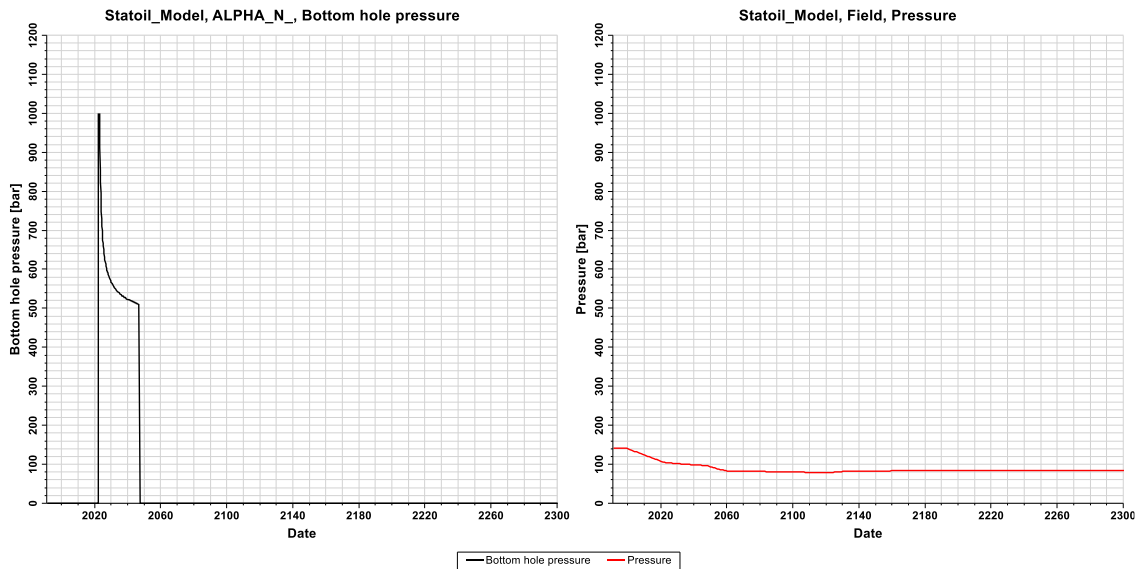


**Figure 3.15: Bottom hole and field pressure**

According to observations, the pressure depletion in the middle of the storage is predicted to be 14 bar between 1999 and 2022. Hence, the southern and northern pore volume multipliers are fixed at 50 and 55, respectively, by a manual history matching.

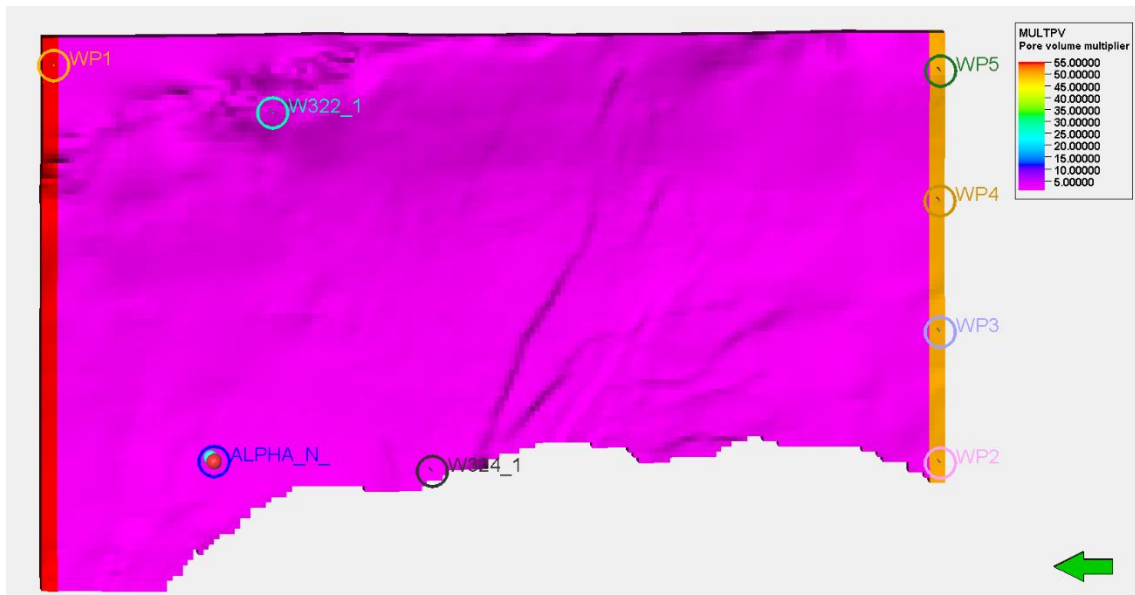


**Figure 3.16: Pore volume multiplier**

As mentioned before, the storage thins eastward as well as the caprock. Additionally, according to figure 3.17, there are a few minor faults and fractures at the top of the zone Beta, which is thinned. Therefore, the CO<sub>2</sub> plume must be prevented from reaching zone Beta as a leakage potential. Furthermore, the default injection well led to bottom hole pressure violence to 1000 bar, which is not feasible. The entire above items and caprock fracturing are parts of CO<sub>2</sub> storage risks, explained in section 2.1.4. In this regard, a new well design and injection optimization are required.

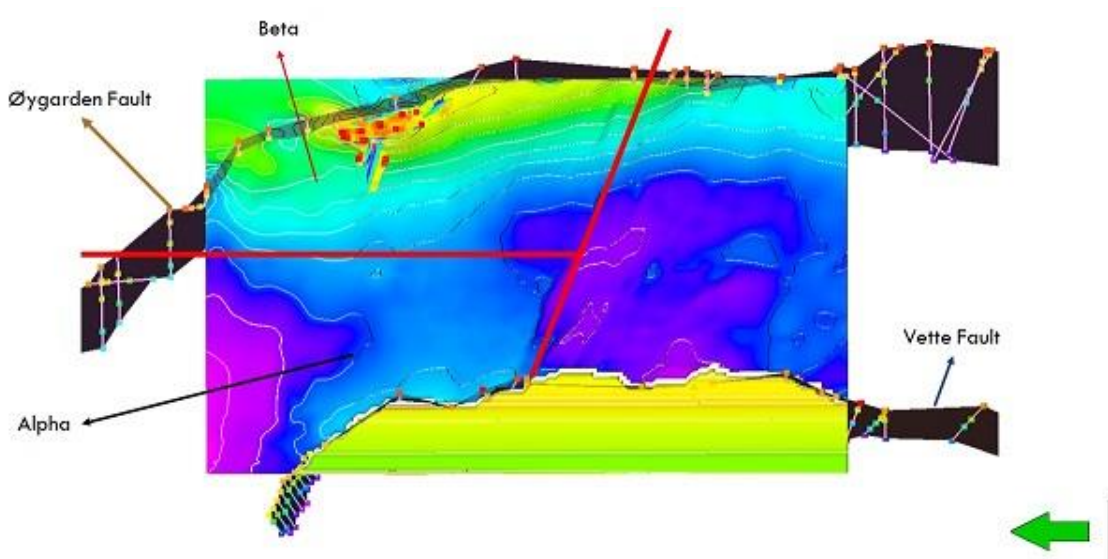


**Figure 3.17: Storage structure**

### 3.3.4 Well Design

Brobakken (2018) has analyzed the sensitivity of the field with respect to the well location in various locations; however, the employed model is different from Statoil's model regarding the presence of the virtual production wells. Indeed, the response of Statoil's model compared when the well is placed in the north of zone Alpha, near the zone Beta, and the south of the model and contributed to the CO<sub>2</sub> plume migration path in figure 3.18.

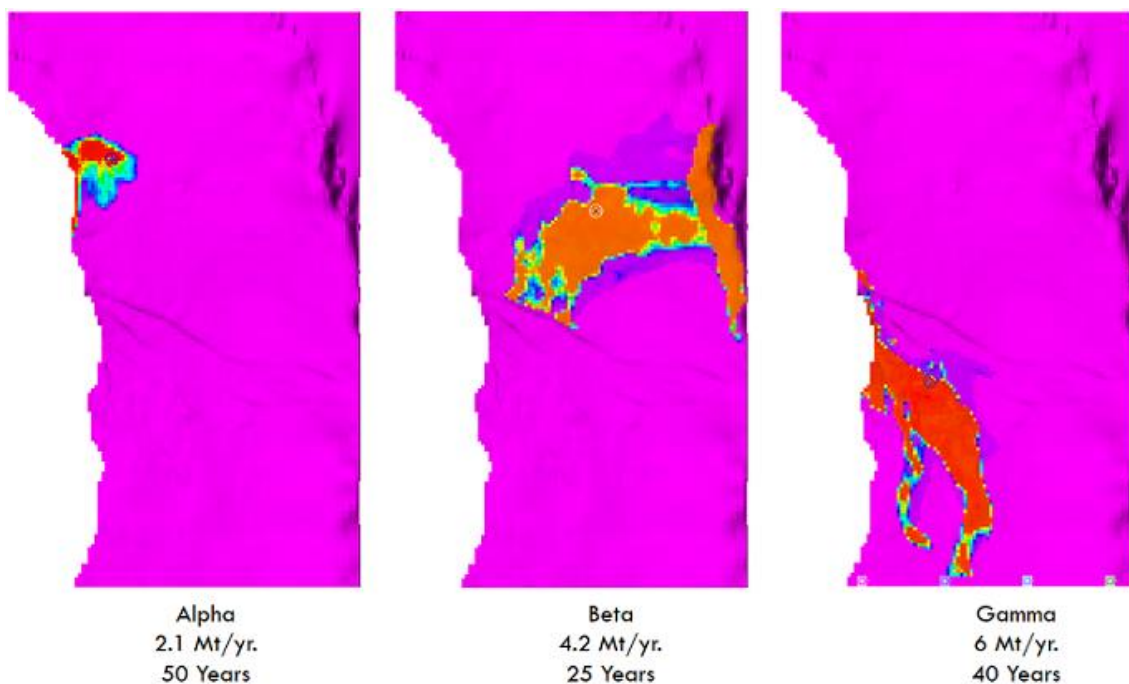


**Figure 3.18: Well location sensitivity analysis**

CO<sub>2</sub> injection in the zone Beta will certainly cause leakage. Despite the fact that zone Gamma possesses high storage potential, it cannot be used in this study because of the property uncertainty and the deviation of CO<sub>2</sub> plume from its natural path toward production wells, which are misleading. Zone Alpha is the best injection location, even though the well must be shifted upward and designed as a down-dip J-shaped directional well in the north of the zone with long displacement and perforation toward the northwest to prevent the bottom hole pressure from exceeding fracture pressure, and CO<sub>2</sub> from migrating in the direction of zone Beta. In consequence, the well Alpha was designed, and the top of the perforation was placed at 1600 m depth.

Based on the stress model in section 3.2.3, the minimum horizontal stress (Min SH) as the bottom hole pressure limit and fracture pressure as the field pressure constraint have been computed and plotted in figures 3.19 and 3.20.

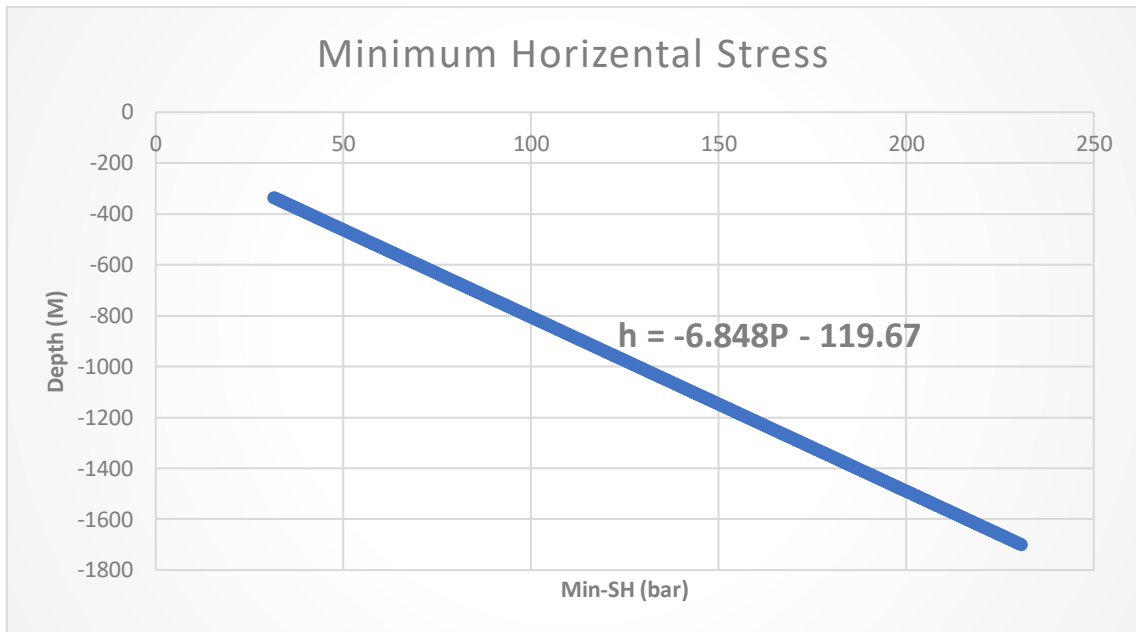


**Figure 3.19: Minimum horizontal stress**

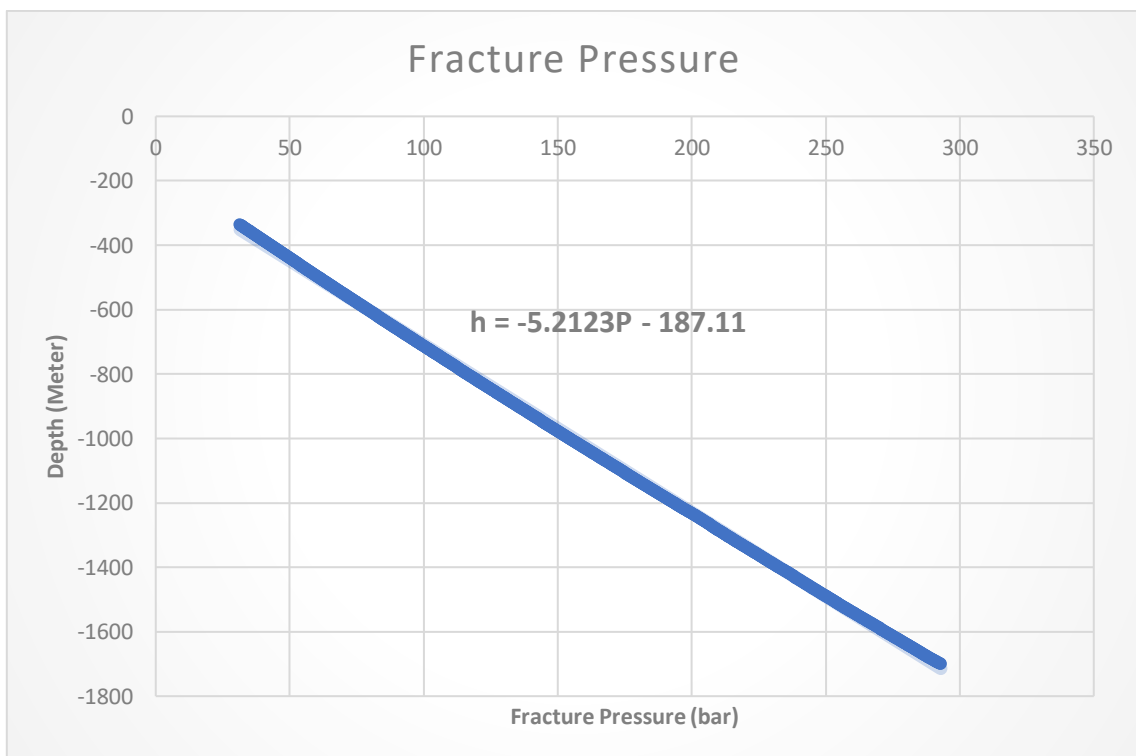


**Figure 3.20: Fracture pressure**

The Min SH in the depth of 1600 m is 216 bar; by considering a safety factor, 200 bar is fixed as the bottom hole fracture pressure. A simulation case for a 35-year CO<sub>2</sub> injection with a 5872000 sm<sup>3</sup>/day rate was created to confirm the well design, and the outcome 50 years after starting injection is demonstrated in figures 3.21 and 3.22.

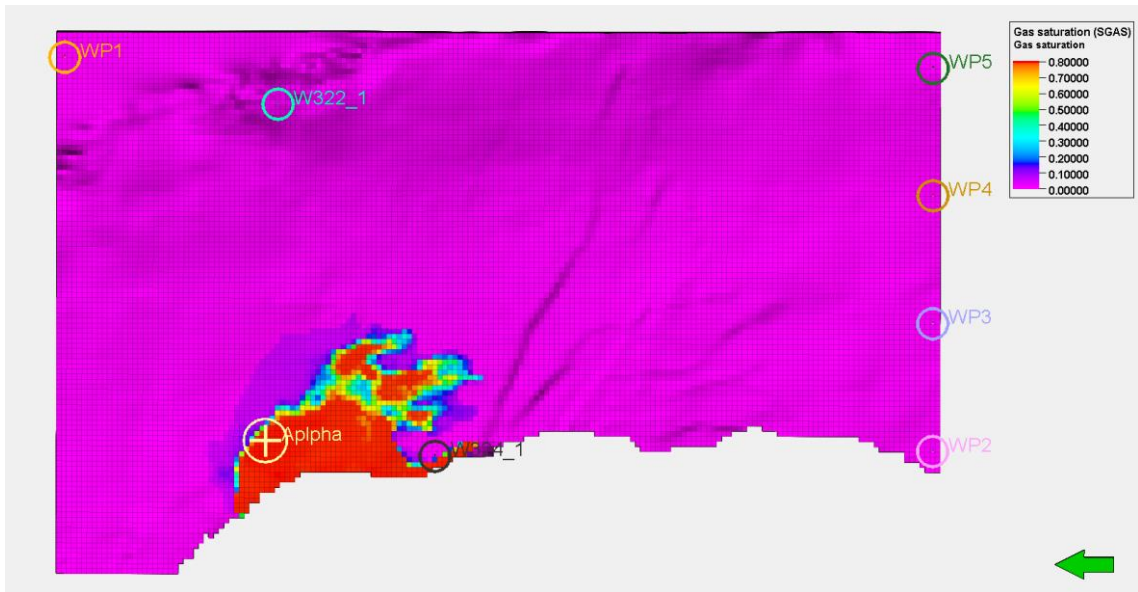


**Figure 3.21: Saturation distribution in 2072 after 35-year CO<sub>2</sub> injection by newly designed injection well**

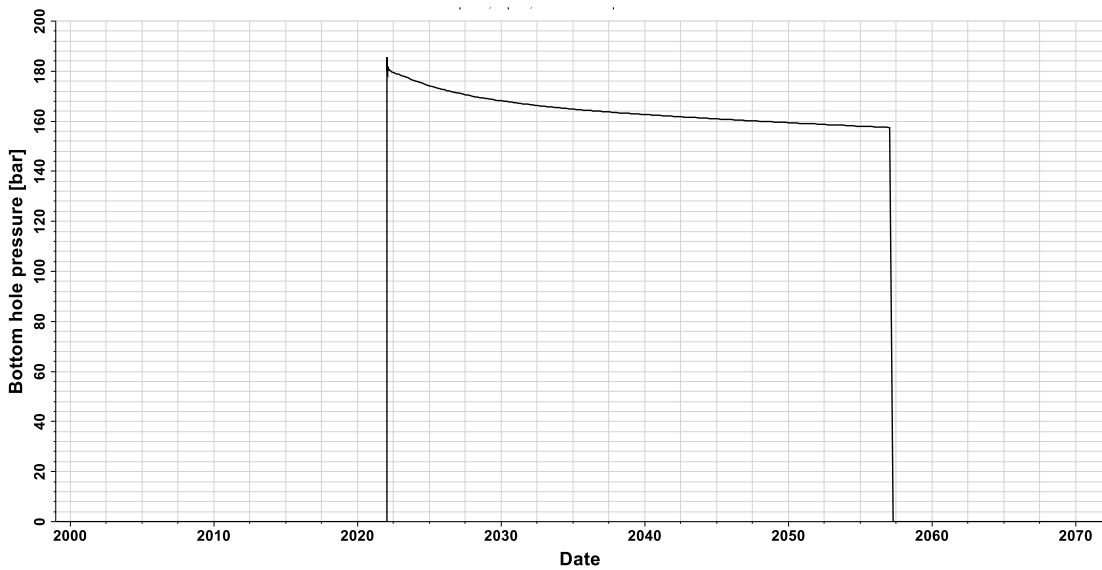


**Figure 3.22: Bottom hole pressure of well Alpha with 5872000 sm<sup>3</sup>/day injection rate**

### 3.4 Optimization Problem

Based on previous studies by (Cameron & Durlofsky, 2012) and (Santibanez-Borda, 2019), the other variables that should be set are injection rate and injection span. Moreover, similar to other engineering projects, the maximum benefits should be derived from CO<sub>2</sub> storage implementation costs related to exploration, study, development, drilling, and maintenance. Hence, to maximize the project's benefit, an optimization problem must be defined to find the optimum injection rate and injection span.

#### 3.4.1 Objective Formulation

According to the CO<sub>2</sub> storage goal and physics that is storing captured CO<sub>2</sub> in subsurface geological formations, the objective of the problem can be defined as follows:

- Maximizing the injected CO<sub>2</sub> while limiting field pressure at the top of the Injection region to avoid caprock fracturing and controlling the CO<sub>2</sub> leakage by preventing the CO<sub>2</sub> plume from migrating toward zone Beta.

Fracturing far from the injection well is unlikely due to the depletion impact of gas production in the Troll field. As the only alternative to fracturing, the shallowest part of zone Alpha is placed at 1240m depth, below the caprock that has a fracture pressure of 187 bar. The maximum allowable pressure at the top of zone Alpha will be 150 bar if a safety factor is employed.

While CO<sub>2</sub> injection from well Alpha, the first arriving spill point is located in a grid with an i-index of 60. Therefore, the i-index of 50 was chosen as the saturation constraint to prevent the CO<sub>2</sub> plume from reaching the 60<sup>th</sup> i-index.

As mentioned in section 2.1.6, the capillary diffusion through the caprock is a leakage concern. Based on the available reports and previous studies on the Smeaheia CO<sub>2</sub> storage, the Draupne formation as the primary caprock is considered seal, and no threshold pressure exists from the laboratory core analysis. On the other hand, figure 3.13 represents the capillary pressure of 0.2 bar optimistically. Owing to the very low average vertical permeability of Draupne formation (6 nano Darcy), the caprock appropriate thickness, and the presence of the secondary seal, the capillary diffusion can be assumed negligible.

The volume of injected CO<sub>2</sub> can be represented as the multiplication of injection rate and time which are optimization variables. Moreover, a grid-based SRM can predict saturation and pressure distribution quickly. These mean that the objective function and constraints can be written as below:

$$\text{Maximize } f(\text{Rate}, \text{Time}) = \text{Injected volume}$$

Subjected to:

$$g_1(\text{Rate}, \text{Time}) = \text{Saturation}_{i_1, j_1, k_1}(\text{Rate}, \text{Time}) - 0.1 \leq 0$$

$$g_2(\text{Rate}, \text{Time}) = \text{Pressure}_{k_2}(\text{Rate}, \text{Time}) - 150 \leq 0 \quad (3.1)$$

Where:

$$2 * 10^6 \text{ Sm}^3 / \text{day} \leq \text{Rate} \leq 7.6 * 10^6 \text{ Sm}^3 / \text{day}$$

$$25 \text{ years} \leq \text{Time} \leq 50 \text{ years}$$

$$i_1 = 50$$

$$0 \leq j_1 \leq 120$$

$$1 \leq k_1 \leq 2$$

$$k_2 = 1$$

### 3.4.2 Optimization Algorithm

The optimization algorithm in this study is GA, imported from the Pymoo package in Python, without any hyperparameter tuning. The constraint handling method is the death penalty, which is the default solution of the package.

## 3.5 Proxy Modeling

The machine learning algorithm selected for proxy modeling is ANN, especially with DNN structure in case of complex behavior of data. The model implementation will be done in Python because of the diversity and simplicity of data processing and machine learning packages. The Keras TensorFlow package will develop the ANN in the next chapter.

---

## 4 PROXY MODELING AND OPTIMIZATION, BUILDING THE STRUCTURE

In this chapter, two proxy models for saturation and pressure distribution will be built to satisfy the optimization objective and constraints. The process of creating the proxy model and performing optimization is based on the project workflow in figure 3.1 and is thoroughly explained in sections 2.2.1 and 2.3.2. In chapter 3, the Smeaheia storage and its model were investigated, and their constraints were defined. A new well was designed in the following, and the optimization objective was formulated. The next step will be carried out in this chapter by starting to generate SRM and, subsequently, the optimization foundation.

### 4.1 Developing SRMs

Generally, there are three types of SRMs: field-based, well-based, and Grid-based. Depending on the SRM application, one SRM or a coupled SRM can be chosen. Because the project requires controlling saturation and pressure at various points and depths during optimization, a grid-based SRM (SRM<sub>G</sub>) will be built.

#### 4.1.1 Data Generation

An ANN needs strong and diverse input data to learn the previous performance of a phenomenon and predict its output in various conditions. In case of no existing or lack of real data, analytical or numerical models are able to generate synthetic data. As the Smeaheia project has not begun yet, and there is not any data about the storage performance, Numerical simulation will be employed to generate data by Petrel software. The optimization variables are injection rate and injection time; in consequence, it is required to create a number of simulation cases (training examples) with different injection rates to simulate the model's behavior respect to the injection rate variation in specific time steps and introduce them to the ANN for training.

Amini (2015) generated SRM<sub>G</sub> with three simulation cases with the same injection interval and increased it to five instances to improve SRM accuracy in the edge of the CO<sub>2</sub> plume. As shown in the project workflow (figure 3.1), the number of numerical simulation cases is one of the hyperparameters that should be tuned while ANN training

to generalize output in prediction. Developing the proxy commenced with introducing the result of three simulation cases that were risen to seven instances until the acceptance of the model accuracy.

Owing to better proxy models' performance in interpolation than extrapolation, the injection rate range of numerical simulations should overlap the minimum and maximum usable rate. According to figure 3.19, the maximum possible rate, without exceeding bottom hole fracture pressure, is 5.5 Mt. Therefore, seven rates between 1.3Mt and 5.5 Mt will be chosen, as shown in figures 4.1 and 4.2.

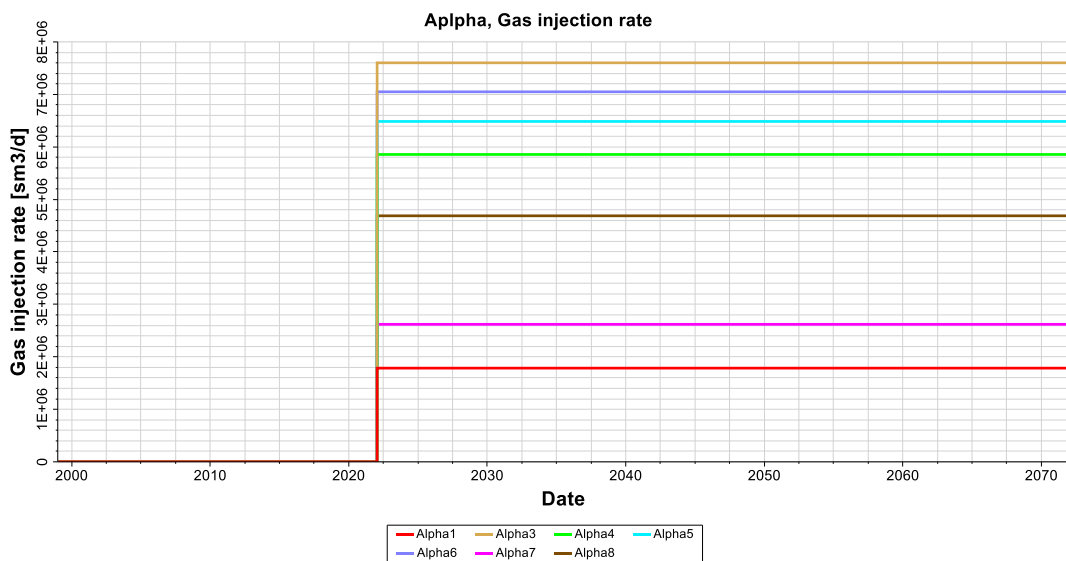


**Figure 4.1: Injection rate of numerical simulation cases**

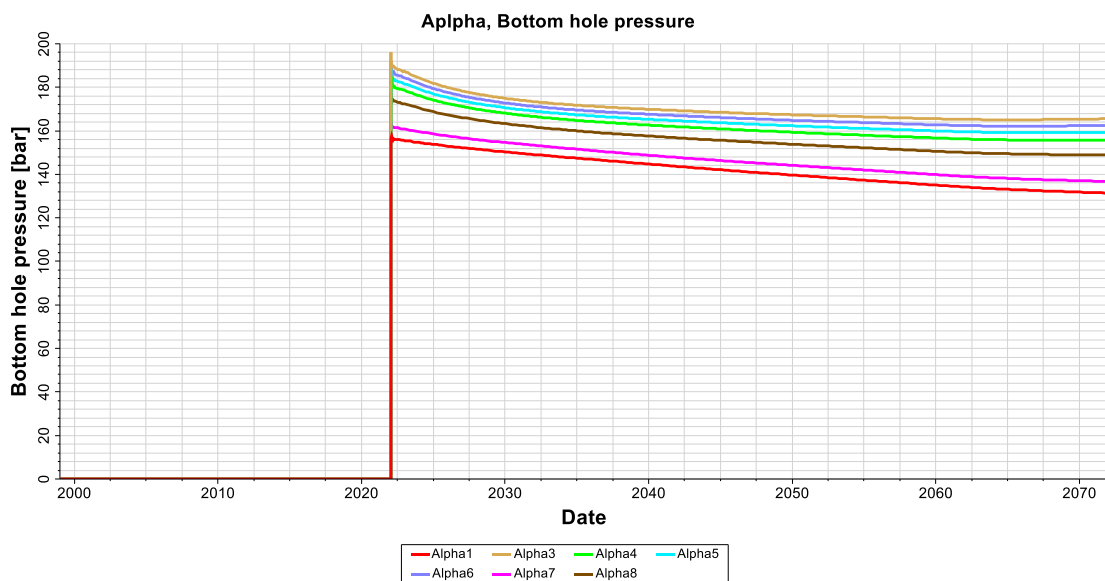


**Figure 4.2: Bottom hole pressure of numerical simulation cases**

The SRM's time step must be fixed to export the simulation result because both have the same time step. The best time step is one month to chase any minor change in property distribution; although, the SRM is intended to simulate 50 years of CO<sub>2</sub> storage, and a too-short time step will cause difficulty in data handling due to heavy data. While developing proxy, an assortment of time steps from 1 month to 5 years was examined. Finally, a 6-month time step was selected, balancing accuracy and data volume. The data was exported from petrel as Gslib properties with ASCII format, compliant with Python standards.

#### 4.1.2 Input Features

As explained in section 2.2.2, two different methodologies exist for building SRM<sub>G</sub>: cascading and non-cascading. This project began with cascading SRM, then modified to non-cascading, resulting from error accumulation, complexity, and time-consuming step-by-step prediction. Therefore, table 2.3, reservoir physic, optimization objective, and SRM's type and methodology employed to select input features in order for dataset generation. Table 4.1 summarizes 31 input features for training SRM's ANN.

**Table 4.1: Input Features**

Cell Index (i, j, k)
Cell Coordinate (X, Y, Z)
Horizontal and Vertical Permeability
Porosity
Distance to injection well and production wells
Injection Rate
Saturation at 0 <sup>th</sup> time step
Pressure at 0 <sup>th</sup> time step
Tier Model at 0 <sup>th</sup> time step
Time step

The properties and conditions of surrounding cells around a grid block must be taken into account as the boundary condition in reservoir simulation because it influences fluid migration. While CO<sub>2</sub> injection and storage, the CO<sub>2</sub> migrates upward by gravity forces and alters the CO<sub>2</sub> content and saturation of grids depending on the upper and lower layer. Thus, a tier model will be created in this study in the shape of figure 4.3 to calculate the average pressure, saturation, permeability, and porosity of surrounding grids in the current layer, above layer, and below layer that construct tier-1, tier-2, and tier-3.

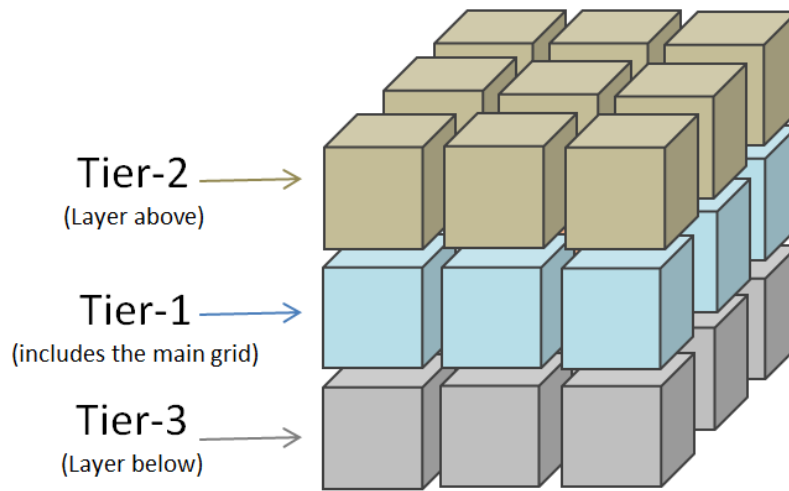


**Figure 4.3: Tier model (Amini, 2015)**

Except for permeability, which uses a harmonic averaging method like equation 4.1, the average of all parameters is computed by the arithmetic method.

$$k_{ave} = \frac{\sum_{j=1}^n Z_j}{\sum_{j=1}^n \frac{Z_j}{k_j}} \quad (3.1)$$

In this study, the boundaries are isolated, making the permeability and porosity of the layer above the first layer and below the last layer zero; indeed, the CO<sub>2</sub> saturation will be zero in the mentioned layers. Furthermore, when the boundary is closed, the reservoir condition will be pseudo-steady state condition, and the pressure above the first layer and below the last layer will equal the concerning layer, and saturation will be zero.

The other input which requires calculation and pre-processing is the distance of grids to injection and production wells. In this regard, the perforation length is considered a line, and the distance of the grids' central point coordinate to the line will be computed by the projection of the point coordinate on the line plane and calculating the minimum distance of the projected point and line. The below solution was implemented in Python to compute the distance of five production wells and one injection well, picking the first and last point of the perforation line (P1 and P2).

```

Def point_to_line(point, P1, P2):
    a = P1-P2
    b = point-P2
    distance = np.linalg.norm(np.cross(a,b)) / np.linalg.norm(a)
    return distance

```

#### 4.1.3 Sampling Dataset

The reservoir model contains 1510500 grid blocks that will require colossal memory and a long training time if the entire grids are included in the input dataset. Therefore, the input grids will be reduced by various sampling methods and criteria based on the output property of the model.

The input dataset of the saturation model will be sampled based on the parameter alteration that selects more affected cells by CO<sub>2</sub> injection. Injection with the highest possible rate influence more cells and propagate CO<sub>2</sub> in a larger space. Indeed, the grids with non-zero saturation at the end of 50 years injection with maximum rate were sampled for the input of the saturation model, and other cells were eliminated for each numerical simulation case.

However, this sampling method led to overfitting for the input of the pressure model due to its distribution in the entire storage, not only a region around the injection well. The trained model by parameter change sampled input could not generalize in the blind evaluation and was rejected. Therefore, the grids were sampled randomly for training the pressure model. In this order, 1485000 cells will be selected randomly and deleted from all cases.

The final dataset comprises 31 features with different ranges of real numbers that may lead to instability in training. According to the physic of the problem, Relu and Sigmoid have been selected as the activation function with an output between 0 and 1. Therefore,

the dataset requires normalization by the min-max method (equation 3.2) to put all input characteristics, except saturation, in the range of 0 and 1. The minimum and maximum of each property are global, and no existing less or more than them. Furthermore, the final prediction of the pressure model can be denormalized to be comparable with its actual unit.

$$x_{norm} = \frac{x - x_{min}}{x_{max} - x_{min}} \quad (3.2)$$

#### 4.1.4 ANN Structure

The last step is building the structure of an ANN, which provides sufficient accuracy in validation, test, and blind evaluation. In this aim, hyperparameters, including the number of layers, the number of units, activation function, and learning rate, in addition to feature and amount of data, must be tuned. Formerly, characteristics and examples numbers were fixed regarding the reciprocity of accuracy and computer facilities tolerance. The best hyperparameters related to the ANN structure were obtained by several trials and checking the error in the blind evaluation. In spite of the fact that Amini was employed and advised one hidden layer for SRM training, raising the hidden layers enhanced the model performance tremendously. The blow scripts show the DNN structures of the pressure and saturation model.

```

Def Pressure_Model (Inputs_P) :
    first_dense_p = Dense(512 ,activation='relu',
    name='hidden1_relu') (Inputs_P)
    second_dense_p = Dense(512, activation='relu',
    name='hidden2_relu') (first_dense_p)
    third_dense_p = Dense(128, activation= 'relu',
    name='hidden3_relu') (second_dense_p)
    Pressure = Dense(units=1, activation='sigmoid',
    name='Pressure_sigmoid') (third_dense_p)
    P_model50 = Model(inputs=Inputs_P, outputs=Pressure)
    return P_model50

```

```

def Saturation_Model (Inputs_Sat) :
    first_dense_sat = Dense(units=512, activation='relu',
    name='hidden1_relu') (Inputs_Sat)
    second_dense_sat = Dense(512, activation='relu',
    name='hidden2_relu') (first_dense_sat)

```

```

third_dense_sat = Dense(128, activation= 'relu',
name='hidden3_relu')(second_dense_sat)

fourth_dense_sat = Dense(128, activation= 'relu',
name='hidden4_relu')(third_dense_sat)

fifth_dense_sat = Dense(128, activation= 'relu',
name='hidden5_relu')(fourth_dense_sat)

Saturation = Dense(units=1,activation= 'sigmoid',
name='Saturation_sigmoid')(fifth_dense_sat)

sat_model50 = Model(inputs=Inputs_Sat, outputs=Saturation)

return sat_model50

```

Many optimization algorithms minimize the loss function output while training an ANN. SGD, RMSprop, Adam, Adadelta, Adamax, and Nadam are a group of available optimizers. In this study, Adam (Kingma & Ba, 2014) indicated better performance than others. Besides, an exponential learning rate decay function was utilized to make the learning rate stable and avoid any fluctuation in the learning and validation loss trend.

```

Def Pressure_optimizer():

lr_schedule_P = tf.keras.optimizers.schedules.ExponentialDecay(
initial_learning_rate=0.0005, decay_steps=10000, decay_rate=0.9)

adam_P = tf.keras.optimizers.Adam(learning_rate = lr_schedule_P,
beta_1=0.9, beta_2=0.999, epsilon=1e-07)

return adam_P

```

```

def Sat_optimizer():

lr_schedule_sat =
tf.keras.optimizers.schedules.ExponentialDecay(initial_learning_
rate=0.0005, decay_steps=100000, decay_rate=0.9)

adam_sat = tf.keras.optimizers.Adam(learning_rate =
lr_schedule_sat, beta_1=0.9, beta_2=0.999, epsilon=1e-07)

return adam_sat

```

Finally, the below script was used to save the trained model and its history after training the models by fit API. Due to high data volume, the mini-batch helped reduce training time by performing backpropagation for a group of samples equal to the batch size rather than every single example. This point should be emphasized that the mini-batch method

will cause fluctuation of loss function plot typically, which is different from the variations due to overfitting and instability.

```

History_p_main_path = 'D:\Master o
science\Thesis\Export\pressure_history50'
model_p_main_path = 'D:\Master o science\
Thesis\Export\pressure_model50'
history_P50 = P_model50.fit(Xp_train, Pressure_train,
                           batch_size=1024, epochs=50,
                           validation_data=(Xp_val, Pressure_val))
history_p_file = 'P_history50.npy'
model_p_file = 'P_model50'
history_p_path = joined_path = os.path.join(history_p_main_path,
history_p_file)
model_p_path = joined_path = os.path.join(model_p_main_path,
model_p_file)
np.save(history_p_path, history_P50.history)
P_model50.save(model_p_path)

```

```

history_sat_main_path = 'D:\Master o
science\Thesis\Export\Sat_history50'
model_sat_main_path = 'D:\Master o
science\Thesis\Export\Sat_model50'

history_sat50 = sat_model50.fit(X_train, Sat_train,
                               batch_size=1024, epochs=150,
                               validation_data=(X_val, Sat_val))

history_sat_file = 'sat_history50.npy'
model_sat_file = 'Sat_model50'
history_sat_path = joined_path = os.path.join(history_sat_main_path,
history_sat_file)
model_sat_path = joined_path = os.path.join(model_sat_main_path,
model_sat_file)
np.save(history_sat_path, history_sat50.history)
sat_model50.save(model_sat_path)

```

## 4.2 Optimization

The optimization objective, described in section 3.4.1, must be restructured by adapting the problem variables to the model inputs. The rate variable has been exactly taken into account in the model. In contrast, the time has been introduced to the model in 6-month

time steps, and the injected volume equals the multiplication of rate and time, and each time step is 162.5 days. On the other hand, the function of GA in Pymoo is based on minimizing the objective. Consequently, the time will be replaced with 182.5 times by time step and the negative optimization objective will be minimized as below:

$$\text{Minimize } f(\text{Rate}, \text{Time}) = -182.5 \times \text{Rate} \times \text{Time Step}$$

Subjected to:

$$g_1(\text{Rate}, \text{Time Step}) = \text{Saturation}_{i_1, j_1, k_1}(\text{Rate}, \text{Time Step}) - 0.1 \leq 0$$

$$g_2(\text{Rate}, \text{Time Step}) = \text{Pressure}_{k_2}(\text{Rate}, \text{Time Step}) - 150 \leq 0 \quad (4.3)$$

Where:

$$2 * 10^6 \text{ Sm}^3 / \text{day} \leq \text{Rate} \leq 7.6 * 10^6 \text{ Sm}^3 / \text{day}$$

$$50 \leq \text{Time Step} \leq 100$$

$$i_1 = 50$$

$$0 \leq j_1 \leq 120$$

$$1 \leq k_1 \leq 2$$

$$k_2 = 1$$

#### 4.2.1 Optimization Implementation

The objective function can be written word to word by the variables to create the problem in Python. Nevertheless, constraints require two functions to compute the pressure and saturation in the desired grids by the pressure and saturation SRM. Now, the objective and problem can be written as below script by the functional problem, which has a default constraint feasibility check. In case of requiring another constraint handling method, it must be imported from the package and introduced to the problem or built by a separate function.

```

from pymoo.problems.functional import FunctionalProblem

def func_obj(x):
    return -182.5*(x[0] * x[1] )

constr_ieq = [
    lambda x: np.amax(sat_prediction(x[0],x[1]))-0.1,
    lambda x: np.amax(Pressure_prediction(x[0],x[1]))-150
]

```

```
problem = FunctionalProblem(2,
                             func_obj,
                             xl=np.array([2e6, 50]),
                             xu=np.array([7.6e6, 100]),
                             constr_ieq=constr_ieq)
```

The following script selects the GA as the optimization algorithm and defines the sampling, crossover, and mutation methods. Moreover, the time step must be an integer number, and picking an integer amount for the rate according to its range makes the optimization faster.

```
from pymoo.factory import get_algorithm, get_crossover,
get_mutation, get_sampling
from pymoo.optimize import minimize

method = get_algorithm("ga",
                      pop_size=100,
                      sampling=get_sampling("int_random"),
                      crossover=get_crossover("int_sbx", prob=1.0,
                      eta=3.0),
                      mutation=get_mutation("int_pm", prob=1.0,
                      eta=3.0),
                      eliminate_duplicates=True,
                      )
```

Finally, the optimizer computes the cost function of an initial population with 100 individuals and minimizes them by substituting 100 generations. The optimum result corresponds to the individual with minimum objective in the final population.

```
res = minimize(problem,
               method,
               termination=('n_gen', 100),
               seed=1,
               save_history=True,
               verbose=True
               )
```

## 5 PROXY MODEL AND OPTIMIZATION PROGRESS, RESULT, AND VALIDATION

In this chapter, the proxy modeling progress and results will be represented, and a blind simulation case will validate the final model. Subsequently, the optimization problem will be solved, and the constraints will be confirmed by performing a numerical simulation in both injection and post-injection interval.

### 5.1 Developing Proxy Model

In a non-cascading SRM<sub>G</sub>, besides static input, the dynamic features, including pressure, saturation, and their tier model, are in the initial condition, zero time-step. The output of each model is the CO<sub>2</sub> saturation or pressure of grids at all time steps during the injection. As this study is composed of 100 time-steps with 6-month intervals, each grid will have 100 outputs per simulation case. In fact, in a simulation case data, only the time step will change according to the output, and by altering the simulation case, the injection rate will change in a constant time step. Moreover, sampling declines the grids of each case to 25000 more or less; considering seven simulation cases and 100 time-steps, the final dataset contains 17500000 examples.

Developing an ANN involves the training, validation, and testing phase that requires a separate dataset. Consequently, the generated dataset must be split into three datasets for three stages. Frequently, the training, validation, and testing dataset ratios are 80%, 10%, and 10% of the entire data. While fitting the model, the model is trained by the training dataset, and after each epoch, the resulted model will be validated by the validation dataset. By finishing model training, the final model will be tested with the testing dataset. An appropriate model possesses the same loss and metrics in all steps approximately. MSE, equation 5.1 computes the loss function, and the metrics equal MAE, equation 5.2.

$$MSE = \frac{1}{n} \sum_{i=1}^n \left( Y_{i_{true}} - Y_{i_{prediction}} \right)^2 \quad (5.1)$$

$$MAE = \frac{1}{n} \sum_{i=1}^n \left| Y_{i_{true}} - Y_{i_{prediction}} \right| \quad (5.2)$$

### 5.1.1 Model Training

The CO<sub>2</sub> saturation model error does not change significantly after 150 epochs; that is the evidence of approximate achieving the minimum loss. Figures 5.1 and 5.2 indicate loss function and MAE trend during training and validation. Due to employing the mini-batch method for fitting the model, some fluctuations can be observed in the diagrams, which are hidden by nearing the optimum model. Testing confirms the model by resulting in roughly similar and low errors of all model development steps, compared in figure 5.3.

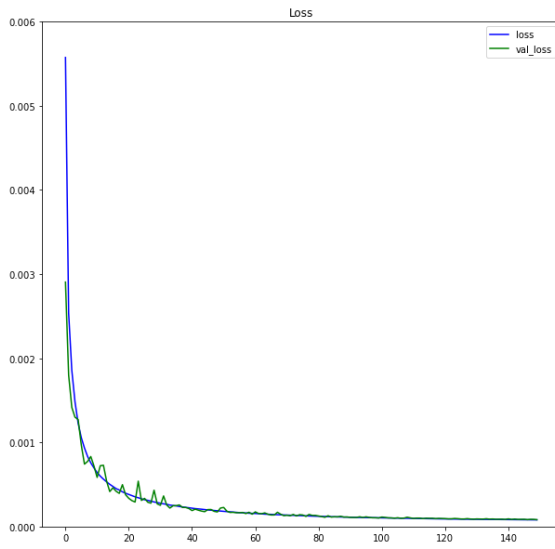


Figure 5.1: Saturation model loss

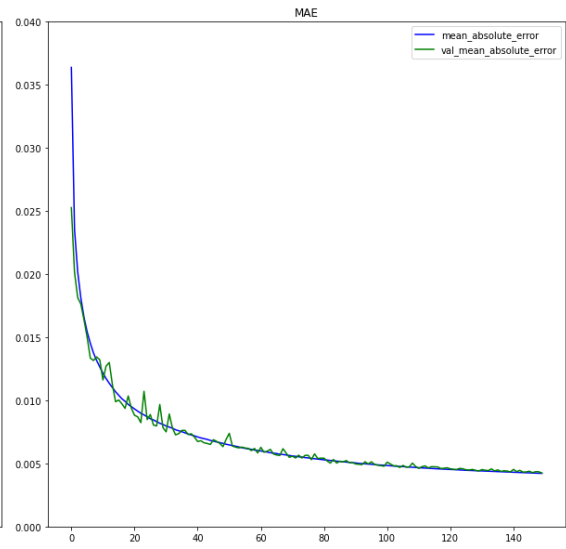


Figure 5.2: Saturation model MAE

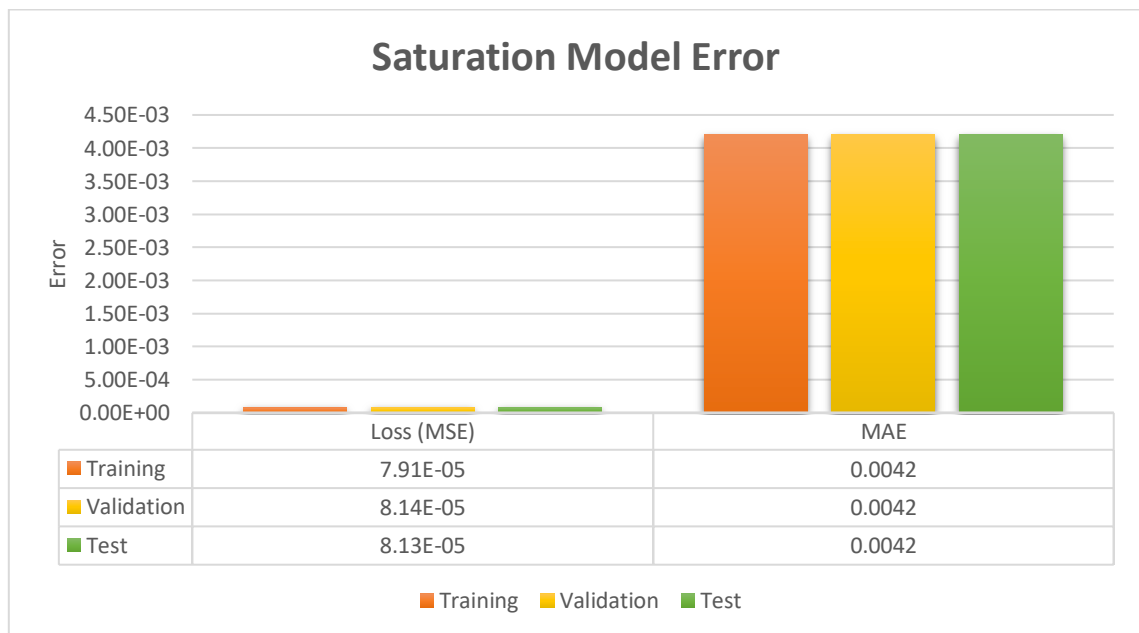


Figure 5.3: Saturation model evaluation

In contrast with the saturation model, the pressure network approached the minimum loss quickly, only after 50 epochs, and reflected less disruption in the declining trend of errors. The model errors in all stages are meaningfully comparable, and the model can be verified in the preliminary evaluation. Figures 5.4 and 5.5 represents loss function and MAE while model training and validation.

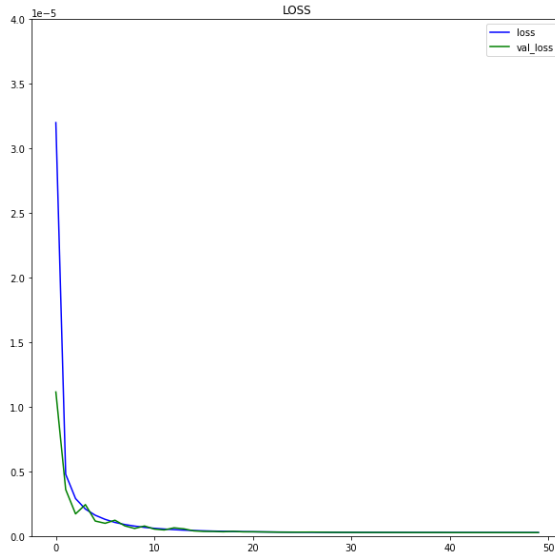


Figure 5.4: Pressure model loss

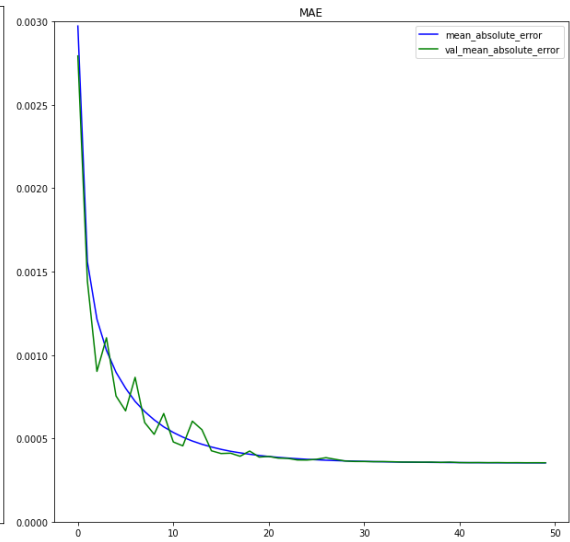


Figure 5.5: Pressure model MAE

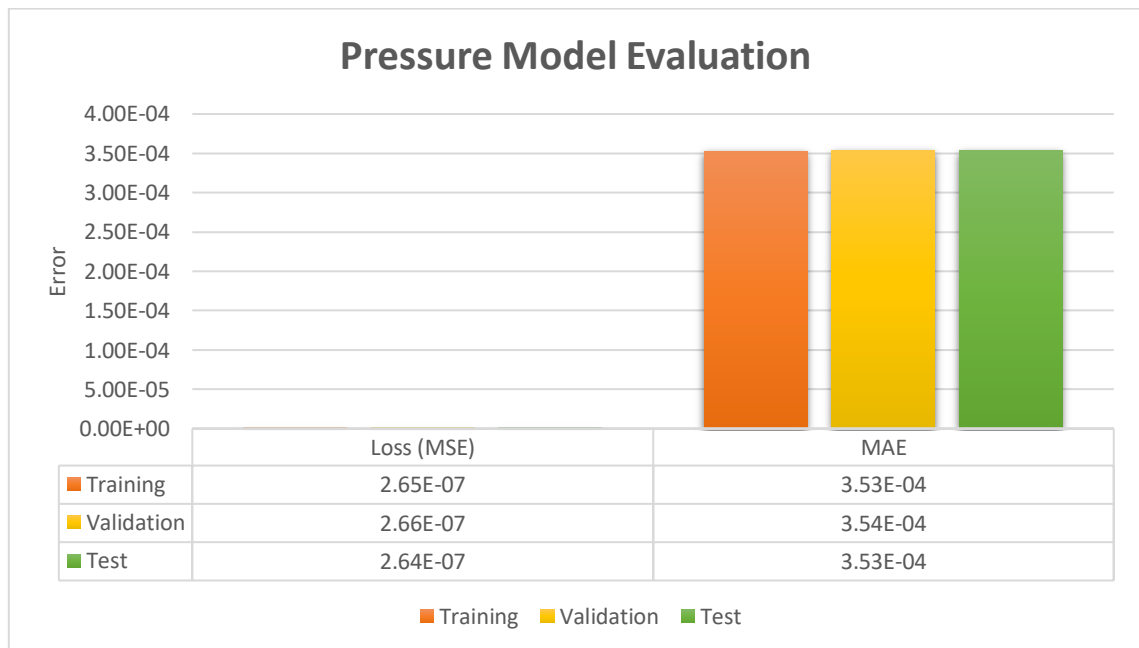


Figure 5.6: Pressure Model Evaluation

As the pressure data is normalized, the MAE of the pressure is different from the real MAE in the bar unit. The normalization function (equation 4.1) can be transformed into the denormalization function by keeping the real value of the parameter on one side and transferring the other variables to the other side, which leads to equation 5.3.

$$x = x_{norm}(x_{max} - x_{min}) + x_{min} \quad (5.3)$$

By replacing the denormalized parameter inside the MAE formula (equation 5.2), the  $Y_{min}$  will be removed from the equation, and equation 5.4 will be obtained for the real MAE. The real MAE of the pressure model was calculated by the minimum and maximum pressure and plotted in figure 5.7.

$$Real\ MAE = (Y_{max} - Y_{min}) \frac{1}{n} \sum_{i=1}^n |Y_{i_{true-norm}} - Y_{i_{prediction-norm}}| \quad (5.4)$$

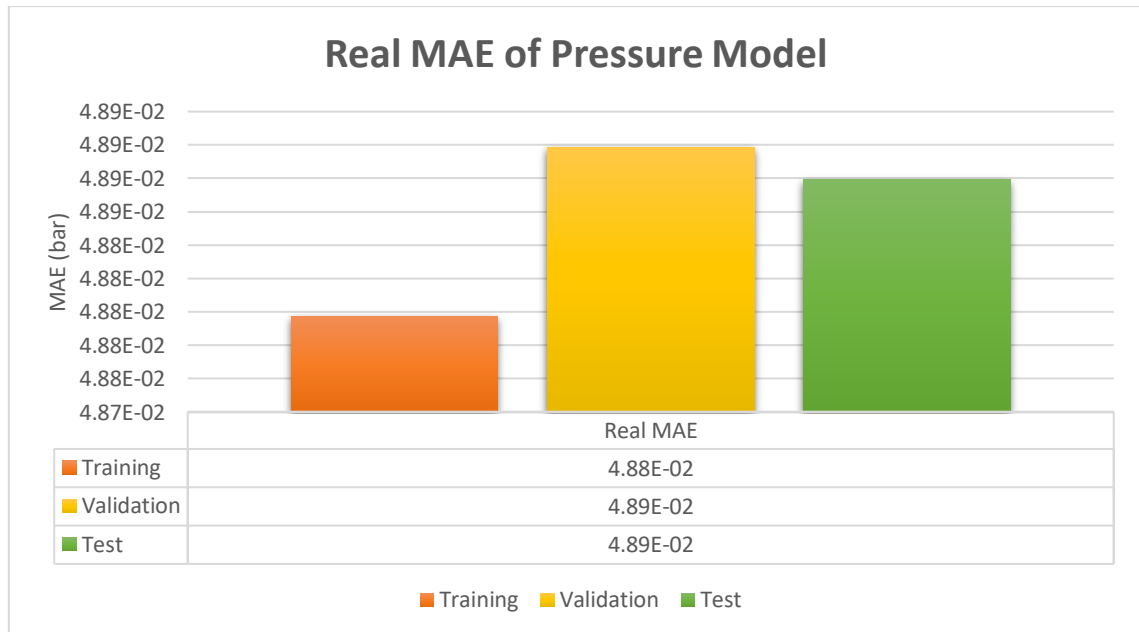


**Figure 5.7: Real MAE of the pressure model**

### 5.1.2 Blind Evaluation

Ultimately, the SRMs will be validated by a blind case that was never introduced to the model. In this order, a numerical simulation case with a rate different from other cases will be created and test the model feasibility for the proxy model applications such as

optimization and sensitivity analysis. Figure 5.8 displays the MAE of the CO<sub>2</sub> saturation SRM. A growth of error is visible in the diagram by increasing the time steps that differ from error accumulation in a cascading model. The main reason is concerning the physics of CO<sub>2</sub> propagation in the storage by passing the time and increasing the number of cells with non-zero saturation because the model operates better in distinguishing between grids zero and non-zero saturation than predicting the CO<sub>2</sub> saturation in grids with existing CO<sub>2</sub>. Hence, the number of cells with zero error decreases, and MAE increases.

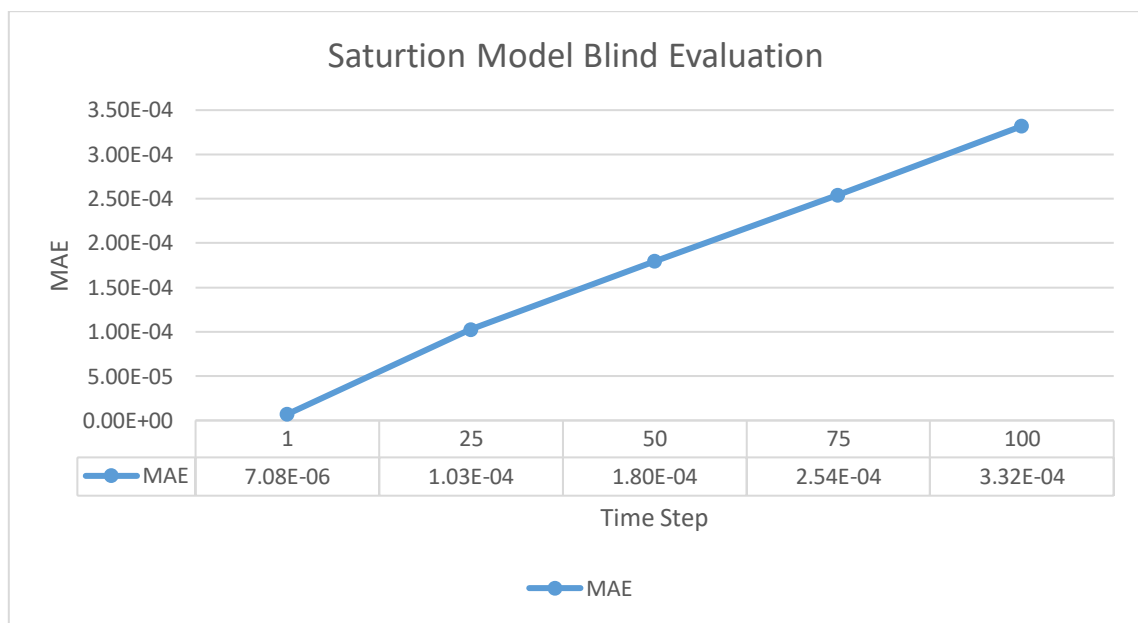


**Figure 5.8: Saturation model blind evaluation**

In regard to the pressure model, the SRM predicted the blind case and the real MAE by denormalization of predicted pressure, computed with respect to the petrel simulation result in various time steps. Unlike the CO<sub>2</sub> saturation, the pressure is distributed among all grids, and the error will not escalate with time. The model's error is demonstrated in the bar unit in figure 5.9.

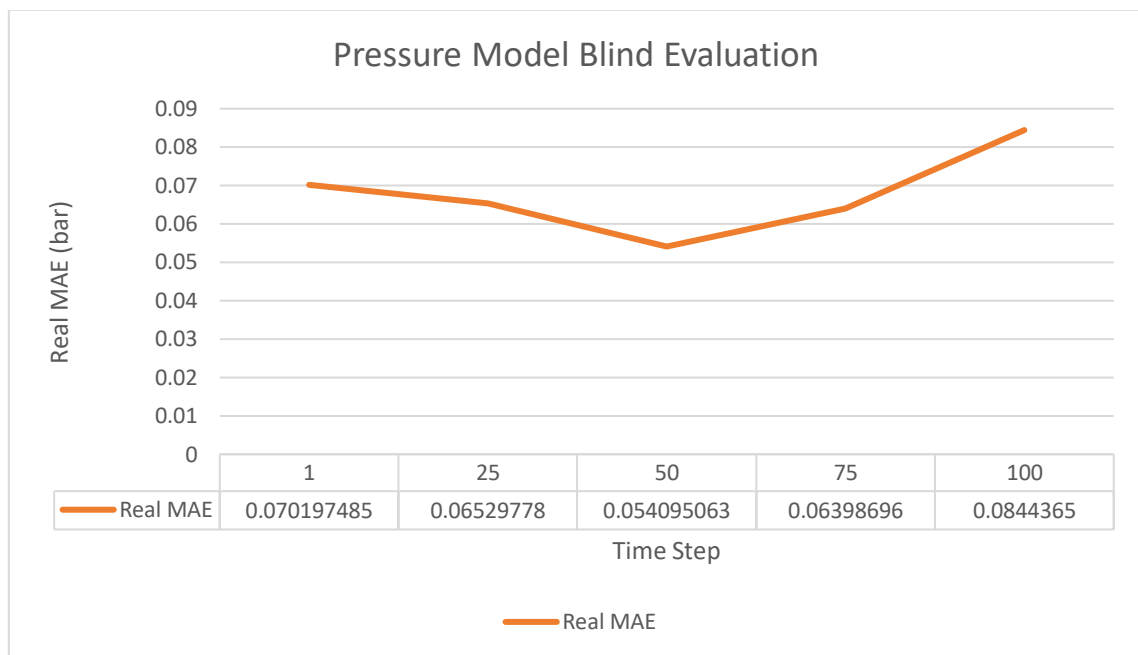


**Figure 5.9: Pressure model blind evaluation**

## 5.2 Proxy Model Results

In this section, the developed SRMs will predict CO<sub>2</sub> saturation and pressure distribution in reservoir grids with both training and blind evaluation cases. The output maps will be compared with the numerical simulation results in petrel to expose the proxy models' accuracy better.

### 5.2.1 SRM Result

25 years injection with the rate of  $1798810 \text{ Sm}^3/\text{day}$ , 30<sup>th</sup> layer:

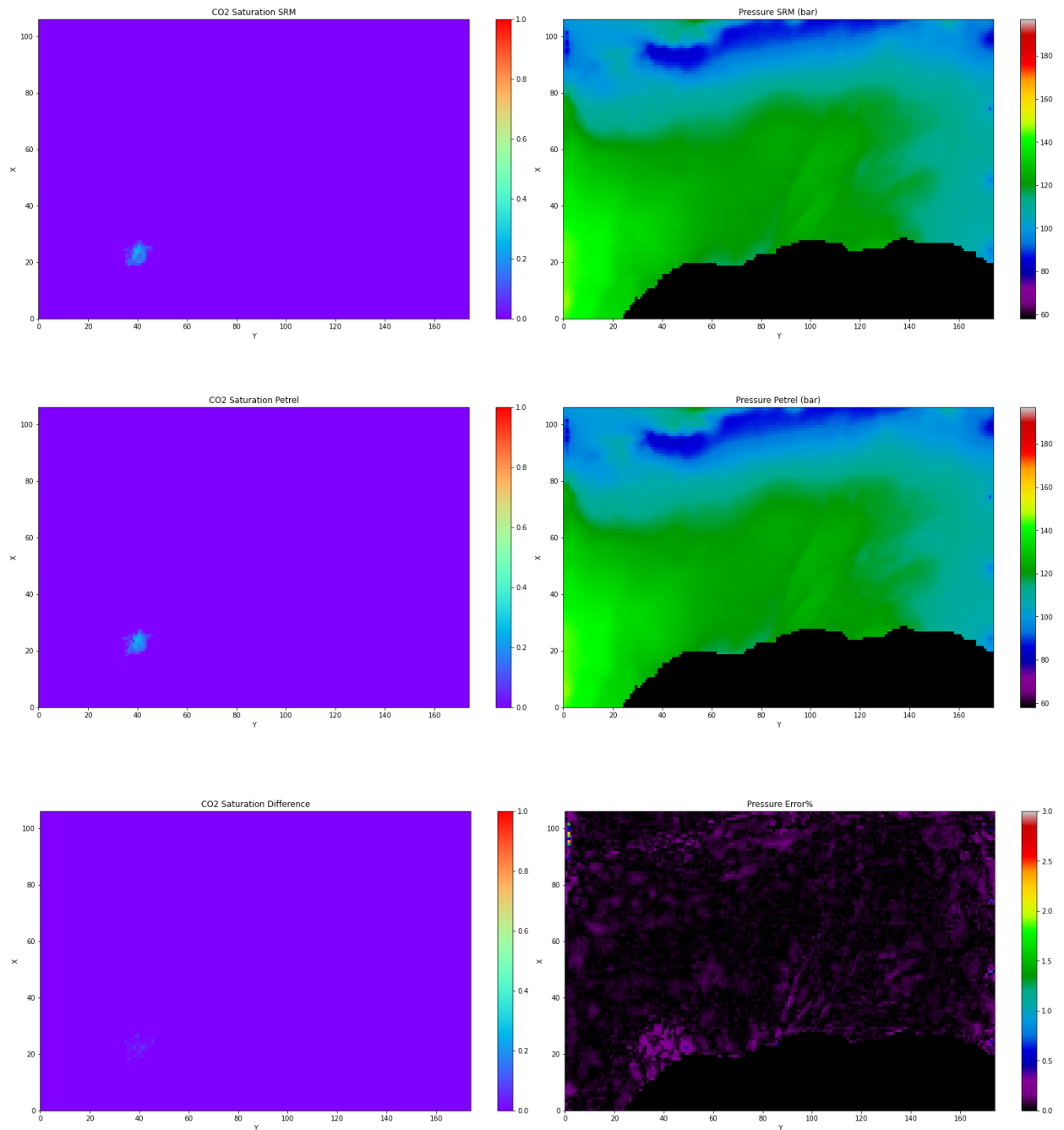


**Figure 5.10: Pressure and CO<sub>2</sub> saturation distribution and error maps in the case of 25 years injection with the rate of  $1798810 \text{ Sm}^3/\text{day}$ , 30<sup>th</sup> layer**

25 years injection with the rate of  $1798810 \text{ Sm}^3/\text{day}$ , 40<sup>th</sup> layer:

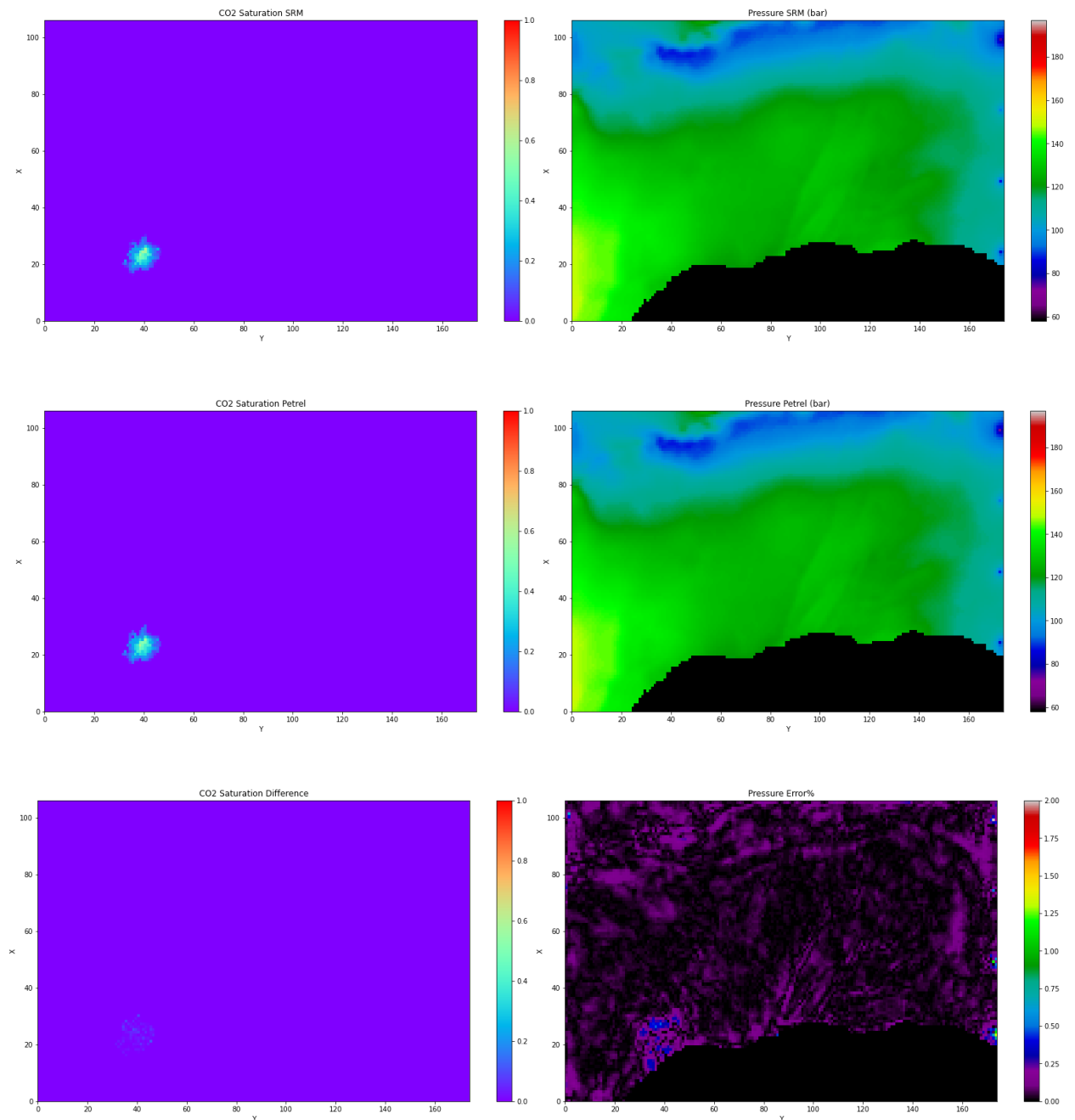


**Figure 5.11: Pressure and CO<sub>2</sub> saturation distribution and error maps in the case of 25 years injection with the rate of  $1798810 \text{ Sm}^3/\text{day}$ , 40<sup>th</sup> layer**

25 years injection with the rate of  $1798810 \text{ Sm}^3/\text{day}$ , 50<sup>th</sup> layer:

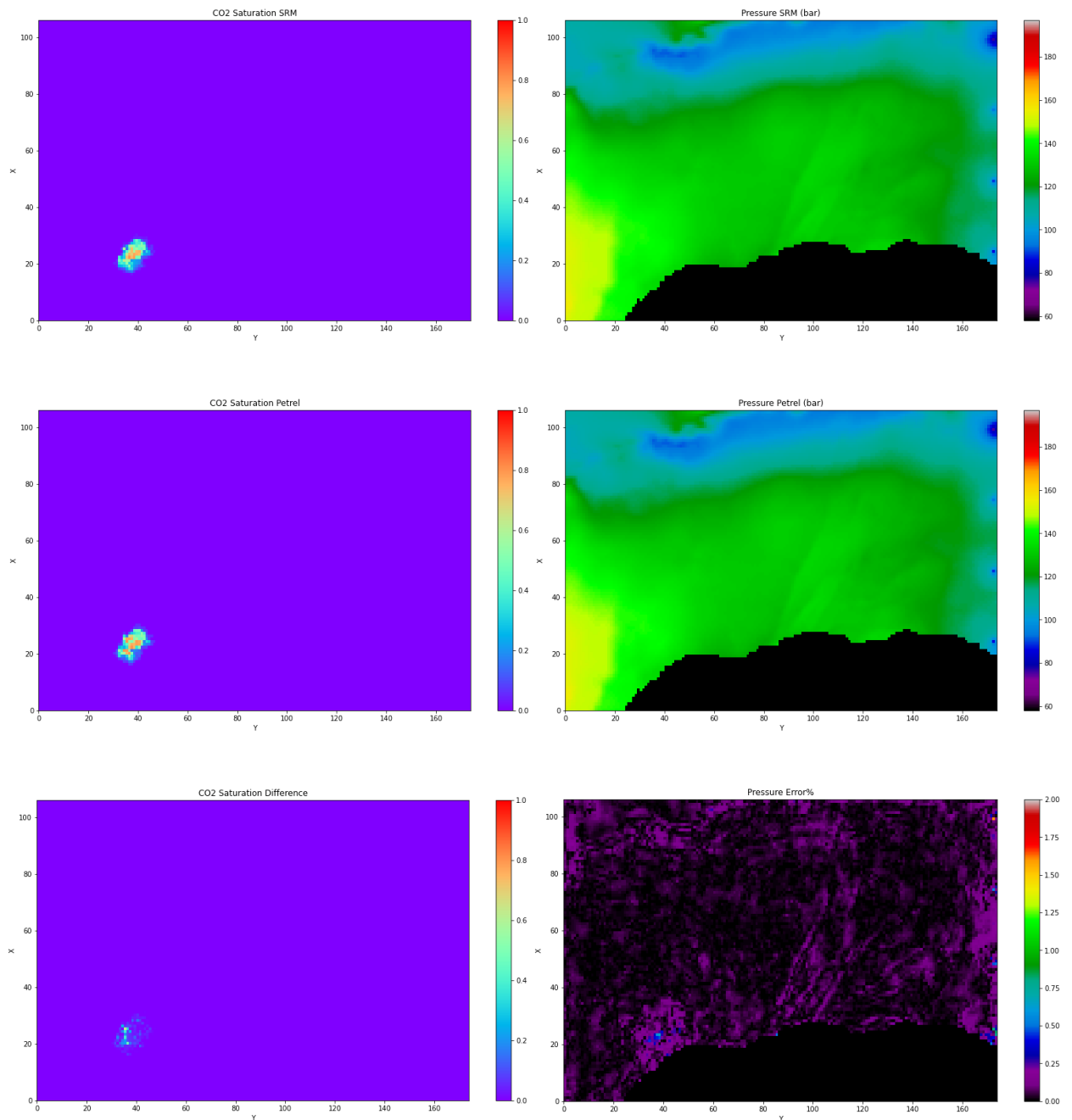


**Figure 5.12: Pressure and CO<sub>2</sub> saturation distribution and error maps in the case of 25 years injection with the rate of  $1798810 \text{ Sm}^3/\text{day}$ , 50<sup>th</sup> layer**

50 years injection with the rate of  $1798810 \text{ Sm}^3/\text{day}$ , 1<sup>st</sup> layer:

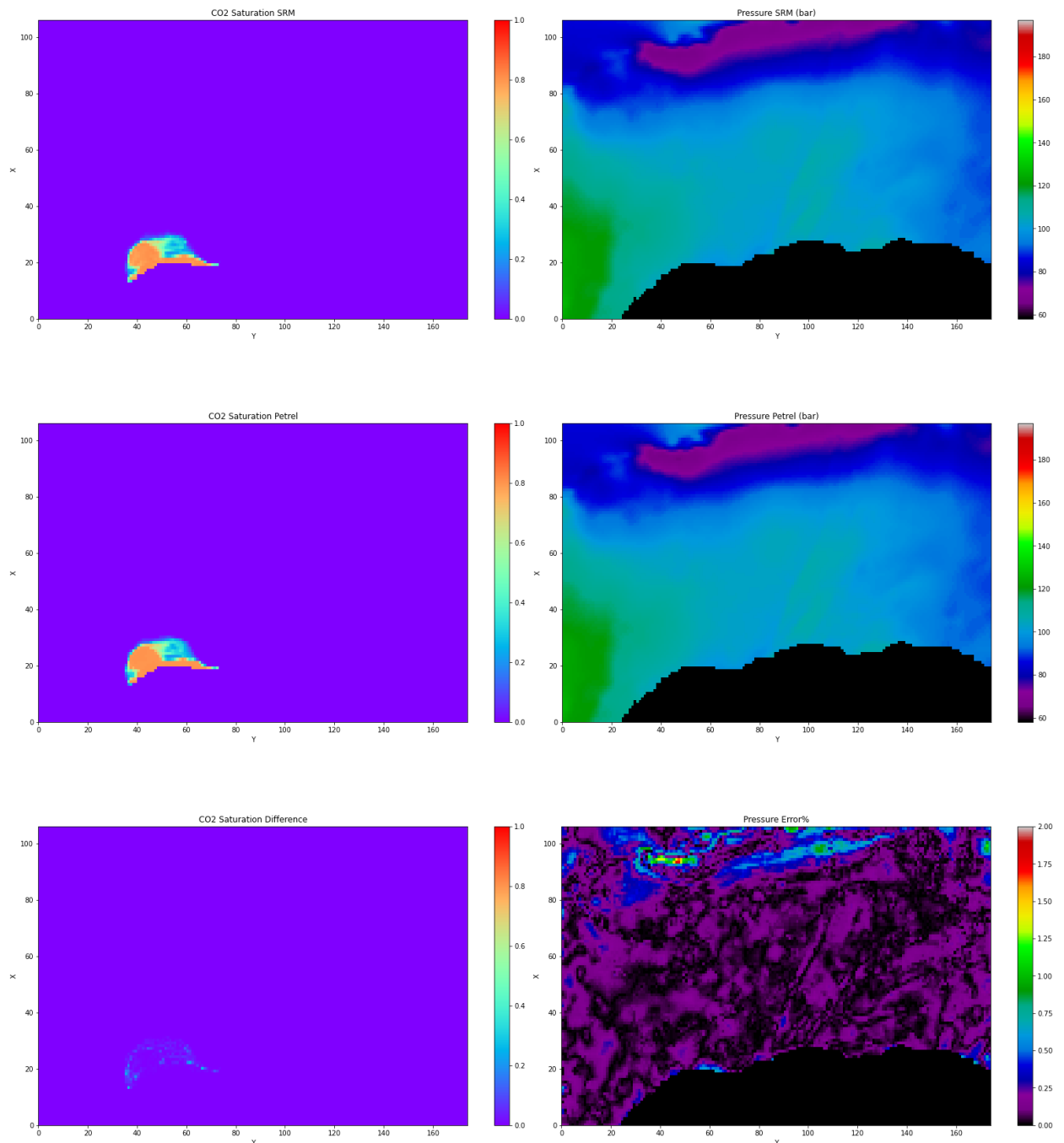


**Figure 5.13: Pressure and CO<sub>2</sub> saturation distribution and error maps in the case of 50 years injection with the rate of  $1798810 \text{ Sm}^3/\text{day}$ , 1<sup>st</sup> layer**

50 years injection with the rate of  $1798810 \text{ Sm}^3/\text{day}$ , 2<sup>nd</sup> layer:

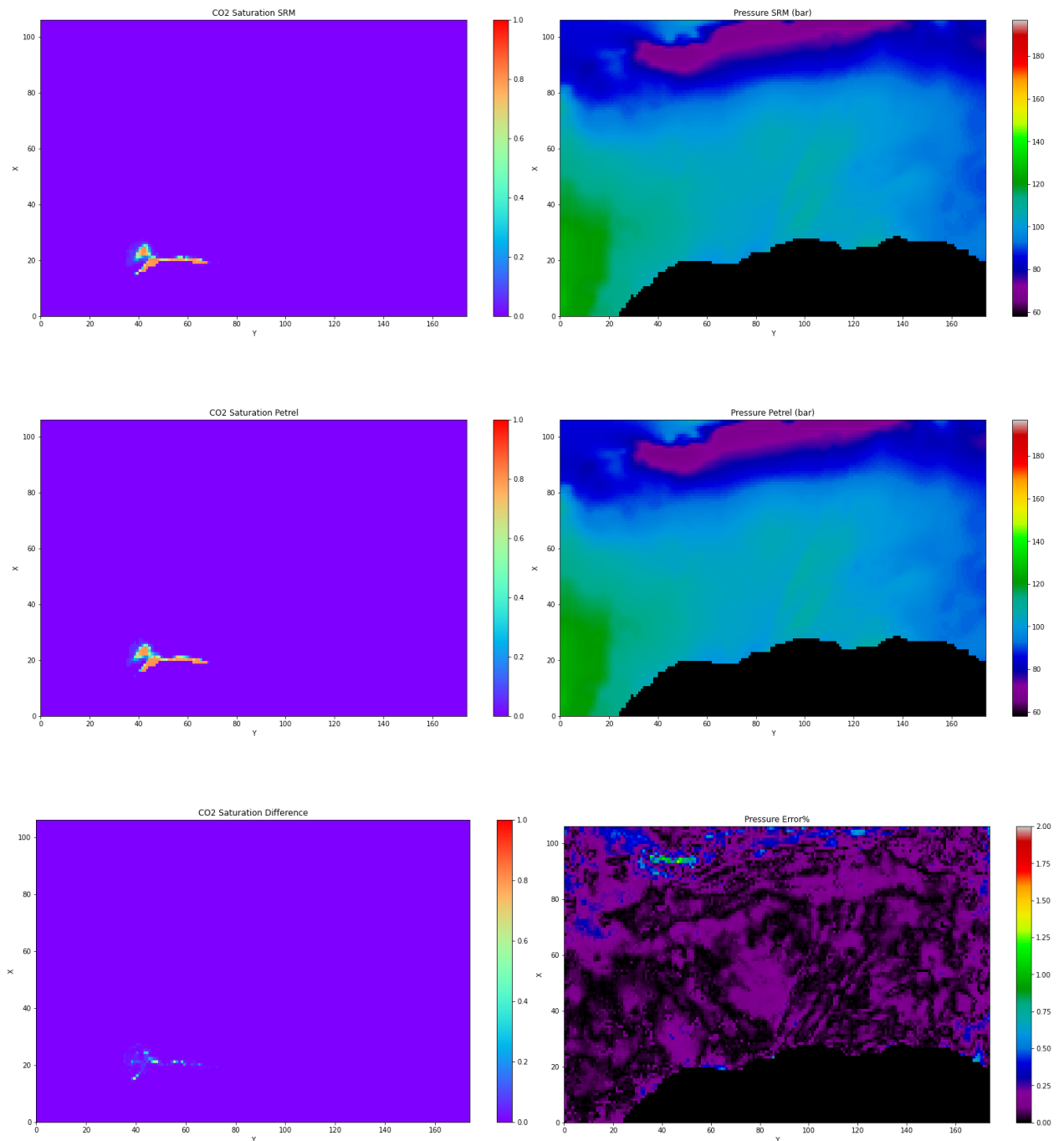


**Figure 5.14: Pressure and CO<sub>2</sub> saturation distribution and error maps in the case of 50 years injection with the rate of  $1798810 \text{ Sm}^3/\text{day}$ , 2<sup>nd</sup> layer**

50 years injection with the rate of  $1798810 \text{ Sm}^3/\text{day}$ , 40<sup>th</sup> layer:

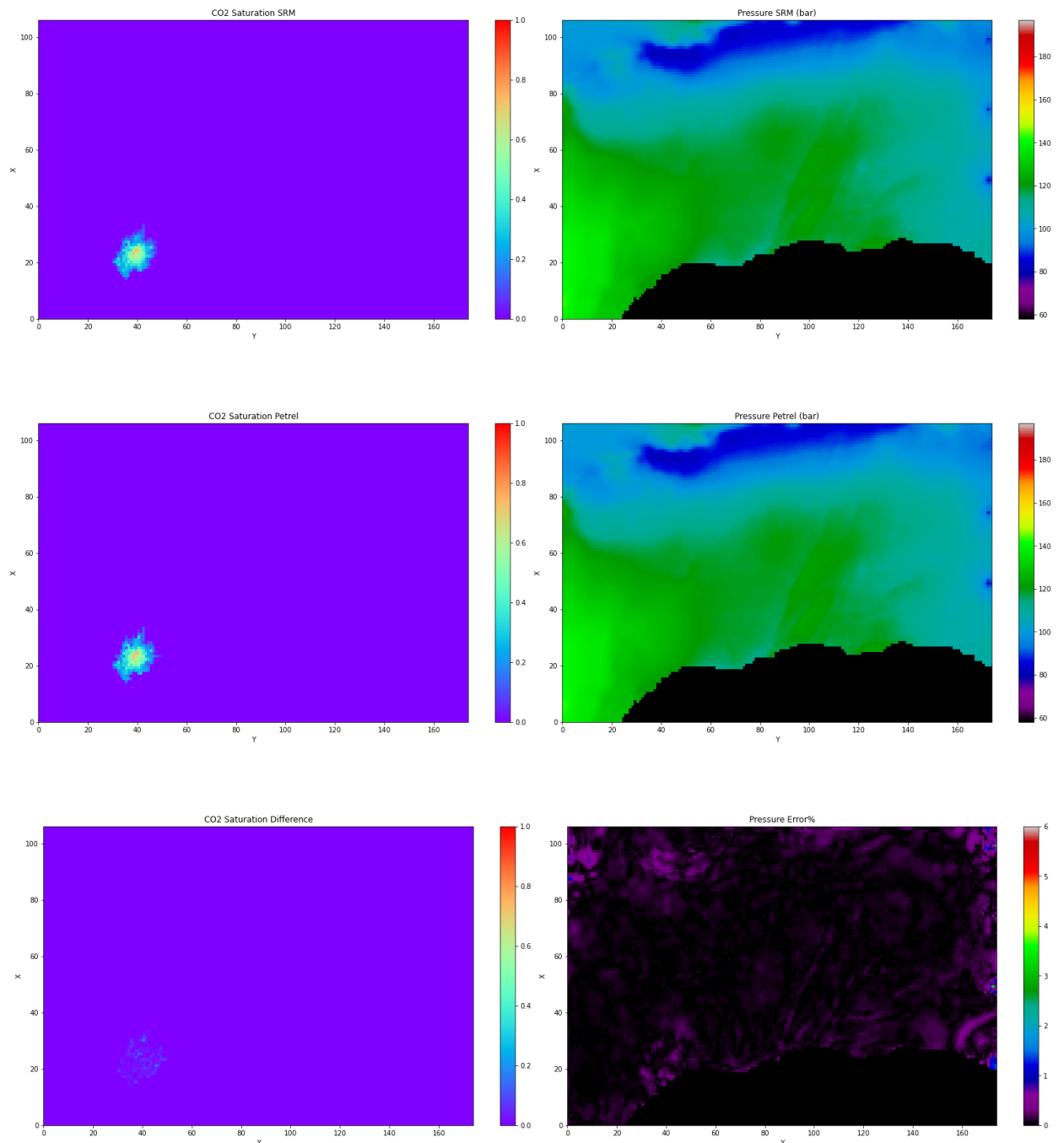


**Figure 5.15: Pressure and CO<sub>2</sub> saturation distribution and error maps in the case of 50 years injection with the rate of  $1798810 \text{ Sm}^3/\text{day}$ , 40<sup>th</sup> layer**

25 years injection with the rate of  $7610350 \text{ Sm}^3/\text{day}$ , 1<sup>st</sup> layer:

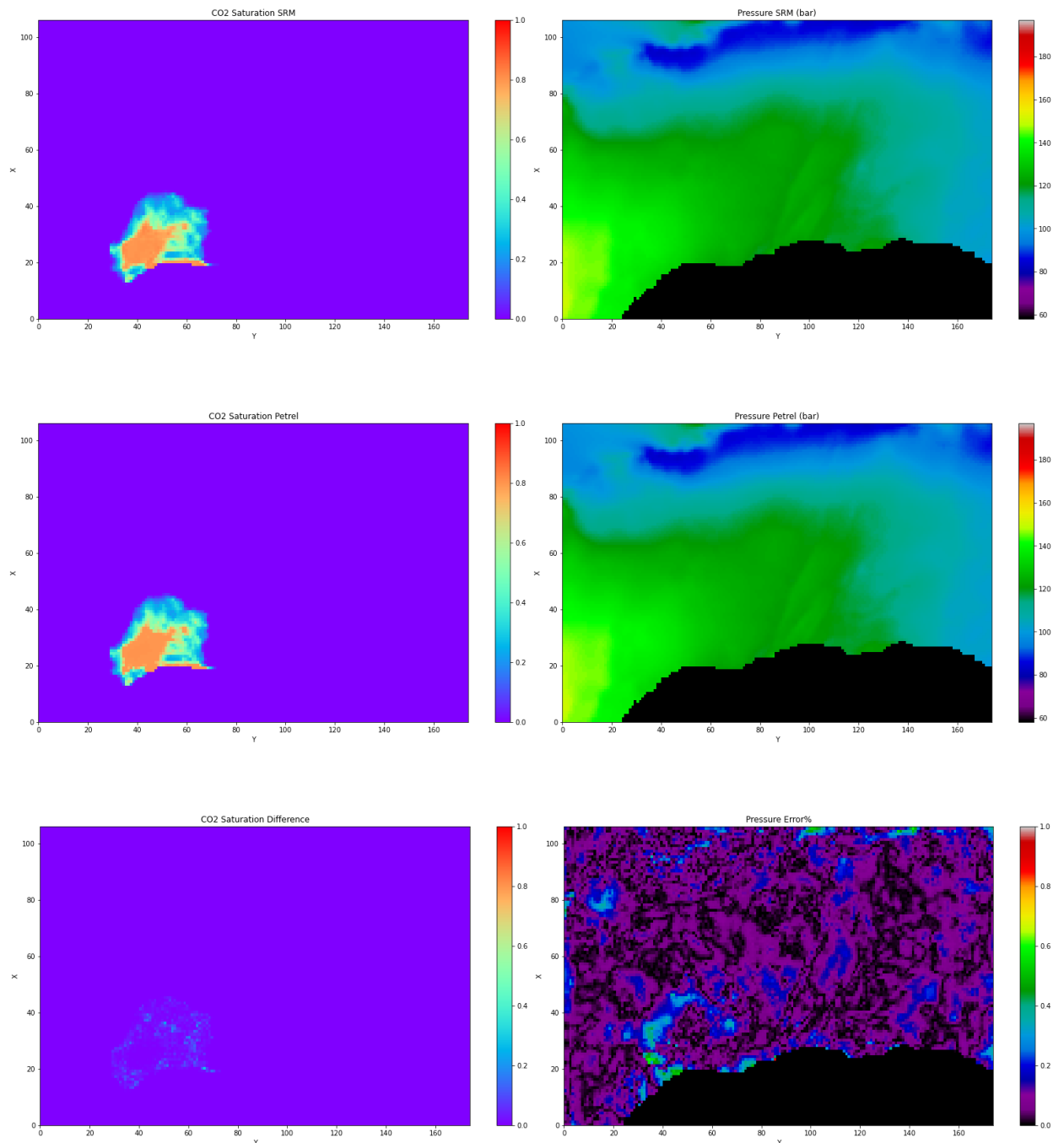


**Figure 5.16: Pressure and CO<sub>2</sub> saturation distribution and error maps in the case of 25 years injection with the rate of  $7610350 \text{ Sm}^3/\text{day}$ , 1<sup>st</sup> layer**

25 years injection with the rate of  $7610350 \text{ Sm}^3/\text{day}$ , 2<sup>nd</sup> layer:

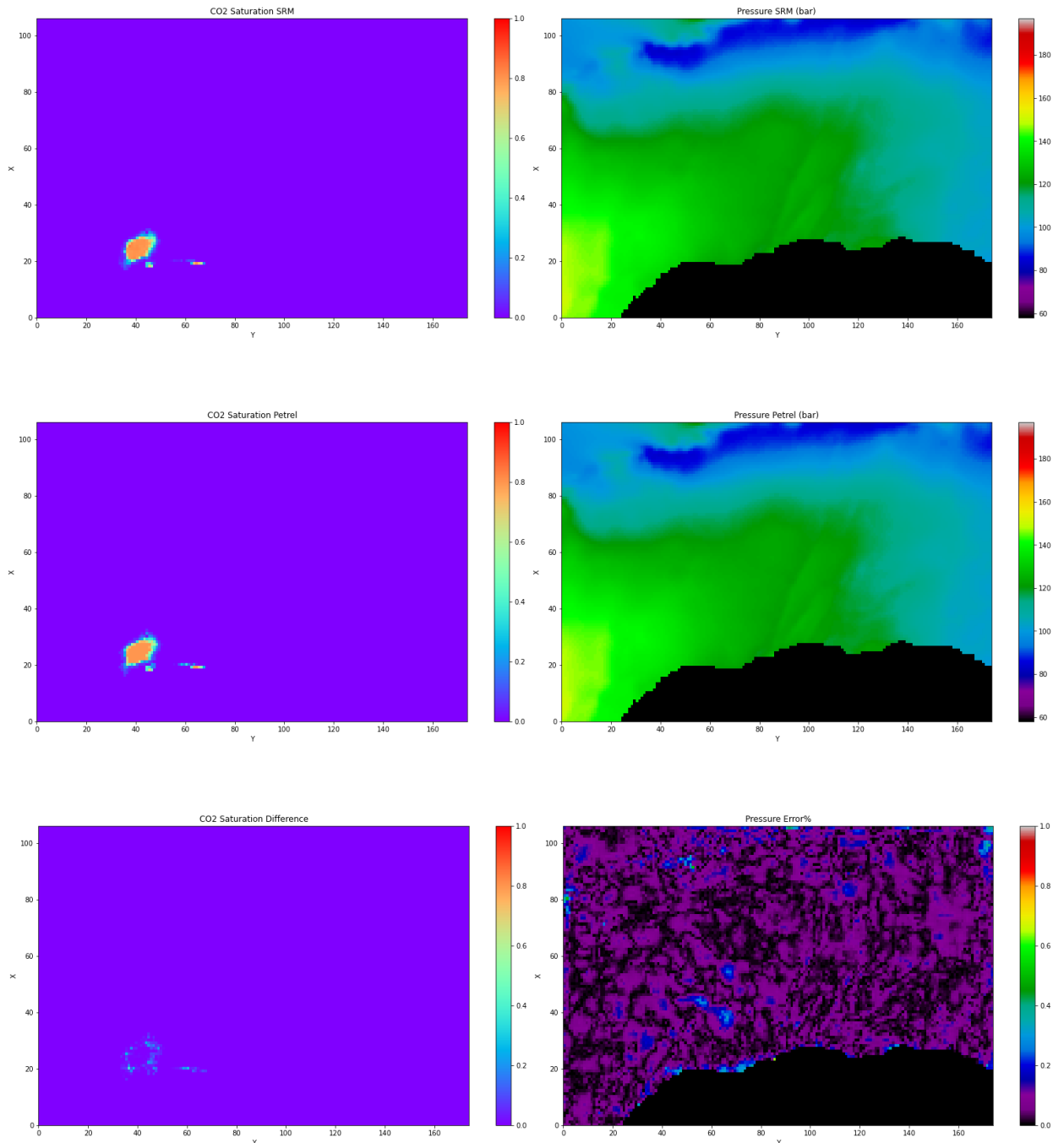


**Figure 5.17: Pressure and CO<sub>2</sub> saturation distribution and error maps in the case of 25 years injection with the rate of  $7610350 \text{ Sm}^3/\text{day}$ , 2<sup>nd</sup> layer**

25 years injection with the rate of  $7610350 \text{ Sm}^3/\text{day}$ , 70<sup>th</sup> layer:

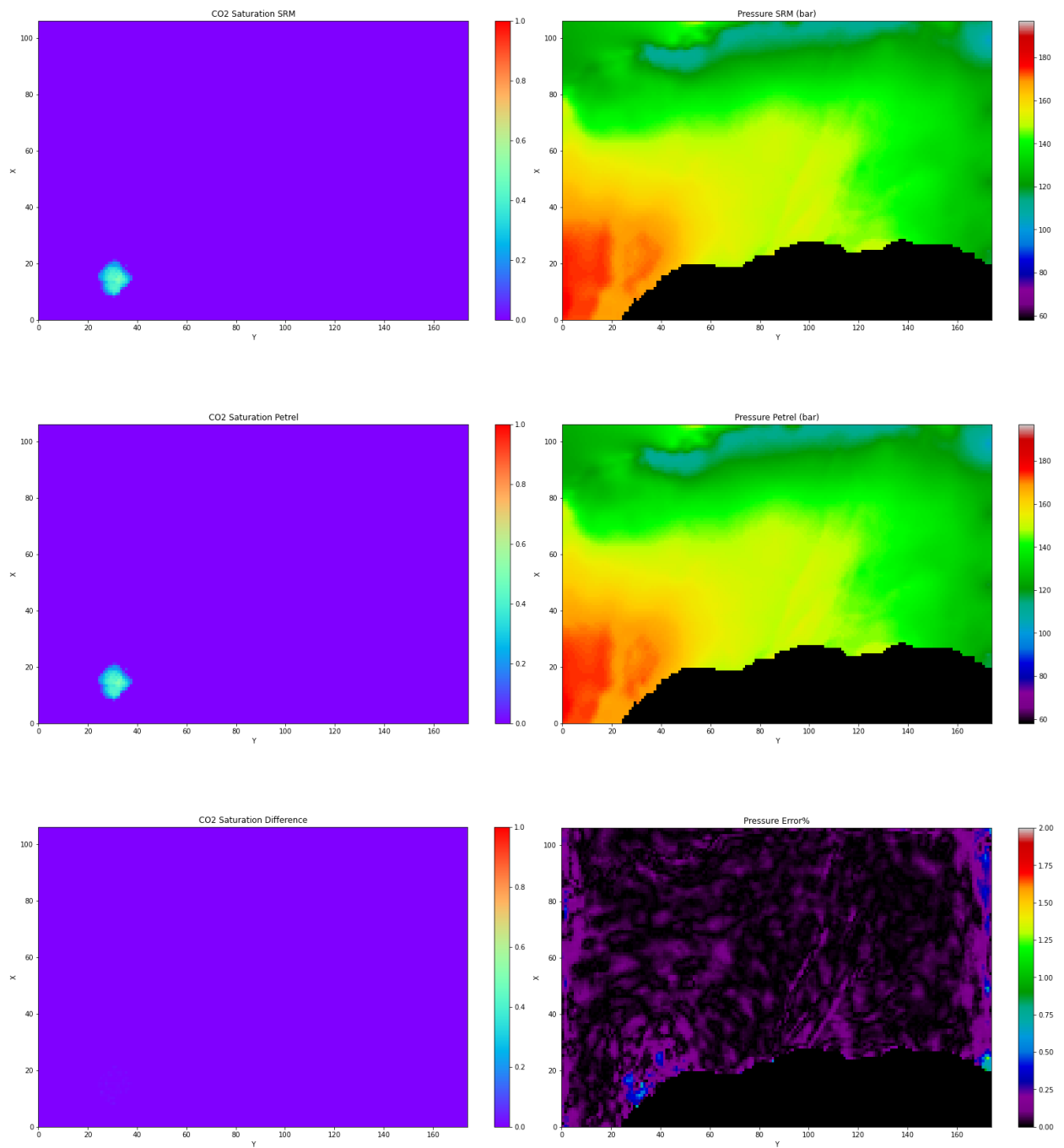


**Figure 5.18: Pressure and CO<sub>2</sub> saturation distribution and error maps in the case of 25 years injection with the rate of  $7610350 \text{ Sm}^3/\text{day}$ , 70<sup>th</sup> layer**

50 years injection with the rate of  $7610350 \text{ Sm}^3/\text{day}$ , 1<sup>st</sup> layer:

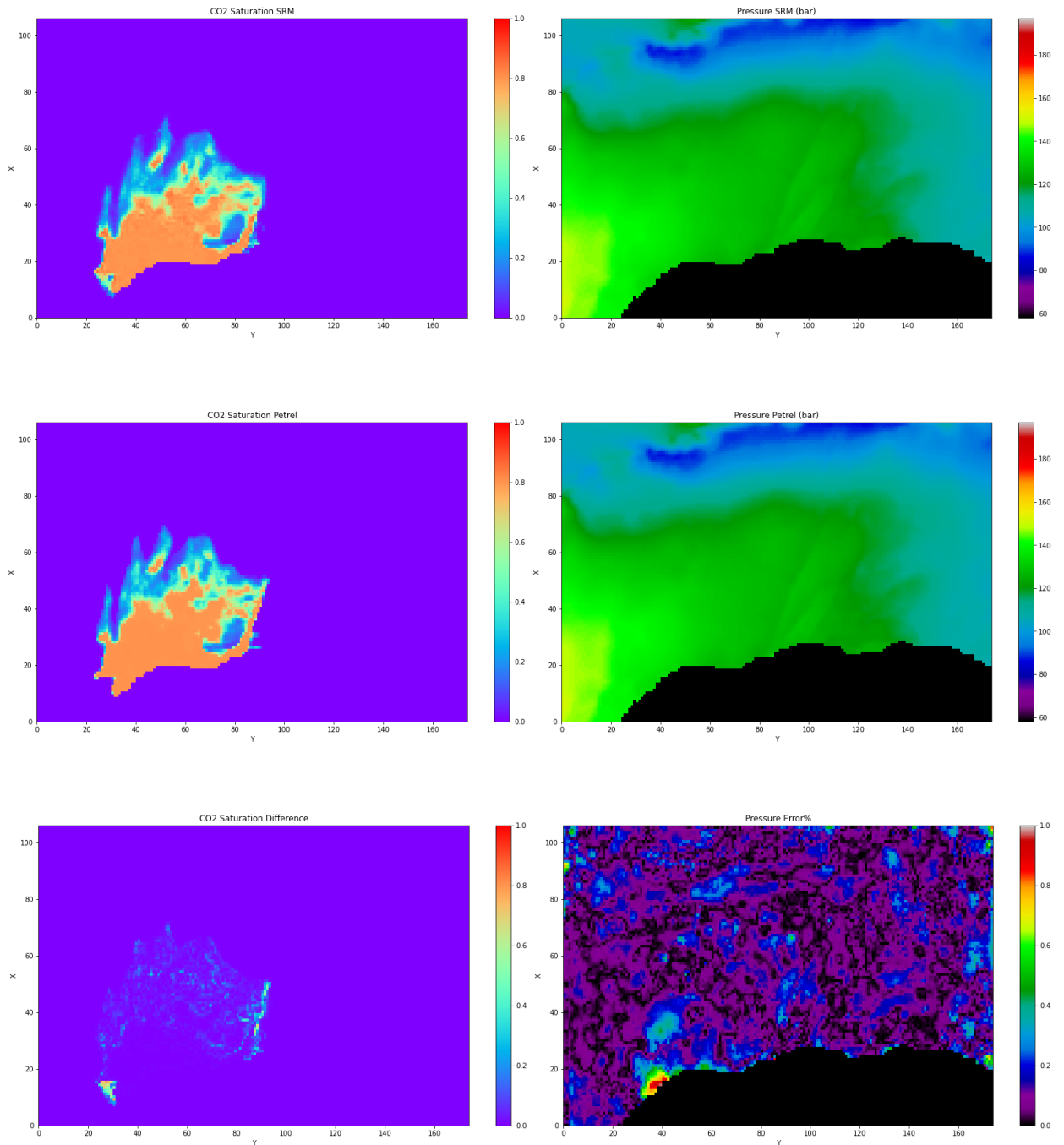


**Figure 5.19: Pressure and CO<sub>2</sub> saturation distribution and error maps in the case of 50 years injection with the rate of  $7610350 \text{ Sm}^3/\text{day}$ , 1<sup>st</sup> layer**

50 years injection with the rate of  $7610350 \text{ Sm}^3/\text{day}$ , 2<sup>nd</sup> layer:

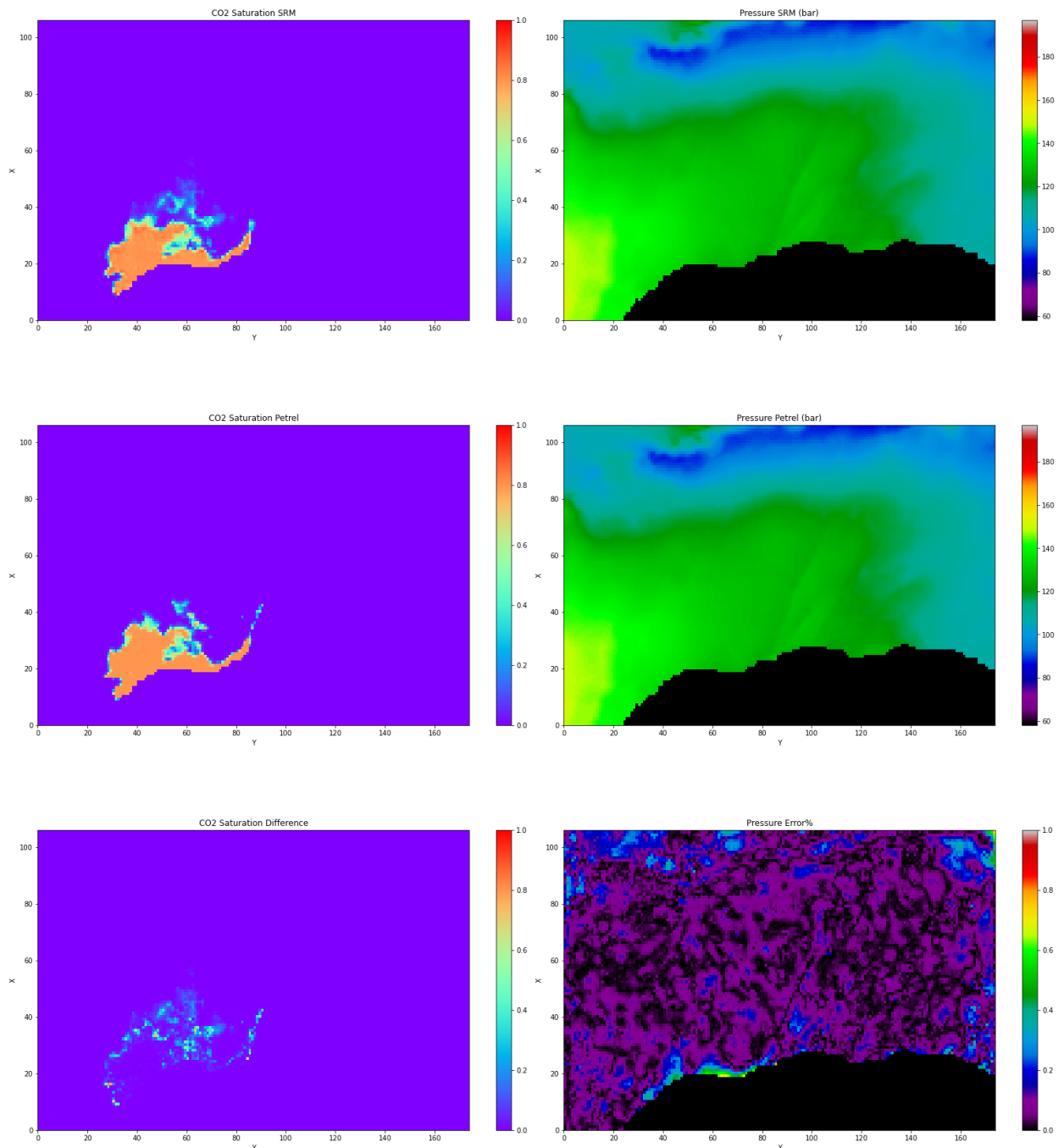


**Figure 5.20: Pressure and CO<sub>2</sub> saturation distribution and error maps in the case of 50 years injection with the rate of  $7610350 \text{ Sm}^3/\text{day}$ , 2<sup>nd</sup> layer**

50 years injection with the rate of  $7610350 \text{ Sm}^3/\text{day}$ , 50<sup>th</sup> layer:

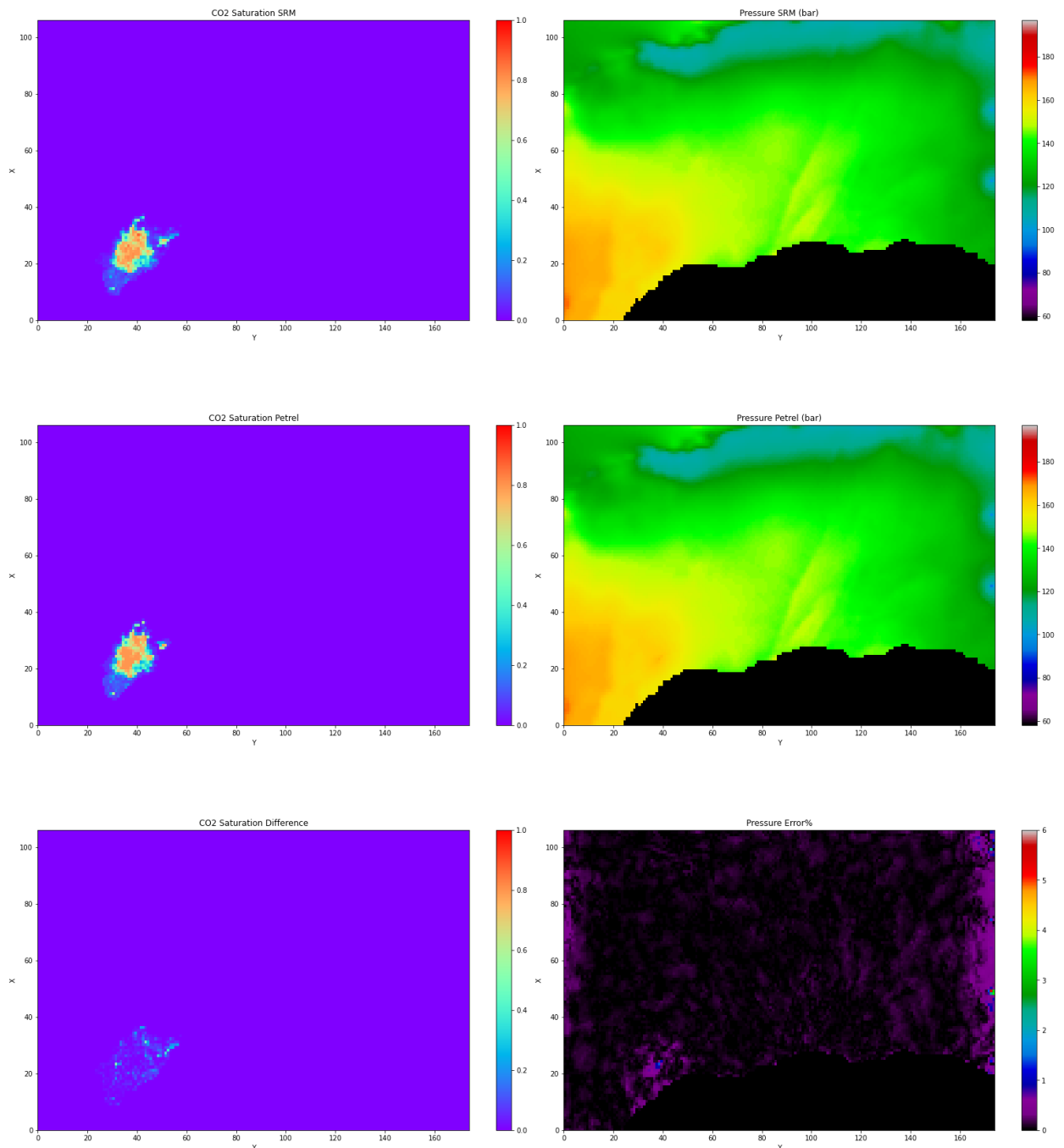


**Figure 5.21: Pressure and CO<sub>2</sub> saturation distribution and error maps in the case of 50 years injection with the rate of  $7610350 \text{ Sm}^3/\text{day}$ , 50<sup>th</sup> layer**

### 5.2.2 Blind Evaluation Result

25 years injection with the rate of  $3459250 \text{ Sm}^3/\text{day}$ , 1<sup>st</sup> layer:

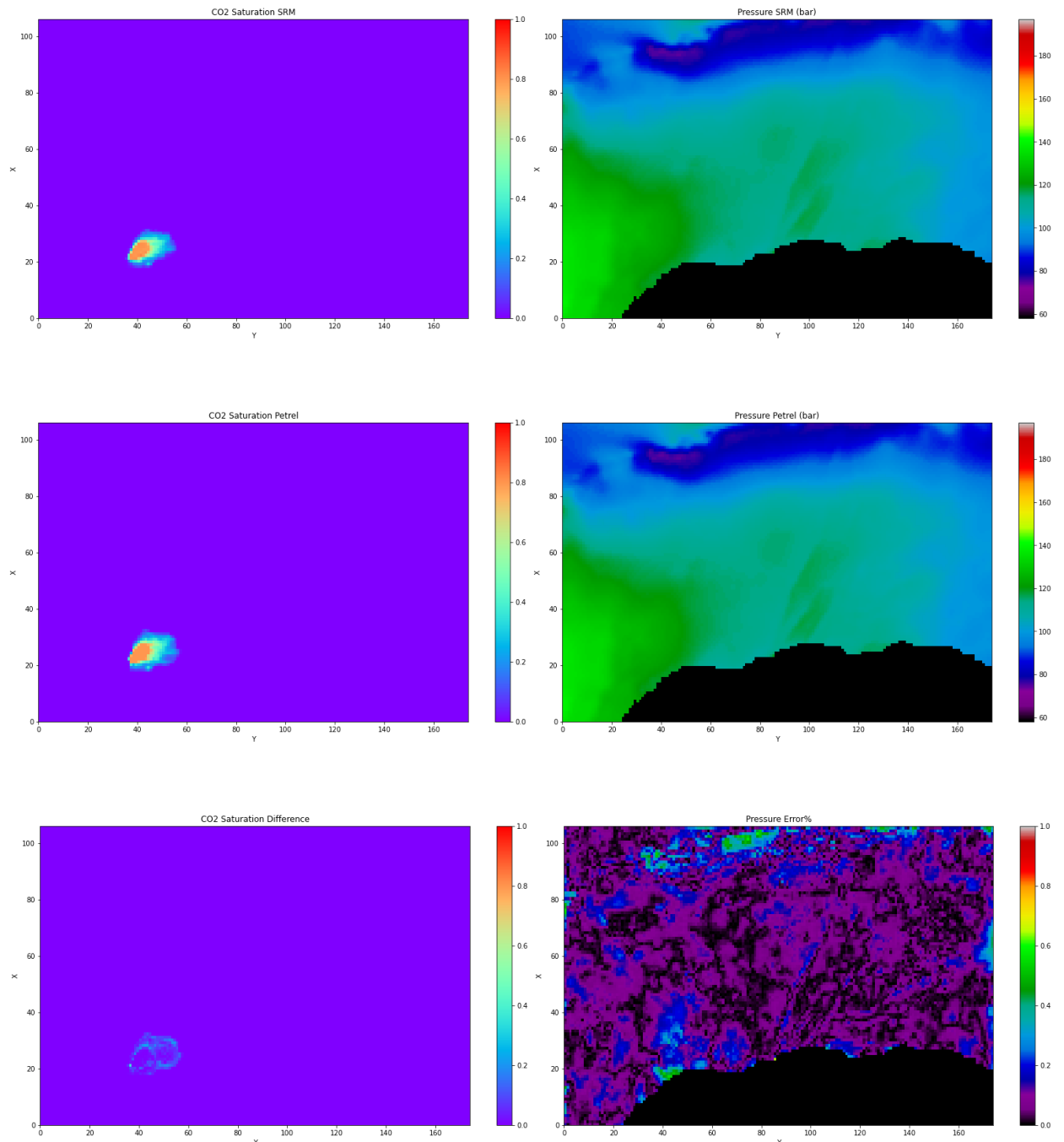


**Figure 5.22: Pressure and CO<sub>2</sub> saturation distribution and error maps in the case of 25 years injection with the rate of  $3459250 \text{ Sm}^3/\text{day}$ , 1<sup>st</sup> layer**

25 years injection with the rate of  $3459250 \text{ Sm}^3/\text{day}$ , 40<sup>th</sup> layer:

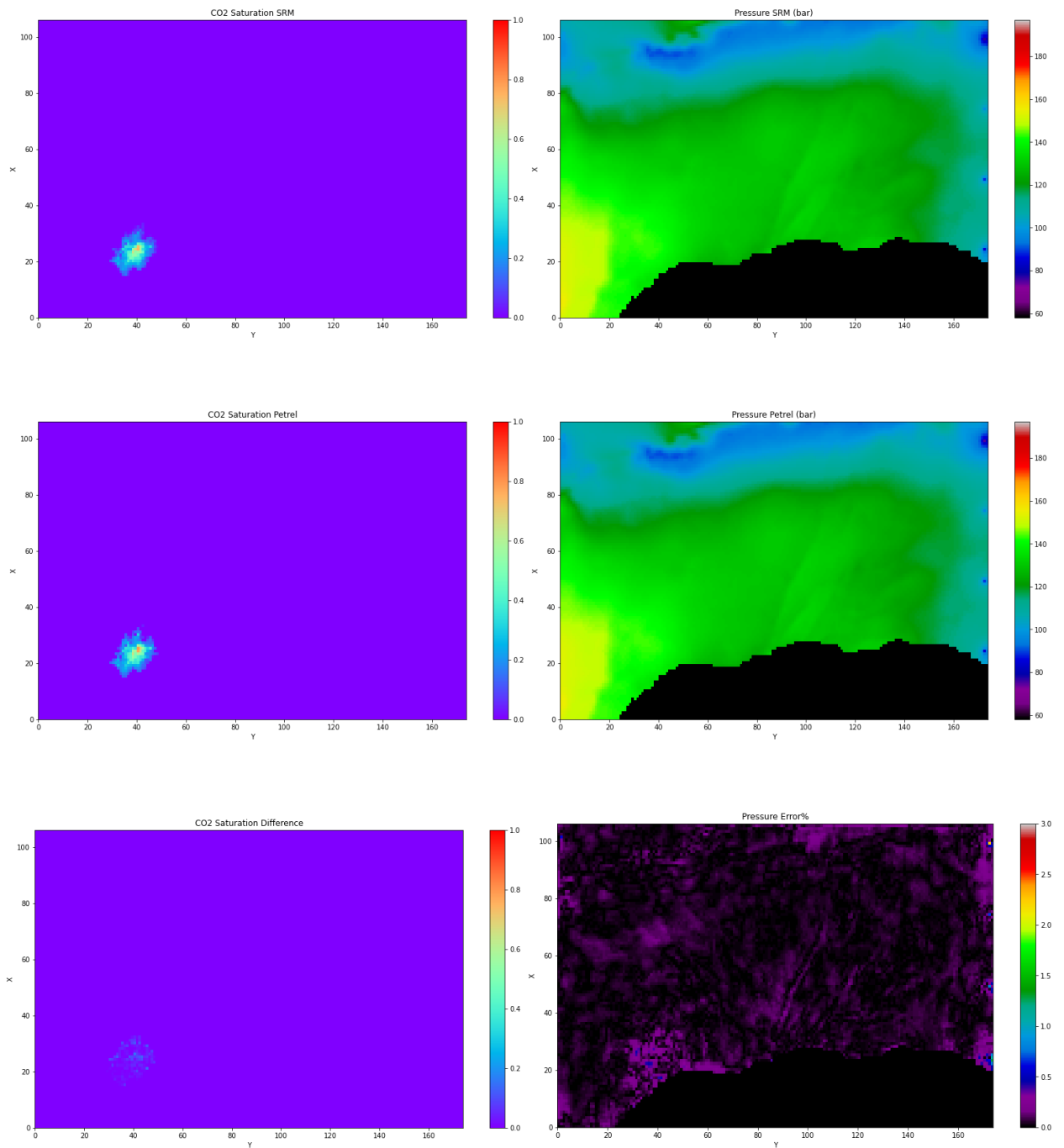


**Figure 5.23: Pressure and CO<sub>2</sub> saturation distribution and error maps in the case of 25 years injection with the rate of  $3459250 \text{ Sm}^3/\text{day}$ , 40<sup>th</sup> layer**

25 years injection with the rate of  $3459250 \text{ Sm}^3/\text{day}$ , 50<sup>th</sup> layer:

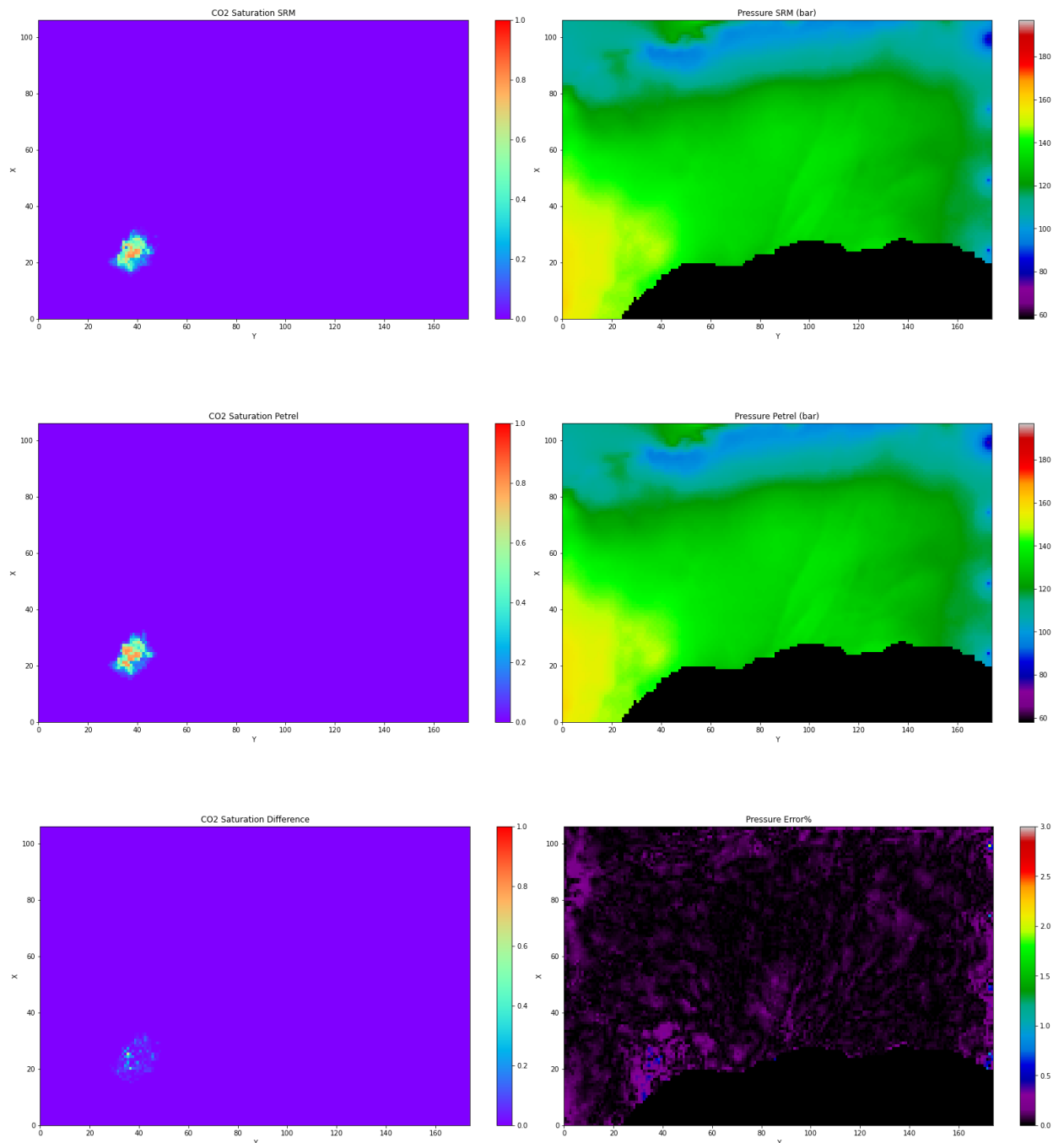


**Figure 5.24: Pressure and CO<sub>2</sub> saturation distribution and error maps in the case of 25 years injection with the rate of  $3459250 \text{ Sm}^3/\text{day}$ , 50<sup>th</sup> layer**

50 years injection with the rate of  $3459250 \text{ Sm}^3/\text{day}$ , 1<sup>st</sup> layer:

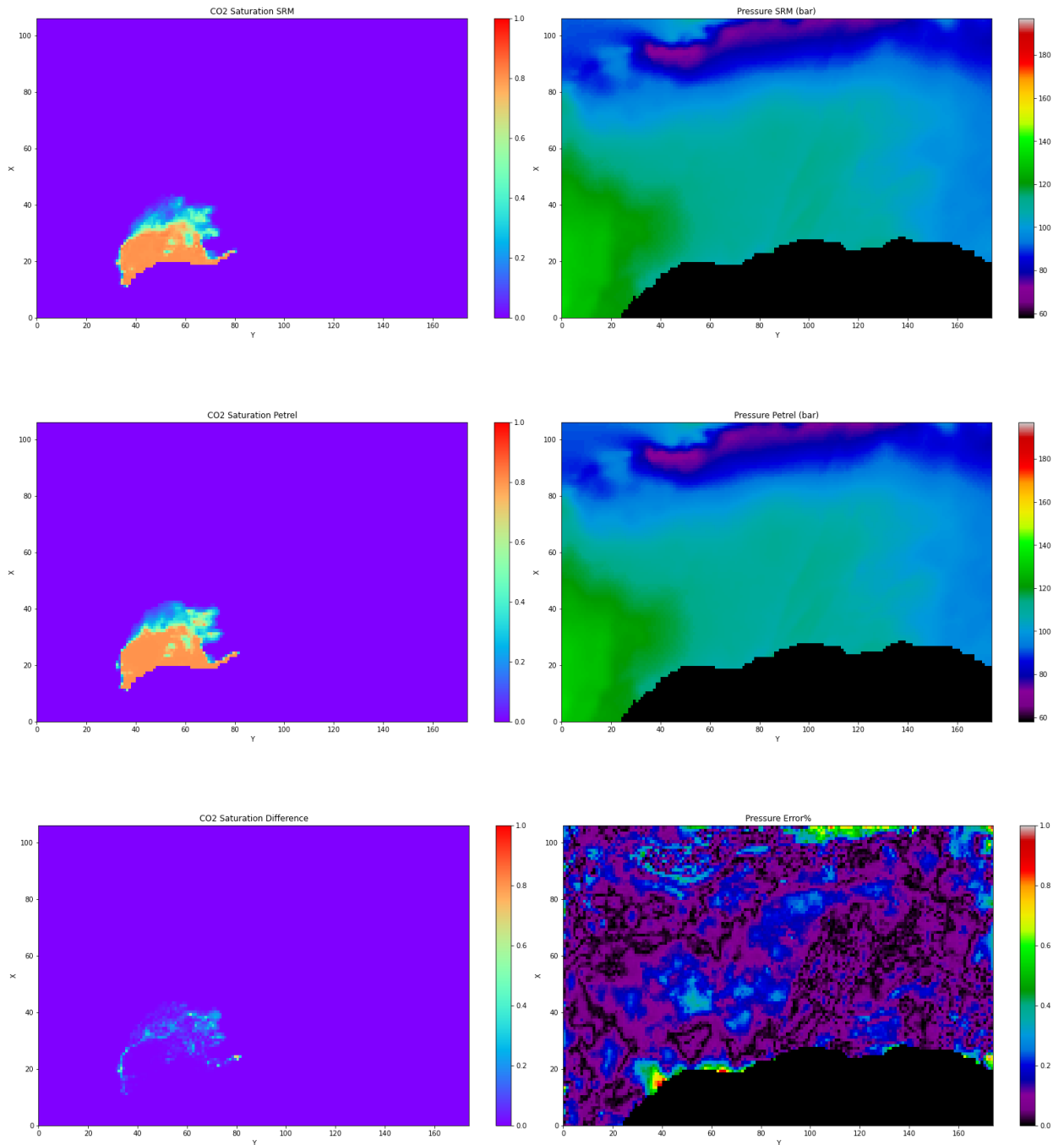


**Figure 5.25: Pressure and CO<sub>2</sub> saturation distribution and error maps in the case of 50 years injection with the rate of  $3459250 \text{ Sm}^3/\text{day}$ , 1<sup>st</sup> layer**

50 years injection with the rate of  $3459250 \text{ Sm}^3/\text{day}$ , 2<sup>nd</sup> layer:

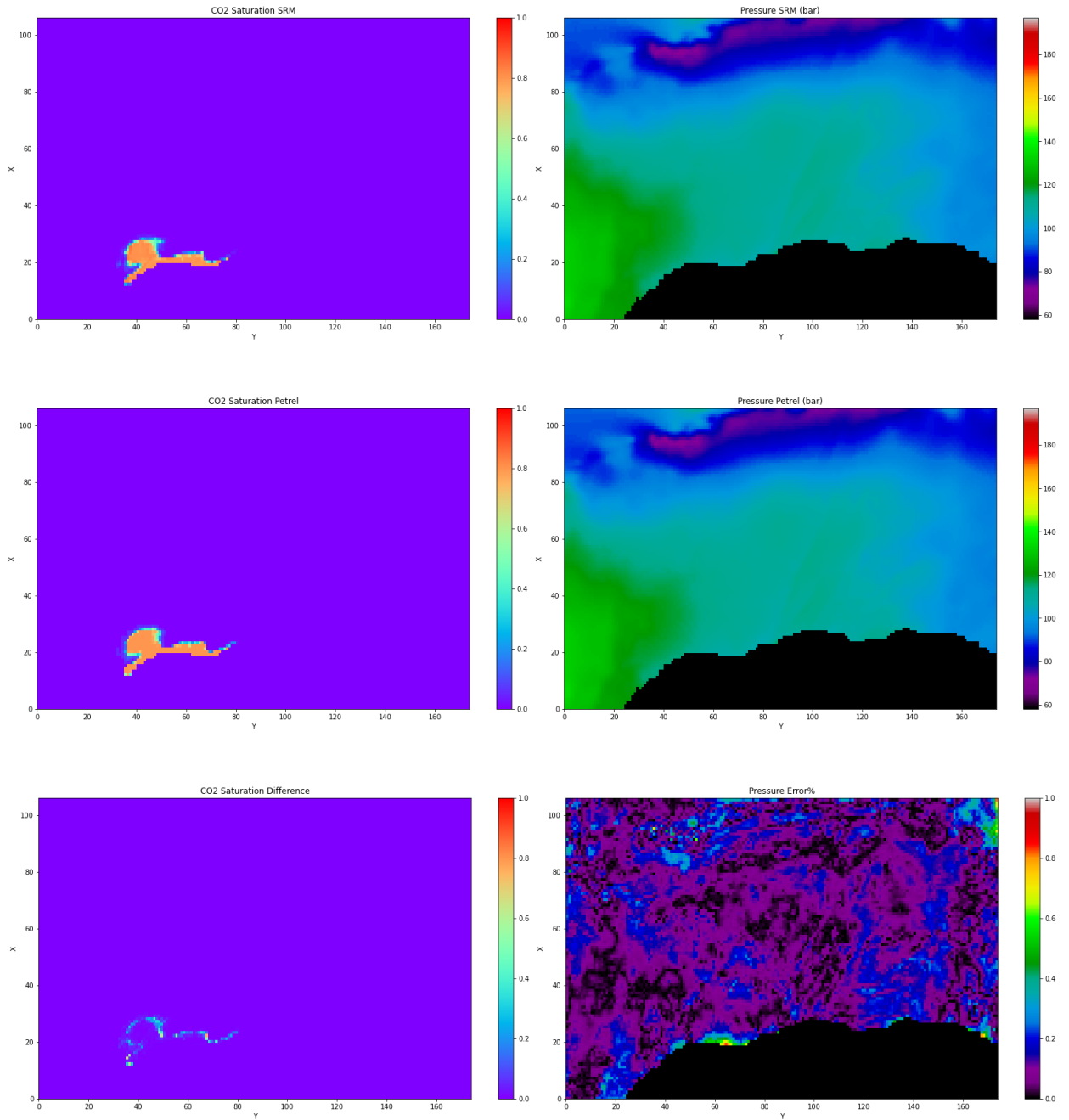


**Figure 5.26: Pressure and CO<sub>2</sub> saturation distribution and error maps in the case of 50 years injection with the rate of  $3459250 \text{ Sm}^3/\text{day}$ , 2<sup>nd</sup> layer**

50 years injection with the rate of  $3459250 \text{ Sm}^3/\text{day}$ , 50<sup>th</sup> layer:

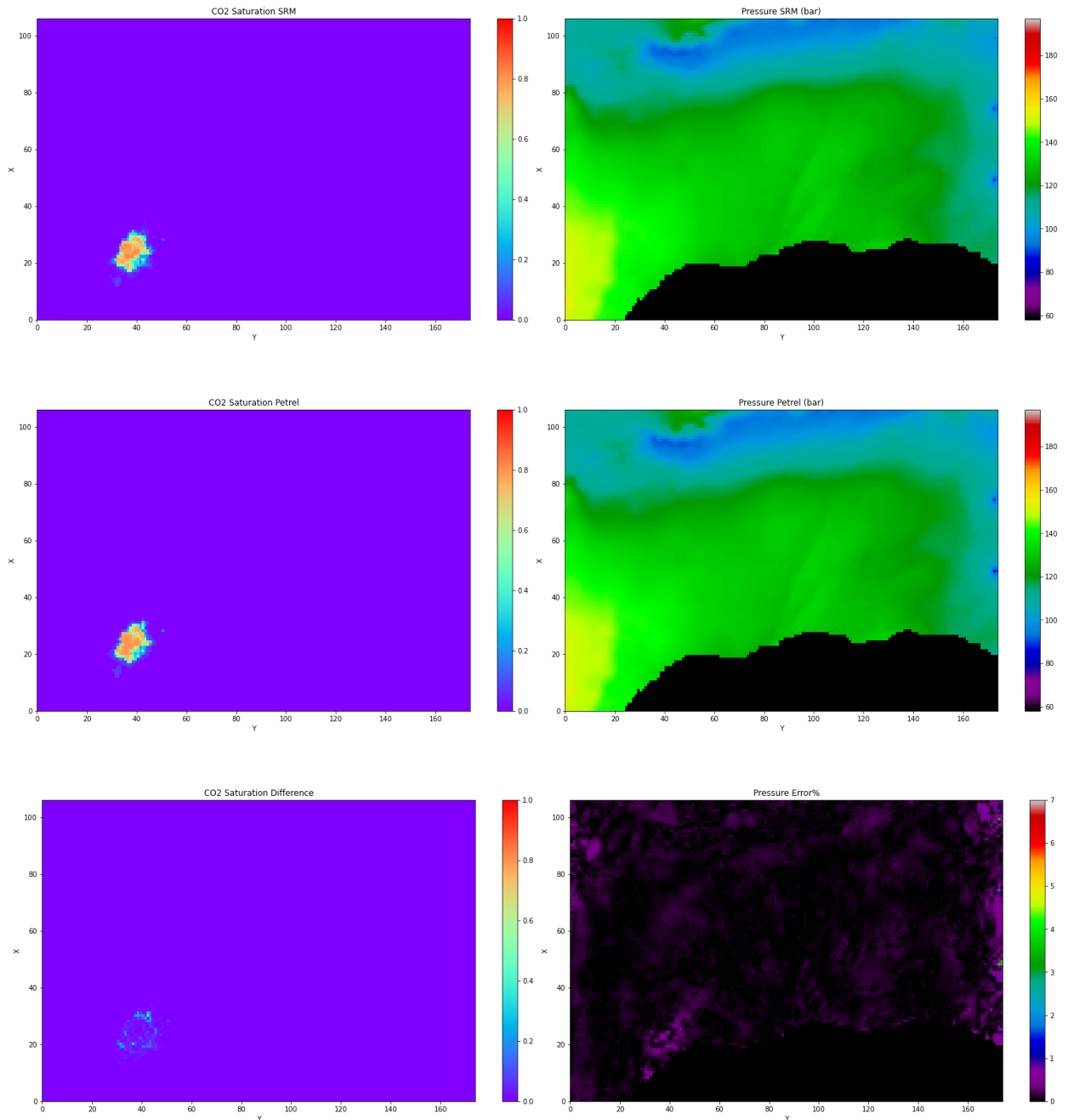


**Figure 5.27: Pressure and CO<sub>2</sub> saturation distribution and error maps in the case of 50 years injection with the rate of  $3459250 \text{ Sm}^3/\text{day}$ , 50<sup>th</sup> layer**

### 5.3 Optimization Result

The GA found the best population with 100 individuals after replacing 100 generations. The optimum rate and injection time that leads to maximum injected CO<sub>2</sub> without exceeding the constraints refers to the first individual in the last population. Table 5.1 represents the first 20 individuals in the best population. According to the table, injecting CO<sub>2</sub> with the optimum rate of 4683495 sm<sup>3</sup>/day for 50 years will store nearly 160 Mt CO<sub>2</sub> safely. Consequently, near 3.2 Mt CO<sub>2</sub> must be supplied annually, a reasonable value according to the CCS acceleration and companies' investments.

**Table 5.1: The final population of the optimization**

Rank	Rate (Sm <sup>3</sup> /day)	Time Step	Injected volume (Sm <sup>3</sup> )
1	4683495	100	85473783750
2	4683444	100	85472853000
3	4683330	100	85470772500
4	4682244	100	85450953000
5	4681683	100	85440714750
6	4681379	100	85435166750
7	4681288	100	85433506000
8	4680804	100	85424673000
9	4680091	100	85411660750
10	4678354	100	85379960500
11	4677049	100	85356144250
12	4675390	100	85325867500
13	4673537	100	85292050250
14	4673406	100	85289659500
15	4671223	100	85249819750
16	4669713	100	85222262250
17	4668789	100	85205399250
18	4667985	100	85190726250
19	4666322	100	85160376500
20	4665829	100	85151379250

#### 5.3.1 Optimum Plan Validation and Visualization

As the optimization is performed with the proxy model, there is the possibility of prediction error. On the other hand, the constraint on the CO<sub>2</sub> saturation is approximately fixed, and it is required to check the CO<sub>2</sub> plume migration in the post-injection period.

Therefore, a simulation case with the optimum CO<sub>2</sub> injection rate and time should be built not only to simulate the injection period but also to monitor a few years after stopping the injection. In the designed case, the injection begins in 2022 until 2072, and the simulation will be continued until 2100. Figure 5.28 demonstrates the CO<sub>2</sub> saturation distribution in 2100 without any evidence of CO<sub>2</sub> migration toward zone Beta. The optimum injection rate and period will be employed to verify the optimization accuracy in figure 5.29.

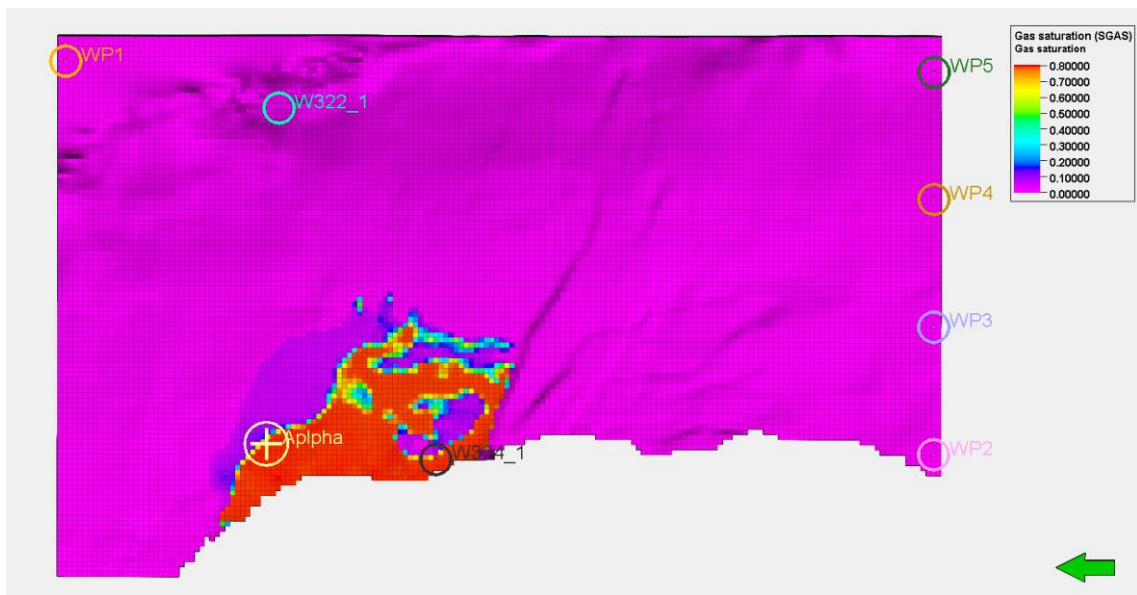


**Figure 5.28: CO<sub>2</sub> Saturation distribution in 2100, 28 years after stopping CO<sub>2</sub> injection with the rate of 4683495 Sm<sup>3</sup>/day for 50 years**

Because of shutting in the wells WP1, WP2, and WP5 in 2060, the depletion effect in the south of the storage is dominant, and the CO<sub>2</sub> plume tends to migrate to the south of the model after dying the depletion wave of well WP1.

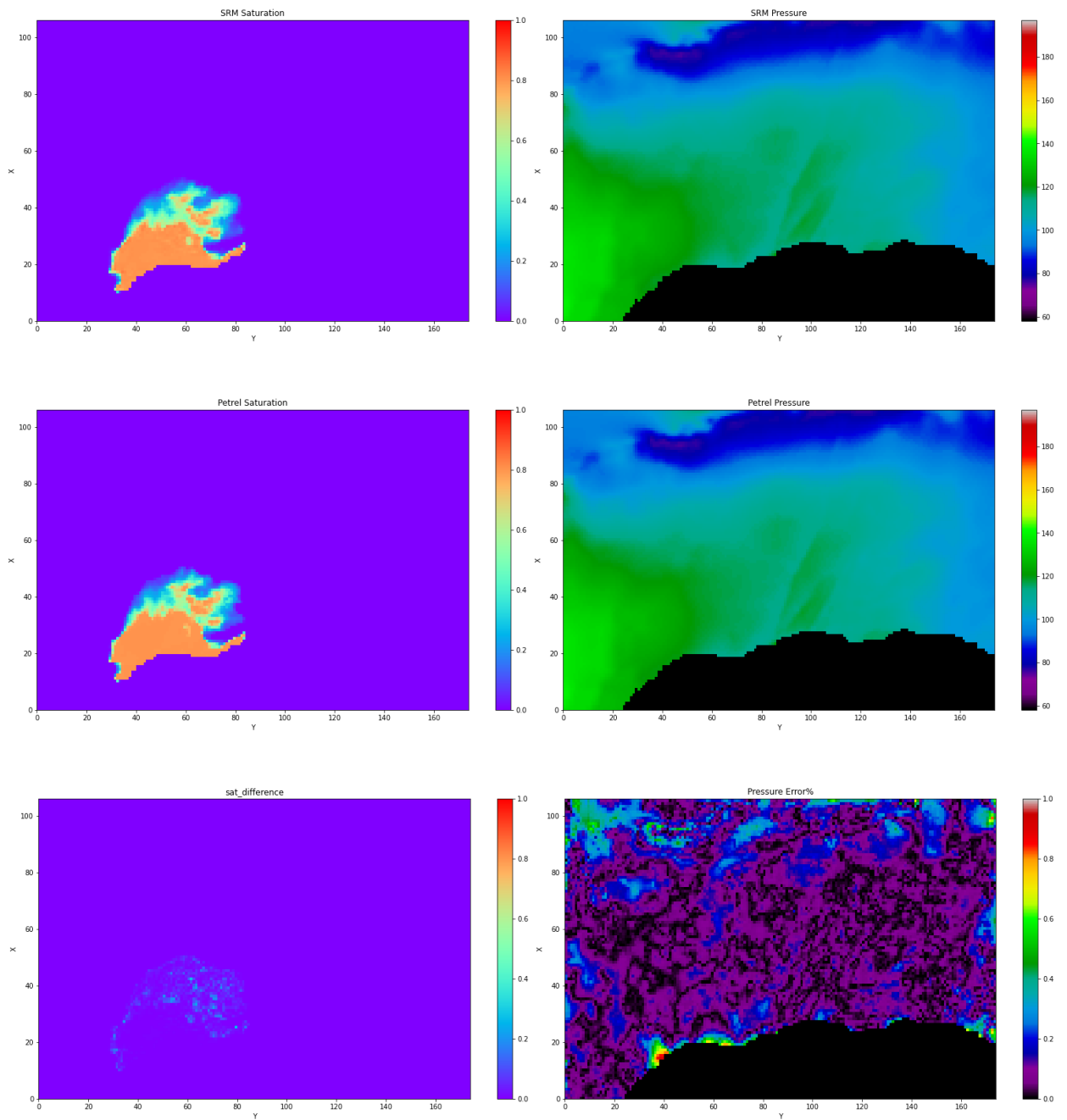


**Figure 5.29: Pressure and CO<sub>2</sub> saturation distribution and error maps in the case of 50 years injection with the rate of 4683495 Sm<sup>3</sup>/day (optimum case), 1<sup>st</sup> layer**

---

## 6 DISCUSSION

The progress of building SRM was begun by the cascading method, which splits simulation time to multiple time steps and trains one model per time step. Later, the approach modified to the non-cascading because of the cascading method disadvantages. At first, in a cascading proxy, several models for each parameter should be trained and tuned, which were complicated and required more powerful systems. As mentioned before, error accumulation is the most critical problem of this method, especially in long-term simulation. For instance, 50 models were trained to predict 50 years of CO<sub>2</sub> storage with a 1-year time step. While training and testing a single CO<sub>2</sub> saturation model, the MAE was around 1e-2, whereas the MAE reached 0.9 by a sequential blind evaluation. Additionally, the proxy is intended for optimization that needs to predict all models before the desirable time step in a cascading approach. If the current model were created with the cascading method, about 50 minutes would be taken to predict the last time step compared with numerical simulation with 6 hours and the non-cascading with 30 seconds.

Concerning the dataset, the number of introduced scenarios (simulation cases), time step, features, and sampling is influential. The model was developed with various quantity and time-step durations to enhance the proxy accuracy. A high level of improvement was not observed in reducing the time step from 6 months to 3 months, nevertheless, increasing the simulation cases helped the model generalize with a higher standard. The only excluded input features are distance to the boundary and the bottom-hole pressure. Coupling a well-based SRM with this model in future works is recommended to add the bottom hole pressure to the model, assess and optimize the injectivity, and control well bore and wellhead conditions. Sampling depends on the property behavior and distribution. When the pressure was sampled by property value variation between time steps, only the points around the injection and production wells were selected, leading to overfitting and high error in points far from wells. Random sampling avoided overfitting by selecting cells throughout the reservoir where the error in most grids is less than 0.5%.

The previous studies suggested utilizing an ANN with one hidden layer in building cascading proxies. However, in the non-cascading method, there is a giant dataset with

---

17500000 rows and 31 columns, in which situation, a simple ANN could not find the solution; in fact, underfitting occurred. Extending the model network improved the result. Not to be forgotten, too much expanding the ANN will be followed by overfitting and poorer accuracy in prediction. According to the problem structure, Relu and Sigmoid are the most appropriate activation functions. In comparison, the Relu activation has a better performance in the hidden layer, despite the fact that its presence in the output layer causes the algorithm to stick in a plateau. Employing the sigmoid in the output layer tackled the problem. Furthermore, the model training was highly sensitive to the learning rate insofar as training only with the initial rate of  $5e-4$ . On the other hand, a constant training rate resulted in shooting the solution and demand for a learning rate decay function.

The error of the CO<sub>2</sub> saturation model in almost all cells does not reach 0.1 and is accumulated chiefly at the edge of the CO<sub>2</sub> plume. This issue is more distinctive in figure 5.20, which is injected with the highest injection rate in training cases. In this order, the model can be trained with a rate more than the maximum rate of the model application.

In this study, the GA parameters were not optimized, even though the population and termination generation were modified a few times after ensuring the code and algorithm were workable. A low population or termination level may not lead to an optimum solution, but it will not be far from the global optimum. Initially, the optimization was performed with saturation constraint on the spill point between zones Alpha and Beta. The CO<sub>2</sub> plume passed from the spill point by checking the post-injection interval. Thus, the condition is set behind the spill point to provide a vacant space for post-injection CO<sub>2</sub> migration.

---

## 7 CONCLUSION

1. A non-cascading grid-based SRM is more appropriate for long-term proxy modeling and optimization.
2. The best model structure is a DNN with 3 to 5 hidden layers activated by the Relu function in the hidden layers and Sigmoid for the output layer.
3. The CO<sub>2</sub> saturation data can be sampled based on the property change in time steps, in contrast with pressure data requiring random sampling.
4. In case of memory and computer performance limitations, raising the number of simulation cases is a priority compared to the time-step reduction.
5. The maximum injection rate in training cases should be fixed more than the required rate while SRM application.
6. Proxy models provide flexibility and pace for reservoir simulation in exchange for a negligible error. According to the study results, grid-based SRMs are able to be substituted for commercial simulators in sensitivity analysis and optimization.
7. The pressure SRM with an error less than 0.5% is capable for all industrial studies, especially for coupling with Geomechanical models.
8. The captured CO<sub>2</sub> can be injected into the Smeaheia CO<sub>2</sub> storage with a rate near 3.4 Mt per year to safely store 170 Mt CO<sub>2</sub> in 50 years without any leakage or pressure violence.

## 8 REFERENCES

- Agada, S., Geiger, S., Elsheikh, A., & Oladyshkin, S. (2017). Data-driven surrogates for rapid simulation and optimization of WAG injection in fractured carbonate reservoirs. *Petroleum Geoscience*, 23(2), 270--283.  
doi:<https://doi.org/10.1144/petgeo2016-068>
- Agarwal, R. K. (2019). Modeling, simulation, and optimization of geological sequestration of CO<sub>2</sub>. *Journal of Fluids Engineering*, 141(10).  
doi:[doi:10.1115/1.4043164](https://doi.org/10.1115/1.4043164)
- Ajayi, T., Gomes, J. S., & Bera, A. (2019). A review of CO<sub>2</sub> storage in geological formations emphasizing modeling, monitoring and capacity estimation approaches. *Petroleum Science*, 16(5), 1028--1063.  
doi:<https://doi.org/10.1007/s12182-019-0340-8>
- Amini, S. (2015). *Developing a Grid-Based Surrogate Reservoir Model Using Artificial Intelligence*. West Virginia University. doi:<https://doi.org/10.33915/etd.5096>
- Amini, S., & Mohaghegh, S. (2019). Application of Machine Learning and Artificial Intelligence in Proxy Modeling for Fluid Flow in Porous Media. *Fluids*, 4(3), 126. doi:<https://doi.org/10.3390/fluids4030126>
- Ampomah, W., Balch, R., Cather, M., Will, R., Gunda, D., Dai, Z., & Soltanian, M. (2017). Optimum design of CO<sub>2</sub> storage and oil recovery under geological uncertainty. *Applied Energy*, 195, 80--92.  
doi:<https://doi.org/10.1016/j.apenergy.2017.03.017>
- Arlota, C., & de Medeiros Costa, H. (2021). Climate change, Carbon Capture and Storage (CCS), energy transition, and justice: where we are now, and where are (should be) we headed? In *Carbon Capture and Storage in International Energy Policy and Law* (pp. 385--393). Elsevier. doi:<https://doi.org/10.1016/B978-0-323-85250-0.00019-0>
- Bandilla, K. W. (2020). Carbon capture and storage. In *Future Energy* (Third Edition ed., pp. 669--692). Elsevier. doi:<https://doi.org/10.1016/B978-0-08-102886-5.00031-1>

- 
- Bouckaert, S., Pales, A. F., McGlade, C., Remme, U., Wanner, B., Varro, L., . . . Spencer, T. (2021). *Net Zero by 2050: A Roadmap for the Global Energy Sector*. IEA.
- Brobakken, I. I. (2018). *Modeling of CO<sub>2</sub> Storage in the Smeaheia Field*. NTNU. Retrieved from <http://hdl.handle.net/11250/2615132>
- Cameron, D. A., & Durlofsky, L. J. (2012). Optimization of well placement, CO<sub>2</sub> injection rates, and brine cycling for geological carbon sequestration. *International Journal of Greenhouse Gas Control*, *10*, 100--112. doi:<http://dx.doi.org/10.1016/j.ijggc.2012.06.003>
- Cook, P. J. (1999). Sustainability and nonrenewable resources. *Environmental Geosciences*, *6*(4), 185--190. doi:<https://doi.org/10.1046/j.1526-0984.1999.64004.x>
- Equinor, & Gassnova. (2021). *Smeaheia Dataset*. Retrieved from CO<sub>2</sub> DataShare: <https://co2datashare.org/dataset/smeaheia-dataset>
- Erichsen, E., Rørvik, K. L., Kearney, G., & Haaberg, K. (2013). *Troll kystnær subsurface evaluation report*. Gassnova SF.
- Ettehadvakkol, A., Lake, L. W., & Bryant, S. L. (2014). CO<sub>2</sub>-EOR and storage design optimization. *International Journal of Greenhouse Gas Control*, *25*, 79--92. doi:<https://doi.org/10.1016/j.ijggc.2014.04.006>
- Géron, A. (2019). *Hands-on machine learning with Scikit-Learn, Keras, and TensorFlow: Concepts, tools, and techniques to build intelligent systems*. O'Reilly Media, Inc.
- Gholami, V. (2014). *On the optimization of CO<sub>2</sub>-EOR process using surrogate reservoir model*. West Virginia University. doi:<https://doi.org/10.33915/etd.5668>
- Goldberg, D. E. (1983). *Computer-aided gas pipeline operation using genetic algorithms and rule learning*. University of Michigan.
- Golzari, A., Sefat, M. H., & Jamshidi, S. (2015). Development of an adaptive surrogate model for production optimization. *Journal of petroleum Science and Engineering*, *133*, 677--688. doi:<https://doi.org/10.1016/j.petrol.2015.07.012>
- Harding, F. C., James, A. T., & Robertson, H. E. (2018). The engineering challenges of CO<sub>2</sub> storage. *Proceedings of the Institution of Mechanical Engineers, Part A:*

- 
- Journal of Power and Energy*, 232(1), 17--26.  
doi:<https://doi.org/10.1177%2F0957650918756542>
- Haupt, R. L., & Haupt, S. E. (2004). *Practical genetic algorithms*. John Wiley & Sons, Inc.
- Hendrix, E. M., Boglárka, G.-T., & others. (2010). *Introduction to nonlinear and global optimization* (Vol. 37). Springer. doi:<https://doi.org/10.1007/978-0-387-88670-1>
- Hill, B., Hovorka, S., & Melzer, S. (2013). Geologic carbon storage through enhanced oil recovery. *Energy Procedia*, 37, 6808--6830.  
doi:<https://doi.org/10.1016/j.egypro.2013.06.614>
- Holland, J. H. (1975). *Adaptation in natural and artificial systems: an introductory analysis with applications to biology, control, and artificial intelligence*. University of Michigan.
- Hosseini Boosari, S. S. (2019). Predicting the dynamic parameters of multiphase flow in CFD (Dam-Break simulation) using artificial intelligence-(cascading deployment). *Fluids*, 4(1), 44. doi:<https://doi.org/10.3390/fluids4010044>
- Jaber, A. K., Al-Jawad, S. N., & Alhuraishawy, A. K. (2019). A review of proxy modeling applications in numerical reservoir simulation. *Arabian Journal of Geosciences*, 12(22), 1--16. doi:<https://doi.org/10.1007/s12517-019-4891-1>
- Jiang, X. (2011). A review of physical modelling and numerical simulation of long-term geological storage of CO<sub>2</sub>. *Applied energy*, 88(11), 3557--3566.  
doi:<https://doi.org/10.1016/j.apenergy.2011.05.004>
- Kingma, D. P., & Ba, J. (2014). Adam: A Method for Stochastic Optimization. *ICLR 2015*. arXiv preprint arXiv:1412.6980.
- Konak, A., Coit, D. W., & Smith, A. E. (2006). Multi-objective optimization using genetic algorithms: A tutorial. *Reliability engineering & system safety*, 91(9), 992--1007. doi:<https://doi.org/10.1016/j.ress.2005.11.018>
- Kramer, O. (2017). *Genetic algorithm essentials*. Springer Cham.  
doi:<https://doi.org/10.1007/978-3-319-52156-5>
- Kuk, M., Kuk, E., Janiga, D., Wojnarowski, P., & Stopa, J. (2020). Optimization Wells Placement Policy for Enhanced CO<sub>2</sub> Storage Capacity in Mature Oil Reservoirs. *Energies*, 13(16), 4054. doi:<https://doi.org/10.3390/en13164054>

- 
- Li, Q., & Liu, G. (2016). Risk assessment of the geological storage of CO<sub>2</sub>: A review. *Geologic Carbon Sequestration*, 249--284. doi:[https://doi.org/10.1007/978-3-319-27019-7\\_13](https://doi.org/10.1007/978-3-319-27019-7_13)
- Liu, S., Agarwal, R., Sun, B., Wang, B., Li, H., Xu, J., & Fu, G. (2021). Numerical simulation and optimization of injection rates and wells placement for carbon dioxide enhanced gas recovery using a genetic algorithm. *Journal of Cleaner Production*, 280, 124512. doi:<https://doi.org/10.1016/j.jclepro.2020.124512>
- Masson-Delmotte, V., Zhai, P., Pörtner, H.-O., Roberts, D., Skea, J., Shukla, P. R., . . . others. (2018). Global warming of 1.5 C. *An IPCC Special Report on the impacts of global warming of 1.5 C*, 1(5).
- Matthew, D. (2021). *Proxy Modeling for CO<sub>2</sub>-EOR Design Study: Water Alternating Gas and Storage*. NTNU. Retrieved from <https://hdl.handle.net/11250/2786742>
- Metz, B., Davidson, O., De Coninck, H., Loos, M., & Meyer, L. (2005). *IPCC special report on carbon dioxide capture and storage*. Cambridge: Cambridge University Press.
- Mohaghegh, S. D. (2018). *Data-driven analytics for the geological storage of CO<sub>2</sub>*. CRC Press. doi:<https://doi.org/10.1201/b21913>
- Mohaghegh, S. D., Amini, S., Gholami, V., Gaskari, R., & Bromhal, G. (2012). Grid-Based Surrogate Reservoir Modeling (SRM) for fast track analysis of numerical reservoir simulation models at the grid block level. *SPE Western Regional Meeting*. doi:<https://doi.org/10.2118/153844-MS>
- Nait Amar, M., Zeraibi, N., & Redouane, K. (2018). Optimization of WAG process using dynamic proxy, genetic algorithm and ant colony optimization. *Arabian Journal for Science and Engineering*, 43(11), 6399--6412. doi:<https://doi.org/10.1007/s13369-018-3173-7>
- Nations, U. (2015). Adoption of the paris agreement. In *United Nations Framework Convention on Climate Change, Paris* (p. 31).
- Nayak, R. a. (2001). Artificial neural networks in biomedical engineering: a review. *Computational Mechanics--New Frontiers for the New Millennium*, 887--892. doi:<https://doi.org/10.1016/B978-0-08-043981-5.50132-2>
- Ng, C. S., Jahanbani Ghahfarokhi, A., Nait Amar, M., & Torsæter, O. (2021). Smart proxy modeling of a fractured reservoir model for production optimization:

- implementation of metaheuristic algorithm and probabilistic application. *Natural Resources Research*, 30(3), 2431--2462. doi:<https://doi.org/10.1007/s11053-021-09844-2>
- Rackley, S. (2017). Introduction to geological storage. In *Carbon capture and storage* (Second Edition ed., pp. 285--304). Boston: Butterworth-Heinemann. doi:<https://doi.org/10.1016/B978-0-12-812041-5.00011-8>
- Rackley, S. A. (2017). Fluid properties and rock–fluid interactions. In S. A. Rackley, *Carbon Capture and Storage* (Second Edition ed., pp. 337-364). Butterworth-Heinemann. doi:<http://dx.doi.org/10.1016/B978-0-12-812041-5.00013-1>
- Rao, S. S. (2019). *Engineering optimization: theory and practice*. John Wiley & Sons, Inc. doi:10.1002/9781119454816
- Santibanez-Borda, E. a. (2019). Maximising the dynamic CO<sub>2</sub> storage capacity through the optimisation of CO<sub>2</sub> injection and brine production rates. *International Journal of Greenhouse Gas Control*, 80, 76--95. doi:<https://doi.org/10.1016/j.ijggc.2018.11.012>
- Silva, I. N., Spatti, D. H., Flauzino, R. A., Liboni, L. H., & Alves, S. R. (2017). *Artificial neural networks: a practical course*. Springer Cham. doi:<https://doi.org/10.1007/978-3-319-43162-8>
- Sivanandam, S., & Deepa, S. (2008). *Introduction to genetic algorithms*. Springer Berlin; Heidelberg. doi:<https://doi.org/10.1007/978-3-540-73190-0>
- Snyman, J. A., & Wilke, D. N. (2018). *Practical Mathematical Optimization: Basic Optimization Theory and Gradient-Based Algorithms*. Springer. doi:<https://doi.org/10.1007/978-3-319-77586-9>
- Statoil. (2016). *Subsurface Evaluation of Smeaheia*. Equinor.
- Sun, Z., Xu, J., Espinoza, D. N., & Balhoff, M. T. (2021). Optimization of subsurface CO<sub>2</sub> injection based on neural network surrogate modeling. *Computational Geosciences*, 25(6), 1887--1898. doi:<https://doi.org/10.1007/s10596-021-10092-9>
- van der Meer, L. B., Hofstee, C., & Orlic, B. (2009). The fluid flow consequences of CO<sub>2</sub> migration from 1000 to 600 metres upon passing the critical conditions of CO<sub>2</sub>. *Energy Procedia*, 1(1), 3213--3220. doi:<https://doi.org/10.1016/j.egypro.2009.02.105>

- 
- Yang, X.-S. (2021). Genetic Algorithms. In *Nature-Inspired Optimization Algorithms* (Second Edition ed., pp. 91-100). Academic Press.  
doi:<https://doi.org/10.1016/B978-0-12-821986-7.00013-5>
- Zhang, D., & Song, J. (2014). Mechanisms for geological carbon sequestration. *Procedia IUTAm*, 10, 319--327.  
doi:<https://doi.org/10.1016/j.piutam.2014.01.027>
- Zubarev, D. I. (2009). Pros and cons of applying proxy-models as a substitute for full reservoir simulations. *SPE Annual Technical Conference and Exhibition*.  
doi:<https://doi.org/10.2118/124815-MS>

